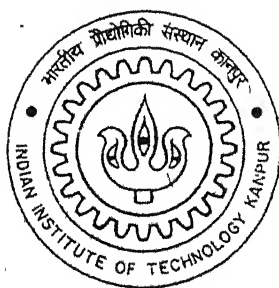


# **UV LASER ACTION IN PULSED LASER DEPOSITED NANOCRYSTALLINE ZnO THIN FILMS**

**BY  
ANIRBAN MITRA**



TH  
PHY/2002/D  
M 6974

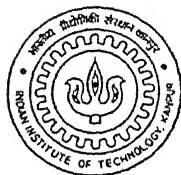
**DEPARTMENT OF PHYSICS  
INDIAN INSTITUTE OF TECHNOLOGY KANPUR**

**January, 2002**

# UV LASER ACTION IN PULSED LASER DEPOSITED NANOCRYSTALLINE ZnO THIN FILMS

*A Thesis Submitted  
in Partial Fulfilment of the Requirements  
for the degree of*  
**Doctor of Philosophy**

by  
Anirban Mitra



Department of Physics,  
Indian Institute of Technology, Kanpur.  
January, 2002.

23

2003

/10/

145026

145026



A1 5026

# CERTIFICATE

---

It is certified that the work contained in this thesis entitled “**UV Laser Action in Pulsed Laser Deposited Nanocrystalline ZnO Thin Films**” by Anirban Mitra has been carried out under my supervision and the same has not been submitted elsewhere for a degree.

31 st, January, 2002.

I.I.T, Kanpur

  
( **Raj K. Thareja** )

Professor  
Department of Physics  
I.I.T. Kanpur.



## List of publications:

---

1. **A. Mitra**, R. K. Thareja, V. Ganesan, A. Gupta, P. K. Sahoo and V. N .Kulkarni, "*Synthesis and characterization of ZnO thin films for UV laser*", Appl. Surface Science, **174**, (2001) pp 232.
2. **Anirban Mitra and Raj. K. Thareja**, "*Dependence of Second Harmonic Generation on Size of Nanocrystallites of ZnO*", Mod. Phys. Lett. B. **15**, (2001) pp 515.
3. **Anirban Mitra and R. K. Thareja**, "*Photoluminescence and ultraviolet laser emission from nanocrystalline ZnO thin film*", J. of Appl. Phys. **89**, (2001) pp 2025
4. R. K. Thareja and **A. Mitra**, " *Random Laser Action in ZnO*", Appl. Phys. B **71**, (2000) pp 181-184.
5. **A. Mitra** and R. K. Thareja, "*Ultraviolet laser Emission from Optically Pumped ZnO*", Mod. Phys. Lett. B. **13**, (1999) pp 1075.

## *Acknowledgement*

---

I express my sincere gratitude to Prof. R. K. Thareja for introducing me into the exciting field of lasers. Before coming to this place I was mere a novice in the experimental field of physics. I am grateful to him for giving me an opportunity and providing a wonderful academic environment.

I express my sincere regards to Dr. (Mrs.) Sukarma Thareja for her encouragement and suggestions. I have also enjoyed a good time with Aditya and Prachi.

I am thankful to the members of my peer group Prof. K. K. Sharma, Prof. V. A. Singh, Prof. V. N. Kulkarni, Prof. S. Kumar and Prof. Asima Pradhan for their comments and useful suggestions.

I greatly acknowledge the help and cooperation of my all labmates Dr. R. K. Dwivedi, Dr. Amit Sirkar, Dr. Amit Neogi, Dr. Ashutosh Misra, Narayanan, Ashwini, Shusmita, Mukesh, Prashant and Himanshu..

My special thanks to Ashutosh, Amit, Narayanan and Ashwini for extending their cooperation during my stay in the lab.

I am thankful to Mr. Kuldeep Singh, Mr. Upkar Singh, and Mr. Maharaj Singh for their constant help regarding different technical problems. I also acknowledge the help of all staff members of CELT and Physics Department.

I am thankful to the members of the Physics and CELT workshop.

I acknowledge the help of Prof. Ajay Gupta and Dr. V. Ganesan for hospitality and help in doing the experiments on AFM.

I also acknowledge the help of Prof. V. N. Kulkarni and Pratap Sahoo in doing the experiments on RBS.

It has been a wonderful experience of my long stay at IIT, Kanpur. I enjoyed my association with friends coming from different walks of life. It happened to be a memorable experience of staying at C-TOP with Tapoda, Tapan Khan, Manoj, Debada, Koushik Basak, Koushik Biswas, Kamallesh Mandal, Aloked, Prasenjit and at later stage with Kesta (Kousjik Nandi).

I am specially thankful to Tapoda (Dr. Tapobrata Som) and Shankarda (Dr. Shankar Dhar) for encouraging me to join this place.

I also enjoyed a good time with old friends of Hall 4, specially Swapanda, Mama, Sonuda, Alok Sharan, Rajan Gurjar, Atanuda and others.

My last days of stay at IITK became enjoyable with my association with Rajib, Surajit, Santosh, Pradip, Samit, Arunangshuda, Sandip and Prasanta.

Thanks to my old friend Koushik (Dr. Koushik Ray) for giving me a chance to relax and share the old memories of our stay.

I have some great memories of my Late Mama. He always encouraged me for higher studies. His absence at the last stage of my thesis is a great loss for me.

I am grateful to my parents and my sister for their constant encouragement to do Ph.D. Without their cooperation and sacrifice it would not have been possible for me to finish my thesis.

*Anirban*

*Dedicated to my Parents*

## Synopsis

---

---

Name of the student	: <b>Anirban Mitra</b>
Roll No	: <b>9520961</b>
Department	: <b>Physics</b>
Degree for which submitted	: <b>Ph.D.</b>
Thesis title	: <b>UV LASER ACTION IN PULSED LASER DEPOSITED NANOCRYSTALLINE ZnO THIN FILMS</b>
Name of the thesis supervisor	: <b>Prof. Raj K. Thareja</b>

---

---

This thesis describes the detailed study of pulsed laser deposited ZnO thin films for its applications as a medium of UV laser. The films were deposited using pulsed laser deposition technique and characterized using X-ray Diffraction (XRD), Atomic Force Microscopy (AFM), Photoluminescence (PL), Rutherford Backscattering (RBS). Random lasing action observed in ZnO pellet and ZnO thin films are presented. The dependence of PL and lasing properties on crystallite size of ZnO are discussed. Nonlinear optical properties of ZnO thin films are also studied.

ZnO thin films were deposited using third harmonic of (355 nm) of a Q- switched Nd:YAG laser (Spectra Physics, DCR4G, pulse width 10 ns with maximum energy of 1 J per pulse in fundamental wavelength 1.06  $\mu\text{m}$ ). The laser radiation was focused to a spot of diameter 250  $\mu\text{m}$  onto a ZnO target in a vacuum chamber that could be evacuated to a pressure better than  $10^{-5}$  Torr. The chamber was specifically designed for laser ablation studies. It has four small and four big ports that can be used for various diagnostics of plasma. The chamber has a provision for introducing gas in a controlled manner. The experiments were conducted at an ambient pressure of oxygen varying from  $10^{-3}$  Torr to 1 Torr. Target was continuously rotated and translated with the help of a stepper motor to ensure that each laser pulse hits a fresh surface of the target. Laser was focused onto the target through the front window with the help of a lens (focal length 45 cm). Substrate

was kept at a distance of 4 cm from the target. All films were deposited at room temperature.

The structural characteristics of as deposited films were studied prior to looking for laser action in them. XRD of the films, using  $\text{CuK}\alpha$  ( $1.5418 \text{ \AA}$ ) source, grown at pressures less than  $3 \times 10^{-1}$  Torr showed the films to be highly oriented along (002) plane, implying c-axis of the film uniformly perpendicular to the surface. At pressures greater than or equal to  $3 \times 10^{-1}$  Torr, the planes (101), (002), (100) were observed. The sharpened and enhanced diffraction peaks (FWHM) with increasing pressure imply that the particle size increases at higher ambient pressures. The average diameter of nanocrystallites is estimated using the broadening of the diffraction peaks in the Scherrer's formula. The size of nanocrystallites varied from 7 to 16 nm (with an error of less than 20 %). The substrate temperature, ambient gas pressure and target substrate distance, in addition to laser parameters are the factors that control the width of the diffraction peaks and hence the size of the nanocrystallites. It is expected that at higher pressures, the compressed plasma plume will lead to nucleation of larger ZnO clusters. Therefore, it is possible to control the size of clusters by controlling the ambient gas pressure. However, it is important for ZnO film growth that the amount of reactive oxygen created from the ambient gas be sufficient to help reduce the number of oxygen vacancies.

Surface morphology of the films was studied using AFM. Measurements were done in air. Film samples were scanned over areas ranging from  $500 \times 500 \text{ nm}^2$  to  $1 \times 1 \text{ }\mu\text{m}^2$  at different locations on the film surface. Surface morphology varied among films grown at various ambient pressures. The films grown at lower oxygen pressures were smoother than those grown at higher pressures. At pressures greater than  $3 \times 10^{-1}$  Torr the film became powdery with observable clustering of grains. However, the films deposited at  $10^{-1}$  Torr showed a particular orientation direction, in confirmation with XRD. The average roughness varied from 20 to 108 nm within the scanned area of  $1 \times 1 \text{ }\mu\text{m}^2$  in the pressure range studied. The root mean square (r. m. s.) value of the grain size ranged from 20 to 200 nm. AFM pictures showed the clusters formation at pressures greater than or equal to 1 Torr.

Photoluminescence study was done by exciting the ZnO thin films using third harmonic (355 nm, pulse width 5 ns) of the Nd:YAG laser. Emission spectra from the

samples were recorded using a fiber coupled to the Monochromator (Jobin Yvon, HRS 2). Generally three peaks (in UV, green and red region of the spectrum) were observed from the ZnO films. The UV peak is attributed to the band edge emission whereas the other two peaks in red and green region are attributed to defects in the films. The ratio of the UV emission to other emission can be used to give information whether the films are defect free or not. In our work we obtained only one peak around 390 nm implying that grown films are defect free. The intensity of the strong PL peak observed at 395 nm decreases with the increase in ambient oxygen pressure. This may be due to unfavorable Zn:O ratio at higher pressures of oxygen.

The thickness and composition of the films was measured using RBS technique. The thickness of the films increased with the increase in pressure of the ambient oxygen. The thickness of the deposited films varied from 115 nm to 1050 nm at pressure of  $10^{-2}$  Torr to 1 Torr. The composition Zn:O of the films varied from 1:1 at lower pressures to 1:2.5 at pressures greater than  $10^{-2}$  Torr.

Letokhov in 1967 predicted amplification of light due to multiple scattering in random medium. Nonetheless, it took 25 years to show experimentally the amplification of light. Lawandy and coworkers showed that a dramatic spectral narrowing occurs on addition of scatterer like  $\text{TiO}_2$  in a laser dye like Rhodamine 6G. The mechanism of formation of laser cavities in such a random gain medium is different from that of a conventional laser. They showed that strong and recurring scattering in a random gain medium helps in forming closed-loop feedback paths leading to lasing. The system is termed as a random laser. We have studied the random laser action in bulk ZnO pellet as well as in ZnO thin films. The ZnO pellet was made from zinc oxide powder (99.99% pure) cold pressed under a pressure of 6 tons for 20 min and then sintered at  $1000^\circ\text{C}$  for 5 h. Methanol was used as a binder for making the pellet. The pellets used in the study were a disc of thickness 8 mm and diameter 2 cm. Experimental set up similar to PL experiment was used for observing the random laser action. The sample was optically pumped with the third harmonic (355 nm, pulse width 5 ns) of a Q-switched Nd:YAG laser. A steep rise in the output after the input pump energy exceeds  $1500 \text{ kW/cm}^2$ , has been observed which can be taken as the lasing threshold. Below the threshold excitation intensity, the spectrum observed is a single broad spontaneous emission peak. As the

input intensity increases, the emission becomes narrower due to preferential amplification at frequencies close to the maximum of the gain spectrum. At excitation intensity above threshold very narrow peaks are observed in the emission spectrum. The line width of these peaks decreased to less than 0.6 nm, which is more than 25 times smaller than the line width of amplified spontaneous emission below threshold. In our samples average particle size is 20 nm, the scattering mean free path is as short as 0.232  $\mu\text{m}$  and hence many closed loops may be formed. These loops could serve as ring cavities having different losses. The discrete peaks observed in emission spectra clearly show the laser emission. The dependence of laser action on excitation volume and excitation intensity was studied by varying the excitation area. As the excitation area increases the lasing threshold pump intensity decreases and more lasing peaks are observed in the emission spectra. However, the laser oscillations stopped once the excitation area decreased below a critical area. The optical gain of the laser was measured by measuring the laser output (above threshold) for two excitation lengths. We obtained the gain coefficient of  $7.50 \text{ cm}^{-1}$ .

Random lasing action in pulsed laser deposited ZnO thin films also showed a lasing threshold. To observe laser action, films of various thickness were optically pumped by third harmonic of Nd:YAG laser. Similar to ZnO pellet a single broad emission peak is observed below the threshold excitation intensity. A steep increase in the output intensity as the pump laser exceeds an intensity of  $2387 \text{ kW/cm}^2$  is observed. At excitation above threshold very narrow peaks, almost 10 times narrower than the emission below lasing threshold, are observed in the emission spectrum. In the case of thin film the emission spectrum also becomes narrower due to preferential amplification at frequencies close to the maximum of the gain spectrum. Due to local variation of particle density and spatial distribution in the films, there exist small regions of higher disorder and stronger scattering and of lower disorder and weaker scattering. Light can be confined in these regions forming closed loop feedback paths through multiple scattering and interference. The gain depends on the volume ( $\frac{4}{3}\pi a^3$ ) of the disordered amplifying medium and loss to its surface area ( $4\pi a^2$ ), where 'a' is the radius of sphere of disordered material. Laser oscillations occur once the optical gain in a cavity exceeds the losses of a cavity. The various peaks observed in the emission spectrum are the cavity resonant



frequencies. Increasing thickness of the film can lead to three-dimensional localization of light and hence to increased emission. To confirm, ZnO films of thickness 0.5, 1 and 1.5  $\mu\text{m}$  were pumped at intensity of 3310  $\text{kW}/\text{cm}^2$ . The films were deposited at ambient pressure of  $10^{-1}$  Torr. Films deposited at higher pressures did not yield good results due to poor stoichiometry. It is also confirmed by PL and RBS studies. The intensity of the laser emission increased with the increase of film-thickness. The increased emission is attributed to a longer optical path in thick films contributing to amplification.

An extensive investigation of the nonlinear optical properties of ZnO thin films deposited under different ambient pressures of oxygen was undertaken. We used the fundamental wavelength (1.06  $\mu\text{m}$ , pulse width 10 ns) of Nd:YAG laser for generation of second harmonic. Vertically, s- or p-polarized light of Nd:YAG laser is transmitted through the ZnO thin films. The incident angle of the fundamental beam is continuously varied by rotating the ZnO thin film. After passing through the thin film, the generated second harmonic of the fundamental beam is detected by a photodiode. Fundamental beam is cutoff by using a filter and only second harmonic that was reflected by dichoric mirror, is ultimately detected by a photodiode.

Second harmonic coefficient ( $\chi_{\text{eff}}^{(2)}$ ) for different films deposited under different ambient pressures is evaluated by fitting the experimental data with the equation which generates the Maker fringes. Variation of second harmonic intensity versus incident angle produces a fringe pattern called Maker fringes. It is found that the films at lower pressure have higher second harmonic generation coefficient ( $\chi_{\text{eff}}^{(2)}$ ) than those deposited at higher pressure. This is may be due to the poor crystallinity and orientations of the films at lower pressure. Another reason may be the grain size of the film. At higher pressures grain size of the film is larger than those deposited at lower pressure.

The second harmonic generation shows a steep increase with the increase in input energy of the fundamental for thicker films. The thickness of the films as measured by RBS is 115 nm, 450 nm, 550 nm, 700 nm and 1050 nm deposited under pressure of  $10^{-2}$  Torr,  $10^{-1}$  Torr,  $3 \times 10^{-1}$  Torr,  $6 \times 10^{-1}$  Torr,  $9 \times 10^{-1}$  Torr and 1 Torr respectively. Though the second harmonic generation coefficient is more for the films deposited at lower pressure, the films deposited at higher pressure show more second harmonic generation due to the

thicker films. It implies that second harmonic generation does not only depend on the crystallinity but also on the thickness of the films.

To conclude we have deposited ZnO thin films under various ambient pressures of oxygen so as to explore its potentials as a UV laser source and non-linear optical material for integrated optics. We have observed random lasing action in ZnO pellet as well as ZnO thin films. Characterizations of the as deposited films by several techniques confirm the strong dependence of lasing action on different parameters like grain size, stoichiometry and thickness of the films.

# Table of Contents

---

<b>List of Tables.....</b>	<b>iii</b>
<b>List of Figures .....</b>	<b>iv</b>
<b>List of Symbols .....</b>	<b>vii</b>
<b>Chapter 1.....</b>	<b>1</b>
<b>Introduction .....</b>	<b>1</b>
1.1    ZnO : A novel wide band gap photonic material .....	2
1.2    Random Laser Action.....	6
1.3    Characterization of ZnO films.....	8
1.4    The Present Work.....	9
<b>Chapter 2.....</b>	<b>11</b>
<b>Experimental Techniques .....</b>	<b>11</b>
2.1    Pulsed Laser Deposition Setup.....	11
2.2    Characterization of Deposited Thin Films .....	13
2.2.1 <i>X –ray diffraction</i> .....	13
2.2.2 <i>Atomic Force Microscopy</i> .....	15
2.2.3 <i>Photoluminescence and Random Lasing Action</i> .....	17
2.2.4 <i>Coherent Backscattering</i> .....	19
2.2.5 <i>Rutherford Backscattering</i> .....	26
<b>Chapter 3.....</b>	<b>28</b>
<b>Synthesis and characterization of ZnO thin films for UV laser.....</b>	<b>28</b>
3.1    Physical Processes.....	28
3.2    Pulsed Laser Deposition of Thin Films.....	35
3.3    Deposition of ZnO films .....	37

3.4	Results and Discussion.....	37
3.5	Conclusions .....	48
<b>Chapter 4.....</b>		<b>49</b>
<b>Random Lasing Action in ZnO .....</b>		<b>49</b>
4.1.	Experimental details:.....	53
4.2.	Results and discussion.....	54
4.2.1	<i>Laser action in ZnO pellets .....</i>	<i>54</i>
4.2.2	<i>Laser action in PLD ZnO thin films .....</i>	<i>59</i>
4.2.3	<i>Theoretical Model: .....</i>	<i>62</i>
4.3	Conclusions .....	64
<b>Chapter 5.....</b>		<b>66</b>
<b>Second Harmonic Generation from Pulsed Laser Deposited ZnO Thin Film .....</b>		<b>66</b>
5.1	Nonlinear Optical Effects in Crystals .....	67
5.2	Second Harmonic Generation .....	69
5.3	Second Harmonic Generation in Thin Films .....	73
5.4	Experimental details:.....	74
5.5	Results and Discussions .....	75
5.6	Conclusions .....	80
<b>Chapter 6.....</b>		<b>81</b>
<b>Conclusion and scope of future work .....</b>		<b>81</b>
<b>References .....</b>		<b>86</b>

## List of Tables

---

Table 1- 1 Properties of ZnO and other wide band gap semiconductors .....	3
Table 1- 2 Different methods used for thin film characterization.....	9

## List of Figures

Figure 2- 1: Experimental Set up for Pulsed Laser Deposition of Thin Films.....	12
Figure 2- 2: Typical XRD spectrum of ZnO thin film .....	14
Figure 2- 3: A 3-D topography of PLD ZnO film.....	16
Figure 2- 4: Light emission(a) and absorption (b) by a semiconductor .....	17
Figure 2- 5: Experimental set up for Photoluminescence and Random Laser Action .....	19
Figure 2- 6: Schematic path followed by an incoming and scattered light from random medium.....	20
Figure 2- 7: Theoretical curve of equation (2.22) for ZnO thin film. ....	23
Figure 2- 8: Experimental Set up for Coherent Backscattering Experiment.....	24
Figure 2- 9: Coherent backscattering spectrum from a ZnO pellet.....	25
Figure 2- 10: Coherent backscattering spectrum from a ZnO thin film.....	25
Figure 2- 11: Typical RBS spectrum of PLD ZnO thin film .....	27
 Figure 3- 1: Different regions of Laser Plasma Interaction .....	 30
 Figure 3-2: Variation of FWHM of the diffraction peak corresponding to the plane (0 02) .....	 38
Figure 3- 3: XRD spectra of ZnO films deposited under various oxygen pressure at RT	38
Figure 3- 4: 2-D AFM photographs of ZnO films deposited under different oxygen pressures .....	40
Figure 3- 5: 3-D AFM photographs of ZnO films deposited under different oxygen pressures at RT .....	41
Figure 3- 6: Variation of the surface roughness of the ZnO films deposited under different ambient oxygen pressure .....	42
Figure 3- 7: Variation of the grain size of the ZnO films with ambient oxygen pressure	42
Figure 3- 8: PL spectra of ZnO films grown at various oxygen pressures.....	44
Figure 3- 9: Variation of FWHM of PL with ambient pressure of oxygen.....	45
Figure 3- 10: RBS spectrum of ZnO thin films deposited under various ambient oxygen pressures. ....	46

Figure 3- 11: Variation of ZnO film thickness as measured by RBS deposited under different ambient oxygen pressures.....	47
Figure 3- 12: Raman spectra of ZnO pellet (a) and PLD ZnO film (b) .....	47
Figure 4- 1: Regular laser cavity and Random Laser.....	52
Figure 4- 2: Emission spectra at different excitation intensity (a) 1527 kW/cm <sup>2</sup> (b) 2860 kW/cm <sup>2</sup> (c) 3310 kW/cm <sup>2</sup> and (d) 7890 kW/cm <sup>2</sup> .....	54
Figure 4- 3: Variation of peak emission intensity as a function of excitation intensity....	54
Figure 4- 4: Variation of threshold excitation intensity with diameter of the focused spot .....	55
Figure 4- 5: Variation of the spectral width (FWHM) of the observed modes with the excitation intensity. ....	56
Figure 4- 6: Emission spectrum for two different excitation lengths (a) $l_g=2$ mm (b) $l_g'=1$ mm.....	57
Figure 4- 7: Emission spectra for two different observation angles: (a) $10^0$ from the normal to the sample surface, (b) normal to the sample surface. The excitation intensity is 7890 kW/cm <sup>2</sup> . The excitation area is 3.14 mm <sup>2</sup> . Left side inset shows the formation of ring cavities due to the multiple scattering. Right side inset shows the directions of the laser and detector.....	58
Figure 4- 8: Emission spectra from an optically pumped ZnO film of 1.5 $\mu$ m thickness deposited at oxygen pressure of $10^{-1}$ Torr .....	60
Figure 4- 9: Variation of peak emission intensity with excitation intensity of laser. ....	61
Figure 4- 10: Emission spectra from ZnO film of thickness of (a) 0.5 (b) 1 and (c) 1.5 $\mu$ m.....	61
Figure 4- 11: Level diagram of a four level electronic material showing the emission and absorption.....	63
Figure 5- 1: A ray diagram of the four layer thin film system of non-linear optical material generating second harmonic.....	73
Figure 5- 2: Experimental set-up for Second Harmonic Generation .....	75

Figure 5- 3: Angular dependence of second harmonic intensity of the ZnO films deposited at (a) $10^{-1}$ Torr, (b) $3 \times 10^{-1}$ Torr, (c) $6 \times 10^{-1}$ Torr and (d) $9 \times 10^{-1}$ Torr of oxygen. ....	77
Figure 5- 4: Variation of SHG coefficient with ambient pressure of oxygen .....	78
Figure 5- 5: Variation of SHG coefficient with grain size of ZnO crystallites .....	78
Figure 5- 6: Variation of SHG intensity with film thickness of ZnO .....	79
Figure 5- 7: Variation of SHG intensity with laser pump energy. ....	79



## List of Symbols

---

$a$	Lattice parameter
$A$	Area
$\alpha_{ab}$	Absorbance
$\alpha(\delta\theta)$	Albedo
$\alpha_{IB}$	Absorption coefficient for inverse bremsstrahlung
$b$	Size of the crystallites
$B$	FWHM of the XRD curve
$\bar{B}$	Magnetic field
$\beta$	Coherence length
$c$	Velocity of light
$d$	Diameter of the diffraction limited spot of laser diode
$d_c$	Spacing between the crystal planes
$d_m$	Cavity length
$D_L$	Diameter of the lens
$D$	Diffusion constant
$\bar{D}$	Displacement current
$e$	Charge of the electron
$E$	Energy
$E_g$	Band gap energy
$\vec{E}$	Electric field
$\epsilon$	Dielectric constant
$f$	Distance of the lens from the compact disc
$\lambda_L$	Wavelength of the laser
$\gamma$	Specific heat ratio
$\hbar$	Plank's constant
$\lambda$	Wavelength of x-ray
$h,k,l$	Miller indices
$\theta$	Angle
$\theta_B$	Peak of the XRD curve
$I$	Intensity
$I_s$	Scattered intensity
$\hat{k}_1, \hat{k}_2$	Propagation vectors of incident and scattered beams
$k$	Propagation vector
$k_B$	Boltzmann constant
$\chi$	Susceptibility
$l_{g-g'}$	Excitation lengths
$l$	Transport mean free path
$l_s$	Scattering mean free path
$L$	Length of the medium
$\Delta\phi$	Phase difference

$\mu$	Permeability
$m$	Mass of the particle
$m_e$	Mass of electron
$n$	Number density
$n(\lambda), n(E)$	Refractive index as a function of wavelength or energy.
$n_c$	Critical density
$n_i$	Density of ions
$n_n$	Density of neutrals
$n_\omega$	Refractive index at frequency $\omega$
$n_{2\omega}$	Refractive index at frequency $2\omega$
$\nu$	Frequency
$\omega_L$	Laser frequency
$\omega_p$	Plasma frequency
$P$	Pressure
$\vec{P}$	Polarization vector
$p$	Exponent
$R_p$	Length of plasma plume
$\rho$	Density
$s$	Total mean free path
$T$	Temperature
$t$	Time
$\tau_L$	Pulse width of laser
$\theta$	Angle
$U_i$	First ionization potential
$v$	Velocity
$X(t), Y(t), Z(t)$	Dimensions of the expanding plasma in three orthogonal directions
$Z$	Charge of the ion

# Chapter 1

## Introduction

---

II-VI semiconductors are attractive for potential in acoustic, electronic, and optical applications such as surface acoustic wave, acousto-optic, piezo-optic, piezo-electric and photoelectric devices and in particular voltage photo-phosphorescent devices [1-4]. Further, it follows from the expression for wavelength of light emitted from a semiconductor with a band gap energy of  $E_g$

$$\lambda = 1.24 / [E_g \text{ (eV)}] \quad [\mu\text{m}] \quad (1.1)$$

that wide band gap II-VI, III-V semiconductors are useful for their uses as UV or blue-green light sources as well as detectors. Since the first demonstration of 490 nm diode laser fabricated from ZnSe base wide band gap II-VI compound semiconductor in 1991 a tremendous progress in commercialization of wide band gap LED/laser diodes has been seen [5]. The main driving force behind such efforts has been the development of blue-green laser diode lasers for optical recording, not withstanding several other applications such as printing, communications, displays and numerous sensor applications etc. In optical recording systems, information are recorded in bits and read by semiconductor laser whose output is focused to a diffraction- limited spot. The diameter  $d$  of the diffraction - limited spot is given by,

$$d = \frac{2\lambda f}{D_L} = \frac{\lambda}{NA} \quad (1.2)$$

where  $\lambda$  is the wavelength of the laser used for reading,  $D_L$  is the diameter of the lens used for focusing,  $f$  is the distance of the lens from the compact disc and NA is the numerical aperture of the lens. Since the diameter of diffraction limited spot is directly proportional to the wavelength of light used to produce it, one can achieve a significant gain in recording density as well as data transfer rate simply by using lasers that operate at shorter wavelength. Among several II-VI semiconductors most useful semiconductors for UV LEDs and laser diodes are ZnO, ZnS, and ZnSe [6]. III-V nitrides like GaN, AlN, InN and their alloys are the other materials useful for this purpose [7]. GaN and its alloys

(e.g. GaAlN, GaInN and AlGaInN) have recently been a focal point of research since the demonstration of high quality GaAlInN based optoelectronics devices like blue laser diode and UV detector [8,9]. However, the conventional II-VI semiconductor materials degrade during device operation due to generation of defects in them.

### 1.1 ZnO : A novel wide band gap photonic material

ZnO, a direct band gap II-VI semiconductor, is a novel photonic material with crystal structure similar to that of GaN. Unique properties of ZnO as compared to other materials are listed in Table 1. These properties reveal that

- (a) ZnO has a large excitonic binding energy of 60 meV compared to other wide band gap materials like ZnSe (20 meV), GaN (21 meV) and ZnS (39 meV) [10], which provides it a low power threshold for optical pumping at room temperature.
- (b) The strength of Zn-to-O bond is larger than that of the Ga-to-N bond.
- (c) It has a high melting point of 2230<sup>0</sup>C compared to ZnSe (1793<sup>0</sup>C), ZnS (2103 <sup>0</sup>C) and GaN (1973<sup>0</sup>C). Being stable at high temperature ZnO can withstand high temperature annealing and treatment processes associated with doping and forming ohmic contacts. It is expected that degradation of the material caused by generation of defects during operation of device will not pose a serious problem.
- (d) ZnO is easily alloyable with other metal oxide like MgO and CdO, and hence offers possibility of tuning of the band gap from 2.8 to 3.3 eV and 3.3 to 4 eV [11].
- (e) With its lattice parameter (a=0.3249 nm, c=0.5207 nm) very near to that of GaN (a=0.3189 nm, c=0.5185 nm) and high refractive index, it can be useful for making heterosturcture LED/laser diode and wave guides [12].
- (f) ZnO films are highly c- axis oriented and self textured. The films can be synthesized on any semiconductor substrate such as Si, GaAs, sapphire, and glass etc[13-15].

These properties make ZnO a good candidate material [16] for optical devices besides widely used GaN.

**Table 1- 1 Properties of ZnO and other wide band gap semiconductors**

Materials	Crystal structure	Lattice constants		Band gap at RT	Meltig pointT <sub>m</sub> (K)	Exciton binding energy E <sup>ex</sup> <sub>b</sub> (eV)	Dielectric constant $\epsilon(0)$
		a(nm)	c(nm)	E <sub>g</sub> (eV)			
ZnO	Wurzite	0.3249	0.5207	3.37	2248	60	8.75
ZnS	Wurzite	0.3824	0.6261	3.8	2103	39	9.6
ZnSe	Zincblende	0.5668		2.7	1793	20	9.1
GaN	Wurzite	0.3189	0.5185	3.39	1973	21	8.9
6H-SiC	Wurzite	0.3081	1.5117	2.86*	2100	-	9.66

\*Indirect band gap

A combination of electron hole pair like hydrogen atom called exciton can act as a source of light in a semiconductor. In fact this can be an alternative to electron hole plasma recombination process common in conventional laser diode operation [17]. The excitonic recombination in semiconductor is a more efficient radiative process and can facilitate low-threshold stimulated emission. To achieve efficient excitonic laser action at room temperature, the binding energy of exciton must be greater than the thermal energy at room temperature ( $kT=25$  meV). ZnO being with an excitonic binding energy of 60 meV has recently been extensively studied for UV laser. Bagnall et al.[18] have reported optical emission from ZnO epilayers at temperatures ranging from room temperature to 550 K. They attributed the single emission peak observed at room temperature and low excitation power to free exciton (3.26 meV). However, at excitation intensities exceeding a certain threshold a sharp peak was observed at lower energy (3.18 meV) due to exciton-exciton scattering. Further increase in intensity gave a second stimulated emission peak at even lower energy (3.14 meV) which they attributed to stimulated emission of electron hole plasma.

Ohtomo et al. [19,20] have reported the increase in the fundamental band gap energy from 3.3 to 4 eV by alloying ZnO with MgO. By varying the magnesium content

they proposed  $\text{ZnO}/\text{Zn}_x\text{Mg}_{1-x}\text{O}$  heterostructure light emitter as well as ultraviolet photo-detectors. In the low dimensional double heterostructure the modified density of states confine both excitons and photons making the stimulated process more efficient. This quantum confinement effect has been observed in  $\text{ZnO}/\text{Mg}_{0.2}\text{Zn}_{0.8}\text{O}$  superlattices. Heterostructure of  $\text{ZnO}/\text{Mg}_x\text{Zn}_{1-x}\text{O}$ ,  $\text{AlN}/\text{ZnO}$ ,  $\text{GaN}/\text{ZnO}$  have been fabricated by making superlattices [12,21-22]. Stimulated emission has also been observed from  $\text{ZnO}/(\text{Mg,Zn})\text{O}$  superlattices [20].

Recently ZnO or impurity doped ZnO films have been extensively studied for use as a transparent conducting electrode material. Doping of ZnO thin films with Al, Ga, and In has been reported to improve their stability as well as their electrical properties [23-25]. ZnO films with about 0.5 at % Al doping have shown low resistivity of  $2\text{-}5 \times 10^{-4} \Omega\text{cm}$ , similar to that observed in indium tin oxide (ITO) films [23-25,26]. Unlike the more commonly used ITO, ZnO is non-toxic, inexpensive, and abundant material. Furthermore, Al doped ZnO (AZO) films have wide band gap of 3.4-3.9 eV, shows high optical transmittance of 90 % in the visible and IR region of electromagnetic spectrum. Due to these unique properties AZO films have been used as transparent conducting electrodes for solar cells, and organic light emitting diodes. Transparent conducting ZnO films have been extensively studied in recent years because of their low cost, relatively low deposition temperature, and stability in hydrogen plasma compared to ITO and  $\text{SiO}_2$  films. These advantages offer considerable improvement in solar energy conversion devices [27]. Highly transparent and conductive ZnO films have been prepared by doping with a group III impurity, such as B, Al, Ga and In and with a group IV impurity, such as Si, Ge, Ti, Zr, and Hf. Al- and In – doped films are being used as transparent electrodes for flat panel displays such as electroluminescent (EL) displays [28,29] and organic LED's [30]. Due to the close proximity of ionic radius of  $\text{Al}^{3+}$  and  $\text{Ga}^{3+}$  to that of  $\text{Zn}^{2+}$  in comparison to other impurities it is believed that best ZnO doped films are that of Al- and Ga-doping. Since the radii of rare earth elements are also close to  $\text{Zn}^{2+}$ , rare earth elements like  $\text{Sc}^{3+}$  and  $\text{Y}^{3+}$  have recently been tried. ZnO films are also being tried for high-resolution field emission display (FED) [31] and thin film electroluminescent (TFEL) devices [32].

It is believed that lasing action in UV region of spectrum from ZnO thin films may be the gateway of fabricating laser diode and LED. Reynolds et al. [33] were the first to observe lasing action from optically pumped ZnO pellet at low temperature (2 K) and at low pump threshold ( $\sim 4 \text{ W/cm}^2$ ). The pellet was grown from the vapor phase. The lasing cavity was an as grown cavity where the bounding surfaces of the cavity were crystal planes. The sample was pumped with a He-Cd laser ( $\lambda=325 \text{ nm}$ ). Lasing action, at room temperature, from optically pumped ZnO thin films was first reported by Bagnall et al [17]. Their films were grown by plasma enhanced molecular beam epitaxy on sapphire substrate. The cleaved end faces formed the laser cavity. They reported a lasing threshold of  $240 \text{ kW/cm}^2$ . Ultraviolet lasing from microcrystalline ZnO thin film grown by pulsed laser beam epitaxy has also been reported at room temperature. Films were self assembled and had hexagonal structure. The facets of the hexagons formed natural Fabry-Perot lasing cavities [34]. The optical gain for the room temperature UV stimulated emission was attributed to excitonic transition and had a peak value an order of magnitude larger than that of bulk ZnO crystal in which laser cavities were formed by cleaving the end faces.

Development of optoelectronics devices from ZnO has been impeded by the fact that the fabrication of p-n junction in ZnO is extremely difficult. It is known that ZnO has Wurtzite structure and is an n-type semiconductor due to interstitial ( $\text{Zn}_i$ ) zinc or oxygen vacancies ( $\text{V}_0$ ). In order to fabricate the p -type semiconductor one needs to compensate these two defects. According to theoretical predictions, among all possible acceptors nitrogen (N) would produce a shallow acceptor level in ZnO. Minegishi [35] et al. have attempted incorporating N by means of  $\text{N}^+$  implantation,  $\text{N}_2$  plasma source, and  $\text{NH}_3$ . The p-type activity was reported only in the case of  $\text{NH}_3$ . The p-type behavior has also been achieved with  $\text{N}_2\text{O}$  gas as source of N, with and without the Electron Plasma Resonance (ECR) source. The resistivity and carrier density of p-type ZnO of  $5 \times 10^5 \text{ } \Omega \text{ cm}$  and  $2 \times 10^{10} \text{ cm}^{-3}$ , respectively has been reported. Best results were obtained on codoping with  $\text{N}_2\text{O}$  (pressure  $1 \times 10^{-3} \text{ mbar}$ ) and  $\text{Ga}_2\text{O}_3$  (5 wt %) [36]. The electrical conductivity of the film increased on doping ZnO with  $\text{Ga}_2\text{O}_3$ . Resistivity of  $4.2 \text{ } \Omega \text{ cm}$  and carrier density as high as  $2 \times 10^{19} \text{ cm}^{-3}$  of film was reported. Xin-Li-Guo [37] has reported p- type ZnO films by N doping using pulsed laser reactive deposition and an electron cyclotron

resonance source. They achieved resistivity of 2-5  $\Omega\text{cm}$  from p- type ZnO thin film grown on fused silica and glass substrate using a pure Zn metal target in  $\text{N}_2\text{O}$  plasma.

Recent developments in growing quantum dots, rods, wires from ZnO have opened up a possibility of making low dimensional opto-electronic devices. Dijken et al [38] reported a detailed analysis of the luminescence quantum efficiency of nanocrystallites ZnO particles. They studied the influence of particle size on the quantum efficiency of the visible emission. The quantum efficiency of visible emission decreases from 20 % for particles with mean radius of 7  $^{\circ}\text{\AA}$  to 12 % for particles with a mean radius of 10  $^{\circ}\text{\AA}$ . Kong et al [39] recently reported UV light emission from physical vapor deposition grown ZnO nanowires. The ZnO nanowire nanocrystallites of an average diameter around 60 nm and length upto a few micrometers were reported. Room temperature ultraviolet lasing action in semiconductor nanowires of ZnO have been demonstrated by Huang et al [40]. The self organized  $\langle 0\ 0\ 01 \rangle$  oriented ZnO nanowires grown on sapphire substrates were synthesized with a vapor transport and condensation process. These wide band gap semiconductor nanowires form natural laser cavities with diameter varying from 20 to 150 nm and lengths up to 10  $\mu\text{m}$ . Under optical excitation surface emitting lasing action was observed at 385 nm with emission line width of less than 0.3 nm [40].

## 1.2 Random Laser Action

In recent years, there has been great interest in the development of microlasers due to their potential applications to integrated photonics circuits. The key issue of the microlaser is to confine light in a small volume with dimensions of the order of optical wavelength. The microlaser based on total internal reflection [41], Bragg scattering [42], and use of Bragg reflectors [43] to confine light have been reported. The fabrication of these lasers requires expensive state of the art crystal growth and micro-fabrication facilities. Commercially available compound semiconductor lasers are made of single crystalline film fabricated by epitaxial growth on lattice-matched substrates. However, epitaxial growth techniques are not only expensive but are restricted to the type of substrate used [44]. Cao et al [45] have demonstrated a microlaser made of disordered medium. The physical mechanism of optical confinement is attributed to Anderson



localization [46,47,48] of light in a micrometer scale random medium. The fabrication of such a microlaser is much easier and cheaper than that of most microlaser. Active medium of such a random laser is a semiconductor ZnO.

Various techniques being used to grow ZnO films are metal-organic chemical vapor deposition (MOCVD) [49], molecular beam epitaxy (MBE) [50,51], sol-gel deposition [52], direct current magnetron sputtering [53], reactive thermal evaporation [54], spray pyrolysis [55], and pulsed laser deposition (PLD). We have used PLD for depositing ZnO films on various substrates [56].

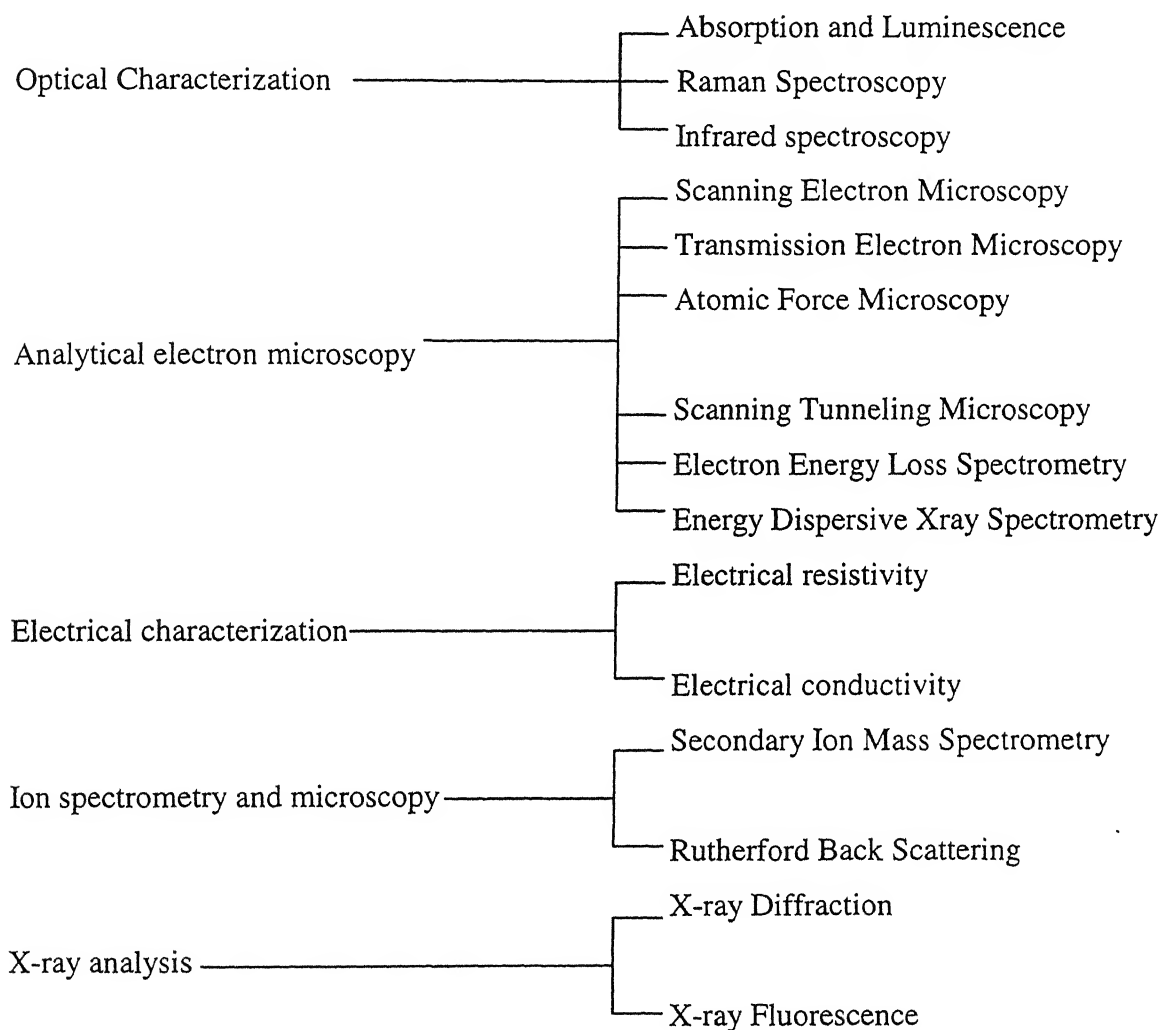
PLD was first reported in 1965 shortly after the invention of pulsed ruby laser [57]. However, its success in the growth of high quality super conducting thin films in a low pressure oxygen environment without the need for further processing in the late eighties got PLD the recognition [58,59]. Today, PLD is used to grow films of ferroelectrics, ferrites, amorphous diamond and other ultra hard phases, polymers, compound semiconductors, and nanocrystalline materials [60]. PLD can be performed in vacuum or in an ambient atmosphere. The ambient gases either thermalize the plasma species through multiple collisions or compensate the loss of an elemental component of the target through incongruent ablation. The expansion of plasma in a background gas has been studied using fluid dynamic models. The collisions between the expanding plasma and the ambient gas molecules results in a shock wave [61]. The front propagates with gradually decreasing velocity towards a substrate on which film growth occurs. For ablation in a gas like oxygen simple oxide molecules are also formed in the expanding ablation plume resulting in oxide film formation on the substrate [61,62]. Among several characteristics that distinguishes PLD from other film growth techniques is congruent (stoichiometric) deposition and hence has been used to grow superconducting superlattices and elegant prototype superconducting device structures [63,64]. Recently, combinatorial methods, an approach in which a large number (library) of materials are synthesized, processed and screened for specific properties have been applied to the discovery and optimization of several functional materials [65,66]. However, the problem of particulates [67] and the uniformity of grown thin films have limited the use of PLD, especially for semiconductors and other electronic thin film materials. It has been shown that metals with low melting temperature are particularly problematic with regards to

production of particulates by exfoliation [68]. Use of liquid targets [69,70] and dual laser ablation techniques have been proposed to minimize the particulate formation [69]. Large area films with uniform thickness have been deposited by `rastering` laser beam over a target [71].

There are several reports of pulsed laser deposited ZnO thin films since 1983 [72]. The pressure of the ambient, choice of substrate, substrate temperature, pulse of ablating laser are among the important parameters for depositing good quality ZnO thin film [73-75]. Choopan et al. [76] studied the influence of the pressure on epitaxy, surface morphology and optoelectronic properties of ZnO thin film. Rutherford backscattering and ion channeling in conjunction with atomic force microscopy were used to ascertain growth mode, degree of epitaxy, etc. The defect density strongly depends on the oxygen background pressure during growth. It is also found that the growth mode and defects strongly influence the electron mobility, free electron concentration, and the luminescence properties of the ZnO thin films. By tuning the oxygen pressure during the initial and final growth stages, smooth and epitaxial ZnO thin films with high optical quality, high electron mobility, and low background carrier concentration have been obtained. Effect of the substrates on the ZnO thin films deposited have also been studied [77,78].

### 1.3 Characterization of ZnO films

Various methods/techniques used to characterize the deposited films are summarized in Table 2.

**Table 1- 2 Different methods used for thin film characterization**

#### 1.4 The Present Work

In the present work, a systematic study of properties of ZnO thin films deposited using pulsed laser technique is reported. The lasing and non-linear properties of the films as an electro-optic material are investigated. The thesis is organized in five chapters. A brief introduction and a survey of the properties as well as several potential applications of ZnO thin films are presented in Chapter 1.

Chapter 2 gives the details of the experimental set up used for pulsed laser deposition of the films, photoluminescence setup, and non-linear susceptibility measurement setup. A brief description of various techniques, X-ray diffraction (XRD), atomic force

---

microscopy (AFM), Rutherford back scattering (RBS), coherent back scattering used to characterize as deposited films is also included in this chapter.

Chapter 3 presents the synthesis and characterization of PLD ZnO thin films. The theoretical details of random lasing action in highly disordered gain medium are presented in Chapter 4. The experimental observations of random lasing action in Bulk ZnO and ZnO thin films are also given in this chapter. Nonlinear properties in particular second harmonic generation in pulsed laser deposited ZnO thin film are reported in Chapter 5.

Concluding remarks and future scope of the work is given in Chapter 6.

## Chapter 2

### Experimental Techniques

---

An overview of ZnO thin films has been discussed in the previous chapter. This chapter describes various experimental tools used/used to deposit and characterize the PLD ZnO thin films for its applications as a medium of UV laser. The films were characterized using X-ray diffraction (XRD), Atomic Force Microscopy (AFM), Photoluminescence (PL), Rutherford Backscattering (RBS). Nd:YAG (Spectra Physics, Model DCR-4G) laser was used for laser ablation.

Nd:YAG laser (Spectra Physics DCR-4 G) used for ablation delivers energy up to 1 J in 2.5 and 8 nsec (FWHM) pulse at fundamental wavelength of 1.06  $\mu\text{m}$  with a pulse repetition rate of 10 Hz. Laser beam has a Gaussian limited mode structure and the beam divergence is less than 0.5 mrad. The energy of the laser beam was measured using a laser power meter (Ophir Model 30 A) by placing the meter in the path of the laser beam. The energy of the laser was varied by varying the voltage of the laser oscillator and the amplifier. The mode structure of the laser remains nearly stable on varying the voltage. The pulse duration was measured using a fast photo diode (Antel, Model AS-2, rise time < 35 psec). Various harmonics are generated using KD\*P crystals. The prism harmonics separator (PHS) was used for separating second, third and fourth harmonics of the laser from the fundamental wavelength [79].

#### 2.1 Pulsed Laser Deposition Setup

The schematic diagram of the experimental setup used for pulsed laser deposition is shown in figure 2.1. ZnO thin films were deposited using third harmonic (355 nm) of Nd:YAG laser (Spectra Physics, DCR4G, pulse width 10 ns with maximum energy of 1 J per pulse in fundamental wavelength 1.06  $\mu\text{m}$ ). The laser radiation was focused to a spot of diameter 250  $\mu\text{m}$  onto a ZnO target in a vacuum chamber that could be evacuated to a pressure better than  $10^{-5}$  Torr. The chamber was specifically designed for laser ablation studies. It has four small and four big ports that can be used for various diagnostics of plasma. The chamber has a provision for introducing gas in a controlled manner. The

chamber was purged with oxygen gas several times before introducing the gas for experiment. The experiments were conducted at an ambient pressure of oxygen varying from  $10^{-3}$  Torr to 1 Torr. Target was continuously rotated and translated with the help of a stepper motor to ensure that each laser pulse hits a fresh surface of the target. Laser was focused onto the target through the one of the windows with the help of a lens of focal length of 45 cm. The films were deposited on glass and silicon substrates at target to substrate distance varying from 2 to 5 cm. All the films used for present work were deposited at room temperature with substrate placed at 4 cm from the target surface.

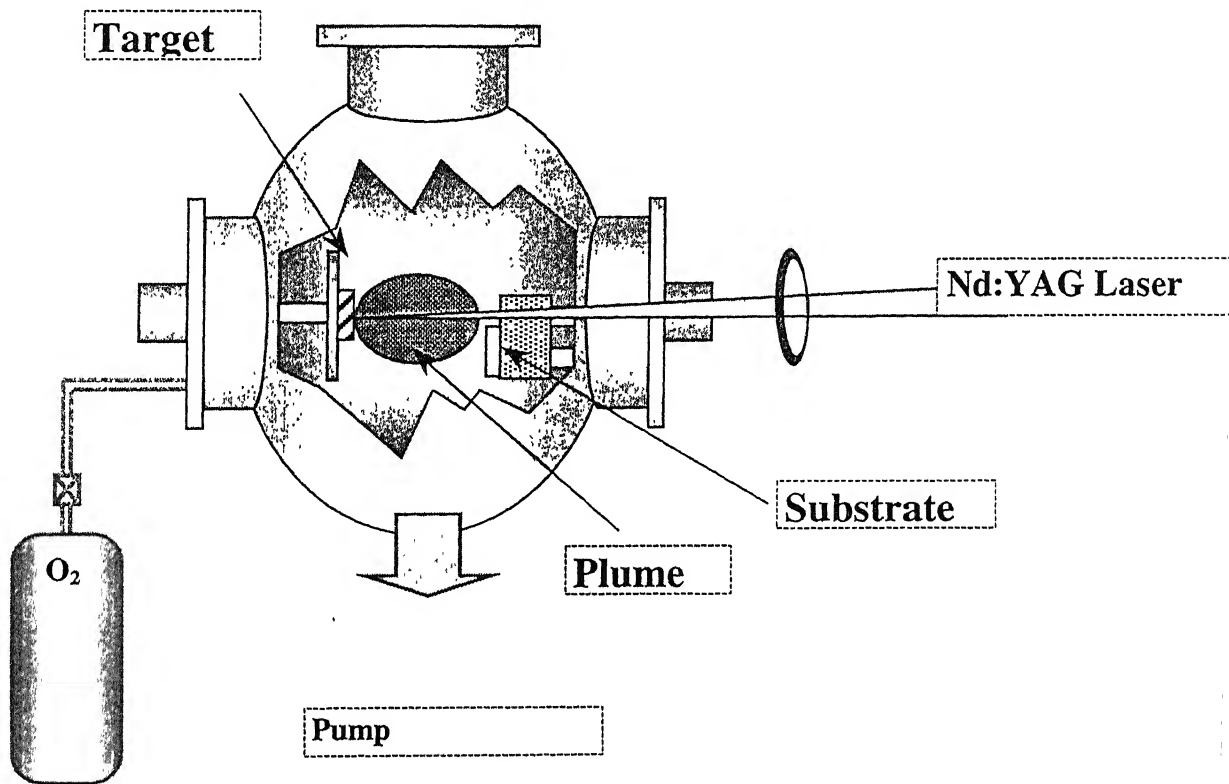


Figure 2- 1: Experimental Set up for Pulsed Laser Deposition of Thin Films.

## 2.2 Characterization of Deposited Thin Films

A brief description of each of the technique viz; X-ray diffraction, Atomic Force Microscopy (AFM), Photoluminescence (PL) and Rutherford Backscattering (RBS) used for characterizing pulsed laser deposited ZnO thin films is given below.

### 2.2.1 X-ray diffraction

The crystalline structure and particle size of pulsed laser deposited thin films was measured using x-ray diffraction. In this instrument, essentially a monochromatic radiation ( $\text{CuK}\alpha$ ,  $1.548 \text{ \AA}$ ) is used. X-rays can be diffracted from different planes of the crystal whenever the Bragg condition  $\lambda = 2d_c \sin \theta$  is satisfied, where  $d_c$  is the spacing between the crystal planes,  $\lambda$  is the wavelength of the x-rays and  $\theta$  is the angle at which the x-rays are diffracted. A general relation obtained by combining the Bragg's law and the plane spacing equation is used for predicting the diffraction angle for any set of planes [80]. For example for a cubic crystal,

$$\lambda = 2d_c \sin \theta \quad \text{and} \quad \frac{1}{d_c^2} = \frac{(h^2 + k^2 + l^2)}{a^2}.$$

Combining these equations, we get

$$\sin^2 \theta = \frac{\lambda^2}{4a^2} (h^2 + k^2 + l^2) \quad (2.1).$$

This equation predicts, for a particular incident wavelength  $\lambda$ , a particular cubic lattice of lattice parameter  $a$  for all the possible Bragg angles at which diffraction can occur from the planes  $(h \ k \ l)$ . Figure 2.2 shows a typical X-ray diffraction spectrum of pulsed laser deposited ZnO film.

A rough estimate of the particle size is made from the width (FWHM)  $B$  of the x-ray diffraction curve. As a first approximation for measuring  $B$  we take half the difference between the two extreme angles at which the intensity is zero,

$$B = \frac{1}{2} (2\theta_1 + 2\theta_2) = \theta_1 - \theta_2. \quad (2.2)$$

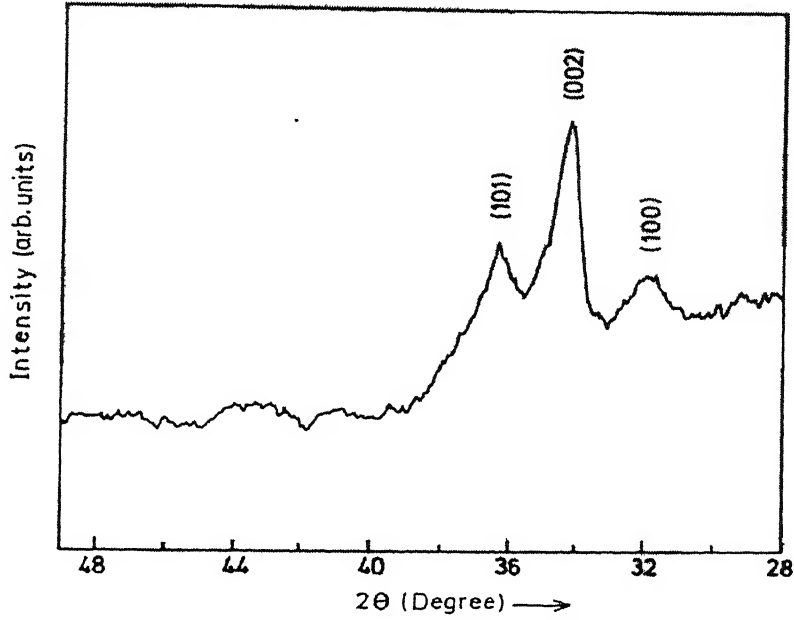


Figure 2- 2: Typical XRD spectrum of ZnO thin film

The path-difference equations for these two angles are

$$2b \sin \theta_1 = (m+1)\lambda \quad (2.3),$$

$$2b \sin \theta_2 = (m-1)\lambda \quad (2.4)$$

where  $b$  is the size of the crystal.

From equations. 2.3 and 2.4 we get

$$b(\sin \theta_1 - \sin \theta_2) = \lambda, \quad (2.5)$$

$$2b \cos\left(\frac{\theta_1 + \theta_2}{2}\right) \sin\left(\frac{\theta_1 - \theta_2}{2}\right) = \lambda \quad (2.6).$$

Since  $\theta_1$  and  $\theta_2$  both are very nearly equal to  $\theta_B$ , we can write

$$\theta_1 + \theta_2 = 2\theta_B \quad (\text{approx.})$$

and

$$\sin\left(\frac{\theta_1 - \theta_2}{2}\right) = \left(\frac{\theta_1 - \theta_2}{2}\right) \quad (\text{approx.}) \quad (2.7)$$



Therefore,

$$2b\left(\frac{\theta_1 - \theta_2}{2}\right)\cos\theta_B = \lambda \quad (2.8),$$

A more exact treatment gives the size 'b' of the crystallite as,

$$b = \frac{0.9\lambda}{B \cos \theta_B} \quad (2.9)$$

This expression is known as Scherrer formula [80]. We have used equation (2.9) to estimate the size of crystallites of ZnO [56].

### 2.2.2 Atomic Force Microscopy

In 1986, Gerd Binnig and Heinrich Rohrer shared the Nobel Prize in Physics for inventing the scanning tunneling microscope and discovering that it can image individual surface atom with unprecedented resolution [81]. The success of scanning tunneling microscope has led to the invention of a host of other "scanning probe" microscopes, which rely on mechanically scanning a sharp tip over a sample surface. The atomic force microscope is one of the most successful of these new devices. One of the most exciting results from atomic force microscopy has been the discovery that atomic resolution can be achieved when the tip is in contact with the sample while scanning [82]. AFM has an additional advantage that insulating samples could be imaged unlike the case of scanning tunneling microscope. The concept of using a force to image a surface is a general one and can be applied to magnetic and electrostatic force as well as to inter atomic interactions between the tip and the sample. Whatever the origin of the force, all force microscopes have five essential components,

1. A sharp tip mounted on a soft cantilever spring
2. A way of sensing the cantilever's deflection
3. A feedback system to monitor and control the deflection (and hence the interaction force)
4. A mechanical scanning system that moves on the surface of the sample with respect to the tip in a raster pattern
5. A display system that converts the measured data into an image

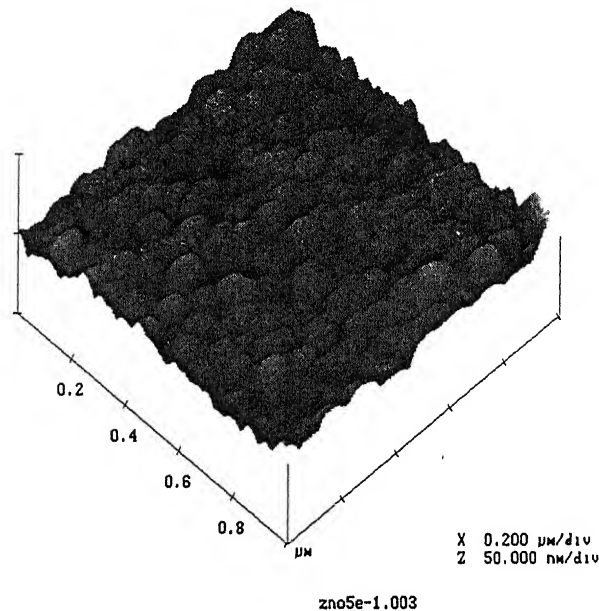


Figure 2- 3: 3-D topography of PLD ZnO film

The scanning, feedback and display systems are very similar to those used for scanning tunneling microscopy (STM). Although the basic elements of all force microscopes are similar, the details of implementation vary. The original AFM, for example, used a handmade cantilever spring formed from a piece of gold foil approximately 1 mm long. A small diamond stylus glued to the foil served as the tip. Today the most advanced AFM uses cantilevers micro-fabricated from silicon, silicon dioxide or silicon nitride using photolithographic techniques. Typical lateral dimensions are on the order of 100 microns with thickness of order of 1 micron. This geometry gives spring constants in the range of 0.1-1 N/m and resonant frequencies of 10-100 KHz. The cantilever can be fabricated with integrated tips, or else small diamond chips can be glued on by hand force. We have used AFM (Nanoscope III) from Digital Instruments. Figure 2.3 shows a 3-D AFM topography of one of our PLD ZnO film.

### 2.2.3 Photoluminescence and Random Lasing Action

The operation of almost all opto-electronics devices is based on the creation or annihilation of electron-hole pairs. Pair formation essentially involves raising an electron in energy from valence band to conduction band, thereby leaving a hole behind in the valence band. In principle, any energetic particle incident on a semiconductor, which can impart an energy at least equal to the band gap energy to a valence band electron, will create pairs. With respect to the bonding in lattice, this process is equivalent to breaking a covalent bond. The simplest way to create electrons hole pairs is to irradiate the semiconductor with photons. Photons with sufficient energy will be absorbed and impart their energy to the valence band electrons and raise them to the conduction band as shown in figure 2.4 (a). This process is, therefore, also called absorption. The reverse process, that of electron and hole recombination, is associated with the pair giving up its excess energy. Recombination may be non-radiative or radiative. In a non-radiative transition, the excess energy is dissipated as heat. In a radiative transition, the excess energy is dissipated as photons as shown in figure 2.4 (b), usually having energy equal to or less than the band gap. This is the luminescent process and is classified according to the method by which the electron-hole pairs are created. Photoluminescence involves the radiative recombination of electron-hole pairs created by injection of photons.

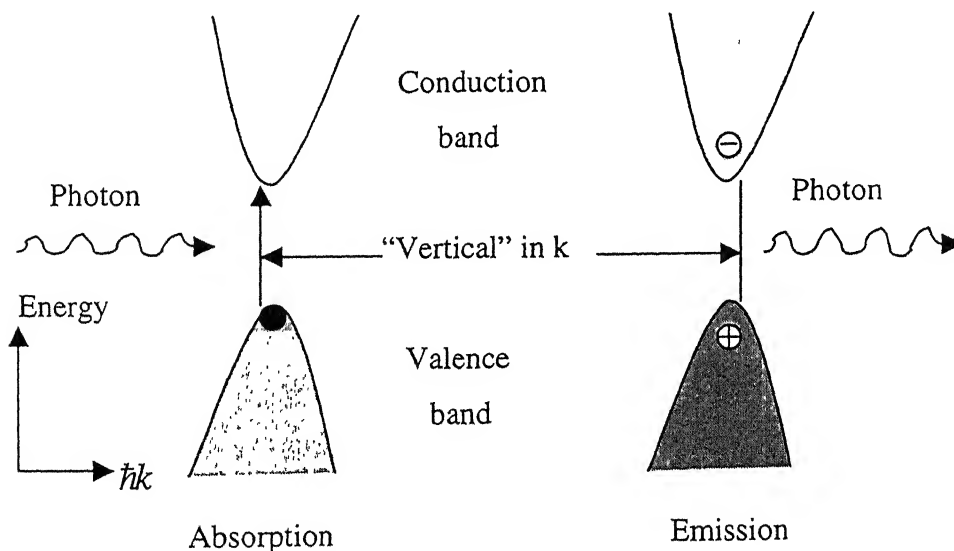


Figure 2- 4: Light emission (a) and absorption (b) by a semiconductor

For strong optical emission one needs to conserve the momentum  $\hbar k$  for the electrons and the photon system. The photons  $k_{ph}$  value is given by  $k_{ph} = 2\pi / \lambda$ . Since 1 eV photons correspond to a wavelength of 1.24  $\mu\text{m}$ , the equivalent  $k$  value is  $\sim 10^{-4} \text{ \AA}^{-1}$ , essentially zero compared to the  $k$  values for electrons. Thus  $k$  conservation ensures that the initial and final electrons should have the same  $k$  value. In other words, only “vertical”  $k$  transitions as shown in Figure 2.4. Because of this constraint of  $k$  conservation, in semiconductors where the valence band and conduction band edges are at the same,  $k=0$  value (the direct band gap semiconductor) the optical transitions are quite strong e.g. GaAs, GaN, GaP, InP. In indirect material like Si, Ge etc. the optical transitions are very weak and require the help of lattice vibrations to satisfy  $k$ -conservation. This makes a tremendous difference in the optical properties of these two materials.

In order to observe photoluminescence and lasing action in ZnO we used the third harmonic (355 nm, pulse width 5 ns) of Nd:YAG laser for optical pumping. PL is essentially a spontaneously emitted light. Third harmonic of the Nd:YAG (355 nm (3.35 eV)) can be effectively used for optical excitation of ZnO which has a direct band gap of 3.39 eV. Figure 2.5 shows a schematic layout used for PL experiments. Lasing action can also be observed by optical pumping if an optical feedback can be provided. However, the rate of stimulated emission must exceed the rate of spontaneous emission. The same experimental set up was used for observing laser action in ZnO. The optical feedback is provided by strong scattering of light by ZnO crystallites. The sample was kept on a rotating table in order to observe lasing at different angles. Light coming from the sample was collected through a fiber and fed to the entrance slit of the monochromator (Jobin Yvon, HRS-2).

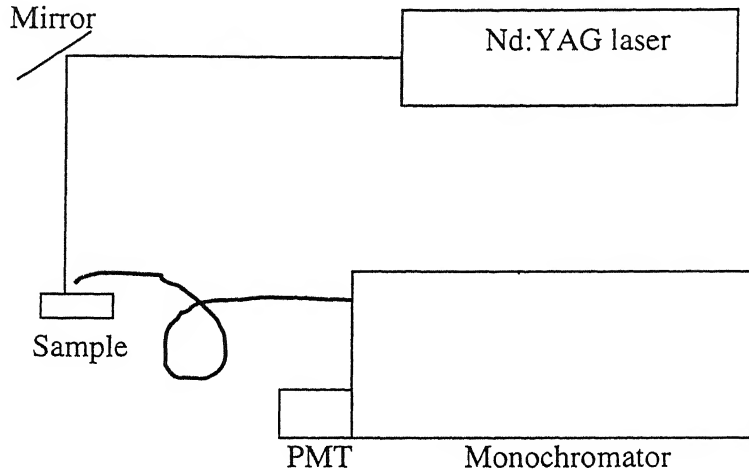


Figure 2- 5: Experimental set up for Photoluminescence and Random Laser Action

### 2.2.4 Coherent Backscattering

Coherent backscattering (CBS) of light is a phenomenon in which partial waves traversing time-reversed paths interfere constructively in the backscattering direction leading to the appearance of an intensity cone. In order to understand the origin of the enhanced intensity cone, we consider a case of photon scattering in a colloidal suspension. The simplest model describing this process assumes that the photons are undergoing a diffusion like random walk with an average step size given by the transport mean free path  $l^*$  which is equal to scattering mean free path  $l_s$  for isotropic medium. Since light is an electromagnetic wave, and not a classical particle, interference between scattering paths must be considered. It is this interference between time reversed paths that gives rise to the CBS intensity cone. Figure 2.6 shows a prototypical scattering path and its time-reversed mate with incident light direction  $\hat{k}_1$  and final direction  $\hat{k}_2$ . Five scattering centers are shown with positions given by  $\vec{r}_1$  through  $\vec{r}_n$ , relative to an arbitrary origin. The intermediate scattering vectors  $\hat{k}'_s$  are not labeled for clarity. The optical path length difference between these two time-reversed scattering paths only depends on the physical path length difference  $d_2 - d_1$ . The scattering angle  $\theta$ , relative to the backscattered direction  $-\hat{k}_1$  is also shown.

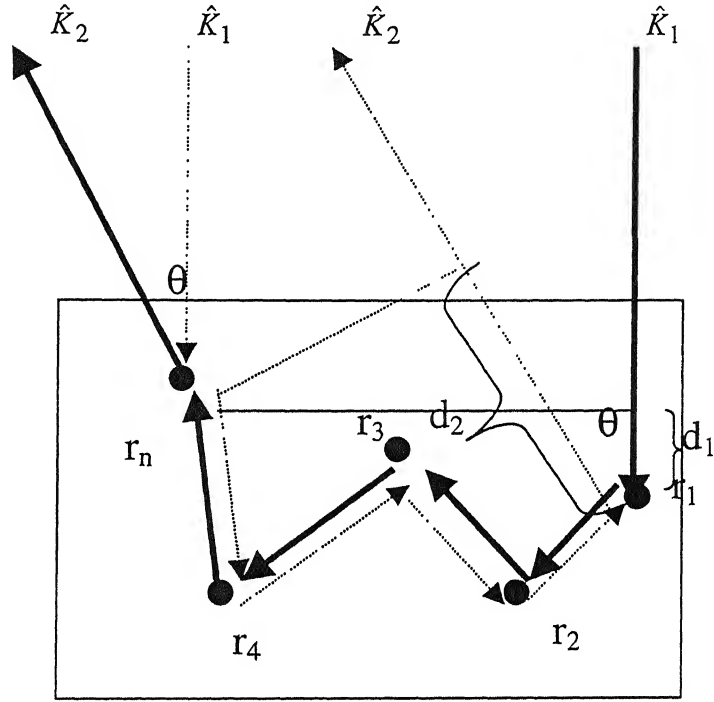


Figure 2- 6: Schematic path followed by an incoming and scattered light from random medium

The nature of the interference between the time reversed scattering paths depends on the phase difference between the two scattering waves. This phase difference is given by,

$$\Delta\phi = \frac{2\pi}{\lambda} (\text{path length difference}) = \frac{2\pi}{\lambda} (d_2 - d_1) \quad (2.10)$$

where  $\lambda$  is the wavelength of the incident radiation in the medium, the distance  $d_1$  is the projection of the vector that points  $\vec{r}_1$  to  $\vec{r}_n$  that is  $(\vec{r}_n - \vec{r}_1)$  onto  $-\hat{k}_1$ , and the distance  $d_2$  is the projection of vector  $(\vec{r}_n - \vec{r}_1)$  onto  $\hat{k}_2$ . The distances  $d_1$  and  $d_2$  are thus given by,

$$\begin{aligned} d_1 &= -\hat{k}_1 \cdot (\vec{r}_n - \vec{r}_1) , \\ d_2 &= \hat{k}_2 \cdot (\vec{r}_n - \vec{r}_1) \end{aligned} \quad (2.11)$$

$\therefore$  Equation (2.10) yields a phase difference of,

$$\Delta\phi = \frac{2\pi}{\lambda} (\hat{k}_2 + \hat{k}_1) \cdot (\vec{r}_n - \vec{r}_1) \quad (2.12)$$

It follows from, equation (2.12), that for light scattered directly into the backward direction,  $\hat{k}_2 = -\hat{k}_1$ , the phase difference between a scattering path and its time reversed mate is zero, and thus constructive interference results.

The qualitative nature of the interference away from the exact backscattering direction can be ascertained by making use of diffusive model of photon transport within the colloidal suspension [83]. On evaluating the dot product in equation (2.12), the phase difference becomes,

$$\Delta\phi = \frac{2\pi}{\lambda} 2 \sin(\theta / 2) R \cos\alpha \quad (2.13)$$

where  $\theta$  is the scattering angle measured from the backscattering direction,  $R$  is the  $|\vec{r}_n - \vec{r}_1|$ , and  $\alpha$  is the angle between  $(\hat{k}_2 + \hat{k}_1)$  and  $(\vec{r}_n - \vec{r}_1)$ , where we have used  $|\hat{k}_2 + \hat{k}_1| = 2 \sin(\theta / 2)$ . Restricting the analysis to the experimentally obtained small  $\theta$  (milli-radians), equation (2.13) reduces to

$$\Delta\phi \approx \frac{2\pi}{\lambda} \theta R \quad (2.14)$$

where we have also used the fact that for a dense colloidal suspension  $(\vec{r}_n - \vec{r}_1)$  will be nearly parallel to the sample surface and  $(\hat{k}_2 + \hat{k}_1)$ , yielding  $\cos\alpha \approx 1$ . The mean square separation between the first and last scatter in the photon diffusion approximation [83] is given as,

$$\langle R^2 \rangle = 6Dt = 6\left(\frac{cl_s}{3}\right)t, \quad (2.15)$$

where  $D$  is the photon diffusion coefficient in the colloidal suspension,  $t$  is the random-walk time, and  $c$  is the velocity of light propagation. Using the root-mean-square value for  $R$  we obtain the final expression for the phase difference as

$$\Delta\phi \approx \frac{2\pi}{\lambda} \theta \sqrt{6\left(\frac{cl_s}{3}\right)t} = \frac{2\pi}{\lambda} \theta \sqrt{2l_s s} \quad (2.16)$$

where  $s=ct$ , the total scattering mean free path length.

In order for the two partial waves that traverse time reversed paths to add constructively, their phase difference must be small. This coherence condition may be

stated as  $\Delta\phi/(2\pi) \ll 1$ . Thus, there exists a critical angle  $\theta_c$  below which this condition will be satisfied and phase coherence maintained. The critical angle is given by

$$\theta_c \approx \frac{\lambda}{\sqrt{2l_s s}} \quad (2.17)$$

This result has important implications for the shape of the coherent backscattering cone and accounts for the cone enhancement factor. the resultant intensity due to the interference between the incoming and outgoing beam will be,

$$I = I_1 + I_2 + 2\sqrt{I_1 I_2} \cos(\Delta\phi) \quad (2.18)$$

As mentioned earlier, equation (2.12) implies that the two partial waves must be added coherently i.e.  $\Delta\phi = 0$  in exactly backscattering direction. Assuming an equal intensity for counter propagating beams  $I_1=I_2$ , where  $I_1$  and  $I_2$  are intensities corresponding to incident and scattered waves equation (2.18) becomes,

$$I = 4I_1 \quad (\text{for constructive interference}) \quad (2.19)$$

Where as incoherent sum may be used for the angles greater than  $\theta_c$ , leading to the intensity given by,

$$I = I_1 + I_1 = 2I_1 \quad (\text{for no interference}) \quad (2.20)$$

Ratio of the intensities (equations (2.19) and (2.20)) shows that the maximum coherent backscattering enhancement factor is 2, i.e. the ratio of maximum cone height to background level, is two. Another important result that follows from equation (2.17) is the dependence of the coherent cone width on the scattering mean free path. The angular cone width of the critical coherence angle is maximum for the smallest total path length. If  $s=l_s$ , is the smallest average path length, cone width becomes,

$$\theta_{\max} \approx \frac{\lambda}{\sqrt{2l_s}} \quad (2.21)$$

An analytical expression for the coherent backscattering intensity line shape may be obtained within the diffusion approximation [84] and is given by,

$$\alpha(\theta) = \frac{3}{8\pi} \left( 1 + \frac{2z_0}{l_s} + \frac{1}{(1 + q_{\perp} l_s)^2} \left( 1 + \frac{1 - \exp(-2q_{\perp} z_0)}{q_{\perp} l_s} \right) \right) \quad (2.22)$$

where  $\alpha(\theta)$  is the albedo, defined as the ratio of the intensity of the scattered light to the incident light i.e.  $\alpha(\theta)=I_2/I_1$ , where  $I_1$  ( $I_2$ ) is the incident (scattered) light intensity,  $l_s$  is the



light mean free path,  $q_{\perp} \cong 2\pi(\theta)/\lambda$ ,  $\lambda$  is the probing light wavelength,  $z_0$  is the mean distance from the surface to the first scatter. Using our experimental values we estimate  $z_0 \cong 0.7l_s$ . Figure 2.7 shows the theoretical coherent backscattering curve from the equation (2.22), ( $\lambda=0.6328 \mu\text{m}$ ,  $l_s=8 \mu\text{m}$ ) for ZnO thin film. These values of  $l_s$  are extracted from experimental curves in figure 2.9

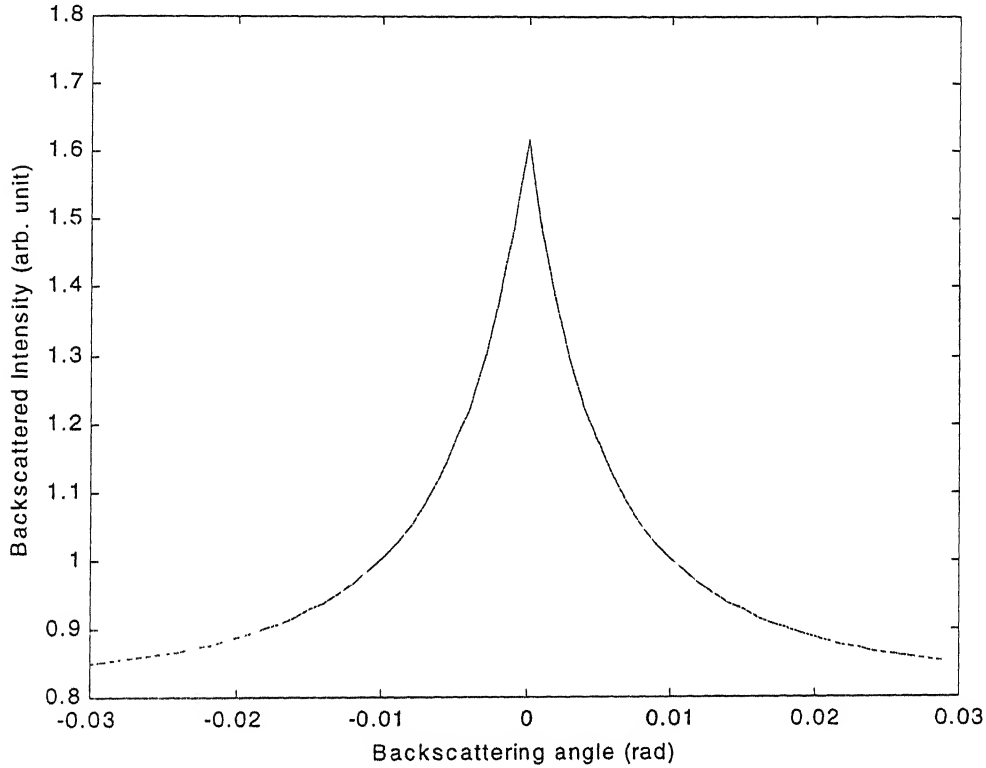
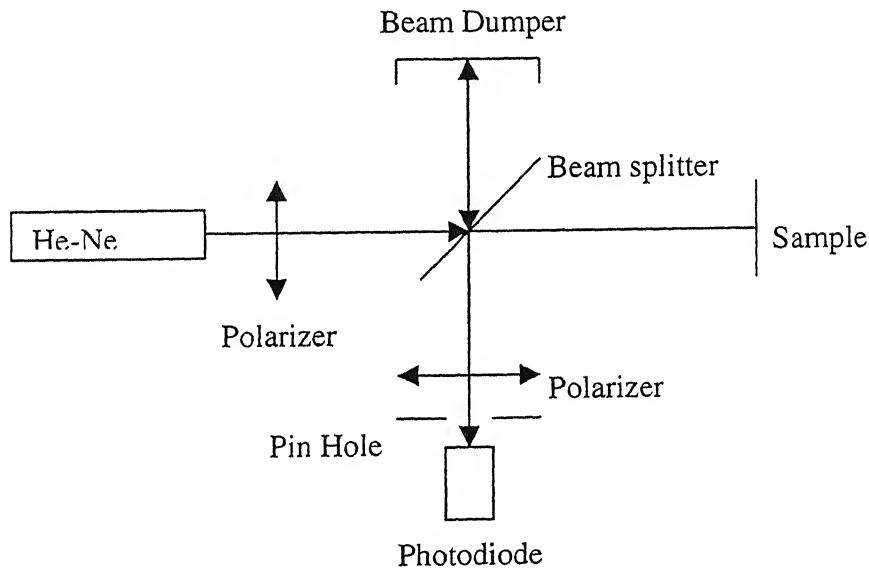


Figure 2- 7: Theoretical curve of equation (2.22) for ZnO thin film.

#### 2.2.4.1 Coherent backscattering from pulsed laser deposited ZnO thin films

We have used CBS to measure the optical scattering mean free path. The experimental setup used, shown in figure 2.8, is similar to that of a Michelson interferometer with one of its arm blocked with a beam dumper. A low power He-Ne laser (1 mW) is used as the light source. The laser beam is expanded to about 3 cm to reduce the divergence of the beam. The He-Ne laser light passes through the beam splitter (50:50) and reflected back from the sample. Another part of the light is simply

dumped into the beam dumper. Single scattering from the sample can be suppressed by using a polarizer and an analyzer. The unpolarized light from the laser will become vertically polarized after passing through the polarizer. The reflected light from the sample can pass through the analyzer only if it is vertically polarized whereas the horizontally polarized light that can generate from single scattering is suppressed. The reflected light is focused by a convex lens through a 200  $\mu\text{m}$  pinhole onto the photodiode placed on a micro-positioner. This geometrical configuration gives an experimental angular resolution of approximately 0.4 mrad, sufficient to resolve coherent cones. The scattering mean free path  $l_s$  is estimated using the formula  $\theta \approx \lambda/\sqrt{2}l_s$ , where  $\lambda$  is the wave length of the incident light [85].



**Figure 2- 8: Experimental Set up for Coherent Backscattering Experiment**

The theoretically expected enhancement factor of 2 is very difficult to realize. This may be due to several factors, for example, the finite sample size, angular resolution, failure to eliminate complete single scattering and the presence of closed loop scattering paths. Figure 2.9 shows the coherent backscattering spectrum obtained from ZnO pellet. We have estimated the value of scattering mean free path from the width of the cone using the equation (2.21). From the angle of the cone we get  $l_s = 0.238 \mu\text{m}$  ( $\approx 0.6\lambda$ ). Figure 2.10 shows the coherent backscattering spectrum for ZnO thin film. For film we got  $l_s = 8 \mu\text{m}$ , which is much larger than that of ZnO pellet.

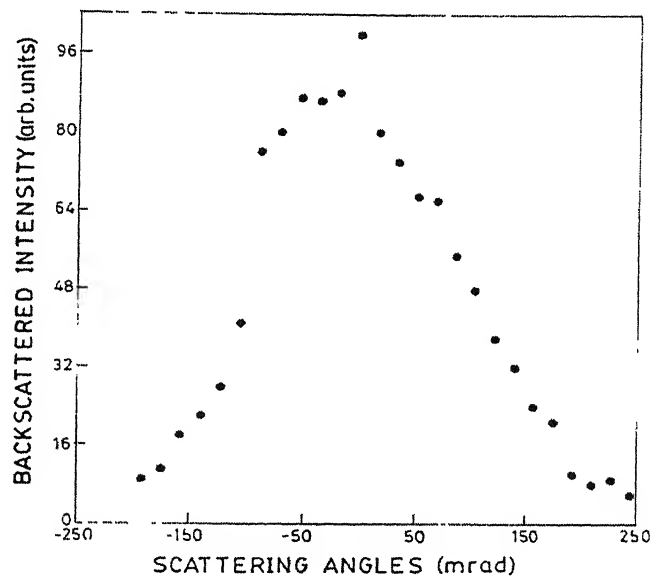


Figure 2- 9: Coherent backscattering spectrum from a ZnO pellet

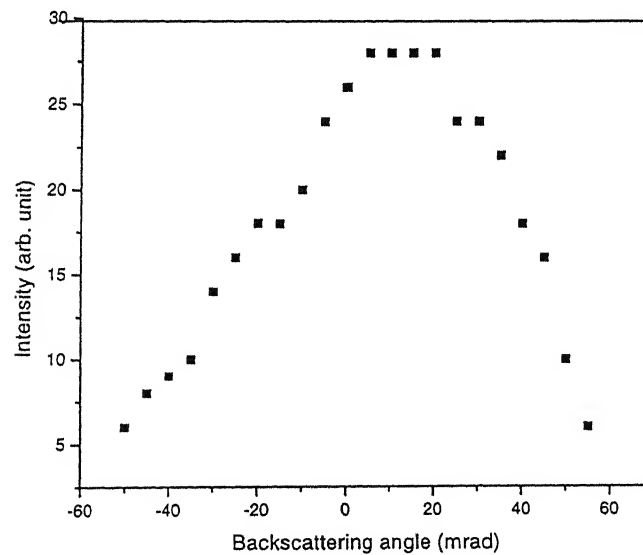


Figure 2- 10: Coherent backscattering spectrum from a ZnO thin film

### 2.2.5 Rutherford Backscattering

Rutherford Backscattering Spectrometry [86] technique is a well established technique for determining the composition at the interface of two layers, identifying the mass of the impurity and the host atoms and the thickness of the film etc. RBS is well suited for characterization of thin films or near surface region of bulk samples especially when the sample contains atoms of heavier species. In general,  $H^+$ ,  $He^+$  etc. ions in the energy range of 0.5 to 3.0 MeV are used for RBS. The well-collimated ion beam of size  $1\text{ mm}^2$  is made to impinge on the surface of the sample at an angle to the surface normal. The backscattered particles are detected using a semiconductor detector (EG & G ORTEC, USA) subtending a small solid angle. The frequency of occurrence of the scattering as a function of energy of the backscattered particles, known as spectrum is recorded by multichannel analyzer. In our study we have used 1.23 MeV  $He^+$  beam obtained from 2 MeV Van De Graff accelerator facility at IIT, Kanpur. Experiments were performed in a clean vacuum of better than  $10^{-6}$  Torr. The RBS spectrum was analyzed using RUMP simulation software [87]. In simulation, first a theoretical sample structure consisting of several layers of varying thickness is prepared. A backscattering spectrum is then constructed using the sample structure and the experimental parameters. The theoretical profile is then compared with that of the experimentally obtained RBS spectrum. The procedure is utilized in an iterative manner to arrive at the best set of parameters using which the given sample spectrum compares quite well with the experimental spectrum. We used RBS to estimate stoichiometry and thickness of the deposited films. Figure 2.11 shows the RBS spectrum of PLD ZnO film.

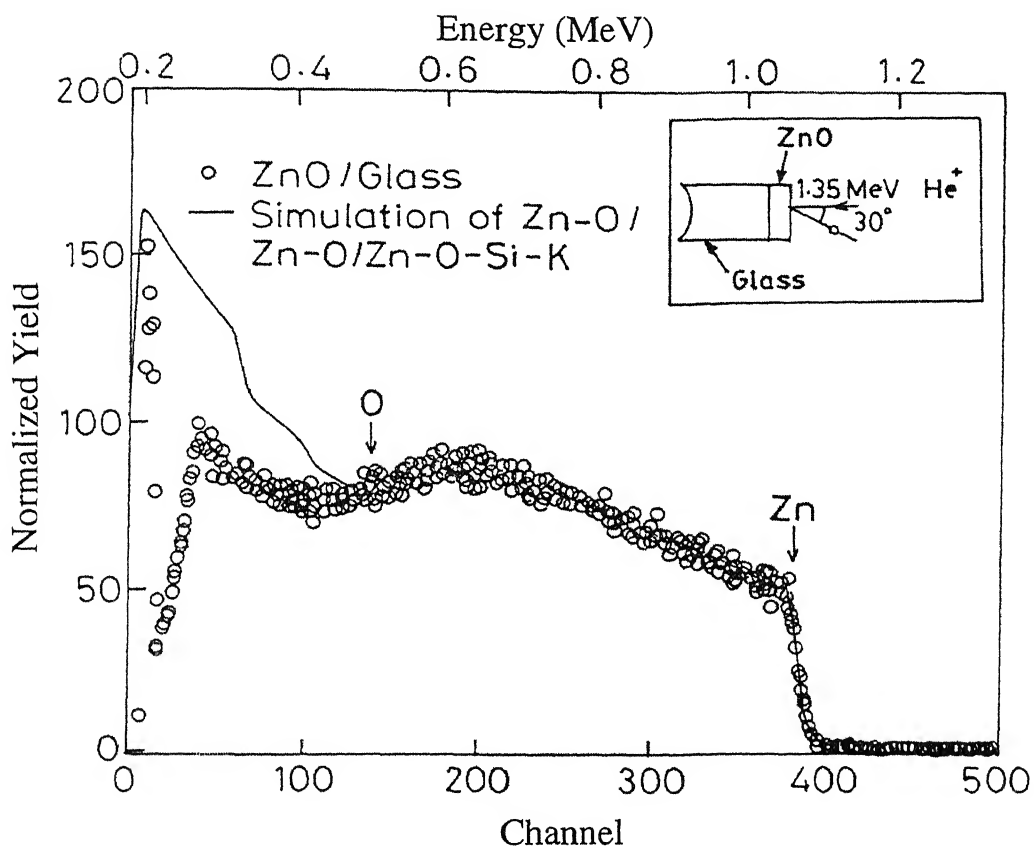


Figure 2- 11: Typical RBS spectrum of PLD ZnO thin film. Inset shows the direction of  $\text{He}^+$  beam and detection angle.

## Chapter 3

### Synthesis and characterization of ZnO thin films for UV laser

---

PLD is a useful technique as one can easily change several controlling parameters for optimization of the condition for deposition of good quality films since 1982. There are several reports of pulsed laser deposited ZnO thin films. Pressure of the ambient gas, choice of substrate, substrate temperature, pulse width of the laser are amongst the important parameter for deposition of good quality thin films. By tuning the oxygen pressure during the initial and final growth stages, smooth and epitaxial ZnO thin films with high optical quality, high electron mobility, and low background carrier concentration have been obtained. The effect of substrate (glass, silicon, GaAs, and sapphire) on quality of ZnO thin films has been reported by several groups [13-15]. The enhancement of PL of green band for film deposited on Si has been observed [88,89]. Recently there have been a few reports on femtosecond pulsed laser deposition of ZnO thin films [90-92].

In order to deposit better quality films, it is necessary to understand the basic processes taking place during laser-target interaction, interaction of plasma with laser and with the ambient atmosphere, and plasma-substrate interaction. In the following section a brief summary of physical processes taking place during laser-plasma interaction is given.

#### 3.1 Physical Processes

To investigate the physics and theoretical nature of the laser deposition process, the evaporation of the target material, formation of high temperature plasma by absorption of the laser energy by the evaporated material, and the expansion of the plasma resulting in the deposition of the thin film is considered in detail. The interaction process can be divided into three separate regimes;

- (a) interaction of the laser beam with the solid target resulting in evaporation of the surface layer.
- (b) interaction of the evaporated material with the incident laser beam resulting in an

isothermal plasma formation and expansion.

- (c) anisotropic adiabatic expansion of the plasma leading to the film deposition process.

The first two regimes start with the laser pulse and continue until the laser pulse terminates. Third regime starts after the termination of the laser pulse. Figure 3.1 shows different interaction regions of the laser with the target, plasma plume and substrate.

**(a) Laser solid interaction:**

The laser solid interaction can be divided into two regimes:

- (i) the interaction of high-intensity laser pulses with a solid target
- (ii) interaction of the laser beam with the evaporated material from the target material

In the first regime the main physical processes involved are heat conduction, melting, and vaporization of the target. In the second regime the density and temperature of the laser-produced plasma can be so high that an efficient shielding of the target occurs during the laser pulse. The properties of the laser-ablation process in this case are strongly influenced by both laser plasma coupling and plasma kinetics.

Several authors have analyzed the laser plasma interaction in the first regime. Most of the reported work deals with nanosecond laser-solid interaction. In nanosecond laser heating of the target, laser energy is first absorbed by the target that heats up the target up to the melting point and then to the vaporizing temperature. The evaporation occurs from the liquid metal, and heat conduction into the solid target is the main source of energy loss. The vaporizing process is often described using the heat flow equation in one dimension (1-D), as appropriate for many experimental conditions [93,94];

$$\rho c \frac{\partial T}{\partial t} = \frac{\partial T}{\partial z} \left( k \frac{\partial T}{\partial z} \right) + \alpha_{ab} A_{ab} I_0 \exp(-\alpha_{ab} z) \quad (3.1)$$

where  $T, \rho, c, k, A_{ab}$  and  $\alpha_{ab}$  are temperature, density, specific heat, thermal conductivity, surface absorbance and absorption coefficient respectively of the target, while  $I_0$  is the intensity of the incident laser pulse, and  $z$  the coordinate normal to the target. The nonlinear boundary conditions for vaporization and the presence of a moving solid-liquid interface make exact solutions of equation (3.1) very difficult. Consequently, numerical approaches are always considered. The evaporation rate is calculated using the Clausius-

Clapiron equation by assuming that the liquid is in thermal equilibrium with its saturated vapor (normal vaporization). Detailed analysis of different vaporization mechanisms contributing in nanosecond laser-solid interaction have been reported by Kelly and Miotello [95]. They have shown that for sufficiently high laser fluences, phase explosion (or explosive boiling) can occur. This mechanism involves homogenous nucleation when the target temperature reaches a value close to the material thermodynamic critical temperature  $T_c$ . As a result, the hot region near the target surface undergoes a rapid transition in a very short time from a superheated liquid to a mixture of vapor and liquid droplets.

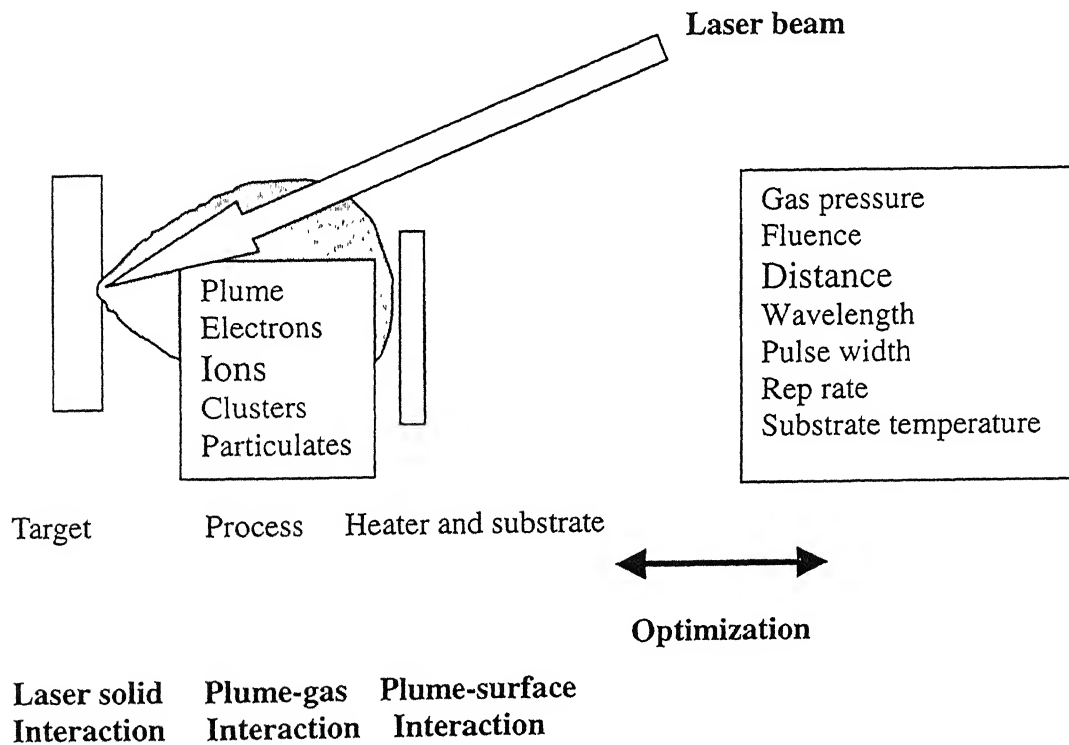


Figure 3- 1: Different region of Laser Plasma Interaction

### (b) Interaction of laser beam with evaporated material

The high surface temperature induced by laser irradiation leads to emission of positive ions and electrons from a free surface. The flux of ions and electrons as a function of temperature can be predicted from Saha equation:

$$n_i = (2.4 \times 10^{15} T^{3/2} n_n e^{-U_i/k_B T})^{1/2} \quad (3.2),$$



where  $T$  is the gas temperature in K,  $n_i$  and  $n_n$  is the density of ions and neutrals in  $\text{cm}^{-3}$  respectively, and  $U_i$  is the first ionization potential of the gas atoms in eV. Once the plasma is formed, the incoming laser radiation is absorbed by the process known as inverse bremsstrahlung. The absorption coefficient of inverse bremsstrahlung of this cloud to radiation of frequency  $\nu$  (in Hz) is given by [96],

$$\alpha_{IB} = 3.7 \times 10^8 \frac{Z^3 n_i^2}{T^{1/2} \nu^3} (1 - e^{-h\nu/k_B T}) \quad (3.3),$$

where  $Z$  is the elemental charge of the ion,  $n_i$  is in  $\text{cm}^{-3}$  and  $\alpha_{IB}$  is absorption coefficient of inverse bremsstrahlung in  $\text{cm}^{-1}$ . The term  $[1 - \exp(-h\nu/k_B T)]$  represents the loss term due to stimulated emission which depends on the plasma temperature and laser frequency. For  $1.06 \mu\text{m}$  laser wavelength, the exponential term becomes unity for  $T < 13600 \text{ K}$  and can be approximated by  $h\nu/k_B T$  for  $T > 13600 \text{ K}$ . The absorption term shows a  $T^{0.5}$  dependence for low temperature and  $T^{1.5}$  dependence for high temperature. The dependence of frequency also changes from  $\nu^2$  to  $\nu^3$  depending on the value of  $(h\nu/k_B T)$ . As the cloud absorbs via inverse bremsstrahlung it becomes hotter, more ionized, and in turn absorb more efficiently. Equation (3.3) shows that the rate of absorption depends on  $n_i^2$ . This results in increase in kinetic energy of the electrons which increases collisional frequency. The energy absorbed by the electron will be transferred to ions by ions-electrons collisions. The ions get more and more ionized resulting in increase in electron density. However, this process cannot go on indefinitely. The electromagnetic wave (laser) propagating through the plasma obeys the dispersion relation;

$$\omega_L^2 - \omega_p^2 = k^2 c^2 \quad (3.4)$$

$$\omega_p = \left( \frac{4\pi n_e e^2}{m_e} \right)^{1/2} \quad (3.5)$$

where  $\omega_L$  is the frequency of the laser light,  $k$  the propagation vector,  $c$  the velocity of light,  $e$  the electron charge,  $n_e$  the electron density,  $m_e$  the electron mass and  $\omega_p$  is the plasma frequency. For  $\omega_L > \omega_p$ ,  $k$  is real and the electromagnetic field propagates whereas for  $\omega_L < \omega_p$ ,  $k$  is imaginary and wave does not propagate. At  $\omega_L = \omega_p$ , reflection of light occurs at a density called the critical density,  $n_c = m_e \omega_L^2 / 4\pi e^2$ .

At the beginning of the inverse bremsstrahlung process  $\omega_L \gg \omega_p$  and the rate of absorption depends on  $n_i^2$ . The absorbed energy causes an increase in the kinetic energy of the electrons i.e. an increase in electron temperature which in turn produces further ionization with a consequent increase in  $n_e$  and eventually approaches  $n_c$  the critical density. The critical density extends across a plane surface to some distance into the plasma. The value of  $n_c$  is  $3.15 \times 10^{21}/\text{cm}^3$  for  $1.06 \mu\text{m}$  wavelength laser light from Nd:YAG laser. At this density the plasma becomes opaque to the incoming radiation and causes laser light to get reflected. Laser light can no longer reach the target surface to generate new plasma. However, plasma growth does not cease. Because of the heating that follows the absorption of energy by inverse bremsstrahlung, the plasma is driven rapidly away from the target surface resulting in a decrease in electron density and laser light again reaches the surface. The energy absorbed by the electron equilibrates very rapidly so that a well defined electron temperature is reached. The energy gained by the electrons is also shared with ions in collisions. These processes do not take place discontinuously but merge into a self-regulating regime with the generation, heating and expansion of plasma taking place through out the pulse. The expanding plasma generates pressure which drives a shock wave into the solid material.

In the initial stages of plasma expansion when the particle density is of the order of  $10^{19}$ - $10^{20}/\text{cm}^3$ , the mean free path of the particles is short, and hence the plasma behaves as a continuum fluid. The equation of gas dynamics can be applied to simulate its expansion [96];

$$\frac{\partial n}{\partial t} + \nabla \cdot (nv) = 0 \quad (3.6)$$

$$nm\left(\frac{\partial v}{\partial t}\right) + (v \cdot \nabla)v = -\nabla P \quad (3.7)$$

where  $n$  is the number density,  $m$  is the mass of the particle,  $v$ , the velocity and  $P$  is the pressure. For the duration of laser pulse the plasma temperature can be taken to be constant i.e., the expansion is an isothermal one. The density ( $n$ ) of the plasma at any point ( $x, y, z$ ) at time  $t$  can be expressed as a Gaussian function given by [97]

$$n(x, y, z, t) = \frac{N_T t}{\sqrt{2\pi}^{1.5} \tau_L X(t)Y(t)Z(t)} \exp\left[-\frac{x^2}{2X(t)^2} - \frac{y^2}{2Y(t)^2} - \frac{z^2}{2Z(t)^2}\right] \quad (3.8)$$

where  $N_T$  is the total number of ablated species at  $t=\tau_L$  (pulse width).  $X(t)$ ,  $Y(t)$  and  $Z(t)$  are the dimensions of the expanding plasma in three orthogonal directions. Assuming plasma to be an ideal gas, the pressure at any point can be expressed as

$$P(x, y, z, t) = n(x, y, z, t)k_B T \quad (3.9)$$

It has been shown that gas dynamics equations follow similarity transformation in which the velocity can be expressed as

$$X(t)\left[\frac{1}{t}\frac{dX}{dt} + \frac{d^2X}{dt^2}\right] = Y(t)\left[\frac{1}{t}\frac{dY}{dt} + \frac{d^2Y}{dt^2}\right] = Z(t)\left[\frac{1}{t}\frac{dZ}{dt} + \frac{d^2Z}{dt^2}\right] = \frac{k_B T}{m} \quad t \leq \tau_L \quad (3.10)$$

where  $T_0$  is the isothermal temperature of the plasmas. The above equation determines the initial expansion of three orthogonal plasma edges. The initial dimensions of the plasma are of the order of mm in the transverse direction whereas in the perpendicular direction they are less than 1  $\mu\text{m}$ . Equation. (3.10) shows that during initial expansion stage, when the velocities are small, the acceleration is very high. With an increase in expansion velocity, acceleration starts to decrease and ultimately becomes zero resulting in an elongated plasma. Since the plasma dimensions are much smaller along the target normal than in the transverse direction, the expansion is transverse in nature.

### (c) Adiabatic plasma expansion

After the termination of the laser pulse, no particles are evaporated or injected into the plasma and the expansion is mostly adiabatic. An adiabatic expansion of the plasma occurs where the temperature can be related to the dimensions of the plasma by the adiabatic thermodynamic equation given by,

$$T[X(t)Y(t)Z(t)]^{\gamma-1} = \text{const.} \quad (3.11)$$

where  $\gamma$  is the ratio of the specific heat capacities at constant pressure and volume. The thermal energy rapidly gets converted into kinetic energy giving higher expansion velocity of the plasma. It has been found for spherical plasmas that the temperature drops off rapidly as the plasma expands; however, drop is smaller at lower temperatures because energy is regained in recombination of the ions. The maximum attainable velocity for any gas in vacuum is given by  $2a/\gamma-1$ , where  $a$  is the velocity of sound [ $a=(\gamma RT/M)^{0.5}$ ] and  $M$  is the Mach number. Thus the maximum attainable velocity is about 3-10 times the velocity of the sound, depending upon the value of  $\gamma$ .

In the adiabatic expansion regime, the velocity of the plasma increases due to a decrease in thermal energy of the plasma. As there is no ejection of particles in the inner edge of the plasma, the density and pressure can be expressed as:

$$n(x, y, z, t) = \frac{N_T}{2^{0.5} \pi^{1.5} X(t)Y(t)Z(t)} \times \exp\left[-\frac{x^2}{2X(t)^2} - \frac{y^2}{2Y(t)^2} - \frac{z^2}{2Z(t)^2}\right] \quad t > \tau, \quad (3.12a)$$

$$P(x, y, z, t) = \frac{N_T}{2^{0.5} \pi^{1.5} X(t)Y(t)Z(t)} \times \exp\left[-\frac{x^2}{2X(t)^2} - \frac{y^2}{2Y(t)^2} - \frac{z^2}{2Z(t)^2}\right] \quad t > \tau, \quad (3.12b)$$

The equations of the gas dynamics which dictate the expansion of the plasma are the same as in the previous regime except that the equation of energy and adiabatic equation of state also need to be solved. The adiabatic equation of state is given by;

$$\frac{1}{P} \left[ \frac{\partial P}{\partial t} + \bar{v} \cdot \nabla P \right] - \frac{\gamma}{n} \left[ \frac{\partial n}{\partial t} + \bar{v} \cdot \nabla n \right] = 0 \quad (3.13)$$

and the equation of temperature is given by

$$\frac{\partial T}{\partial t} + \bar{v} \cdot \nabla T = (1 - \gamma) T \bar{v} \cdot \nabla \quad (3.14)$$

It is assumed that there is no spatial variation in the plasma temperature, or  $\nabla T = 0$ . The solution which controls the expansion of the plasma in this regime is given by

$$X(t) \left[ \frac{d^2 X}{dt^2} \right] = Y(t) \left[ \frac{d^2 Y}{dt^2} \right] = Z(t) \left[ \frac{d^2 Z}{dt^2} \right] = \frac{kT_0}{M} \left[ \frac{X_0 Y_0 Z_0}{X(t)Y(t)Z(t)} \right]^{\gamma-1} \quad t > \tau, \quad (3.15)$$

where  $X_0$ ,  $Y_0$  and  $Z_0$  are the initial orthogonal edges of the plasma after the termination of the laser pulse ( $t \geq \tau$ ). The above equation shows that acceleration of plasma species depends upon the temperature and dimensions of the plasma, and mass of the species. It should be noted that this hydrodynamic model is based on equations of fluid flow, and the expansion velocities are controlled by pressure gradients in the plasma. Thus, this model applies to all species including atoms, ions, molecules, neutrals, small clusters, etc. However, based on the difference in their masses, the expansion velocities may be different for different species.

Several techniques have been used to diagnose the laser produced plasmas. Optical emission spectroscopy is a powerful tool for measuring the temporal and spatial

distribution of ions and neutrals and their relative abundance in the plume [98,99]. Efforts have been made to extract the degree of ionization using Langmuir or ion probes [100]. Time of flight spectroscopy (TOFMS) and time of flight quadrupole mass spectroscopy (TOFQMS) are powerful and flexible analytical methods for identifying ablation species and their kinetic energies. They do not rely on photoemission for detection, in species where internal conversion is efficient and the luminescence yield is low, such as in many clusters. Care must be exercised, however, as ablation plumes contain not only stable neutrals and possibly clusters, but also metastable species such as Rydberg atoms, ionic species, and electrons. In order to differentiate between these species, the experimental configuration must be chosen carefully [101,102].

### 3.2 Pulsed Laser Deposition of Thin Films

In last few years several techniques have been developed like thermal evaporation, r.f. sputtering, chemical vapor deposition, solgel, laser induced chemical vapor deposition and pulsed laser deposition for deposition of thin films. In comparison with other techniques PLD provides several advantages. Several characteristics that distinguish PLD from other techniques are;

1. **Congruent transfer of material:** Films have the same composition as that of the target provided the focused laser energy density is chosen properly. Congruent transfer is a consequence of the high initial rate of heating and highly non-thermal target emission by the laser generated plasma. It gives PLD an edge over the other incongruent transfer techniques such as thermal evaporation or sputtering.
2. **Deposition from energetic plasma beam:** In the ablation plume, atoms and ions have typical initial velocity  $\geq 10^6$  m/sec which for an atom of 100 a.m.u. corresponds to a kinetic energy of  $\geq 52$  eV. The kinetic and internal excitation energies of the ablated species can be used to assist film formation and to promote chemical reactions both in the gas phase and on the growing film surface. Due to very high kinetic energies of the plasma species, high quality films can be grown even at low temperatures.
3. **Capability for reactive deposition in ambient gas:** No electron beam or hot filament is required in deposition chamber so reactive gases can be used.

Energetic species in the ablative plasma react readily with ambient gas molecules to form simple compounds like oxides, nitrides, and hydrides.

4. **Growth of multilayered epitaxial hetero structures:** In these thin film structures adjacent layers share a common, continuous crystal structure. A separate target can be used to grow each layer. Growth is inherently digital because each layer thickness can be precisely controlled by calibrating the deposition rate by counting the pulses incident on the target. By choosing low deposition rate (such as  $0.1 \text{ }^{\circ}\text{A}$  per pulse) it is possible to control film growth near the atomic layer level.
5. **Any material can be deposited:** Any material irrespective of metal, semiconductor and insulator can be grown on any material.

Besides the advantages there are two major disadvantages that limit the commercialization of the process. They are particulate formation and non uniformity of the deposited films. The bulk material in intimate contact with the nascent plasma will suffer a recoil with forces up to  $10^4 \text{ N}$  during the laser irradiation. It has been observed that during the ablation of Al or Ga the 1 cm diameter liquid ball shake with amplitudes estimated at some tenths of a millimeter after each laser shot. The mechanical forces on a target can lead to the ejection of macroscopic particulates generically labeled "laser droplets". The production of laser droplets perhaps represents the greatest obstacle to the use of PLD in commercial applications.

The understanding of the (three dimensional) expansion of the plasma is a prerequisite for the analysis of film thickness profiles in PLD. Experiments have revealed that near the axis of the plasma plume the angular distribution of the flux of species is  $\approx \cos^p \theta$  where  $\theta$  is the angle with normal to the target surface and  $p$  is an integer  $\gg 1$ . This strong forward direction is caused by strong differences in pressure gradients in the axial and radial directions. Therefore, uniform thickness films are produced only in a relatively narrow angular range. The practical solution of this problem is to move the ablation plume relative to the substrate, "painting" the substrate with the plume. For example, the laser beam can be raster-scanned over the target, the substrate can be rotated under an offset plume, or these motions can be combined to obtain uniform thickness deposition. Greer and Tabat [71] showed that laser beam rastering over a large diameter

target can produce uniform, large area films with predictable and reproducible growth rates and properties. For example, oxide ceramic films have been deposited over 150 mm diameter substrates, with variations of only  $\pm 2.3\%$  and  $\pm 0.5\%$  for thickness and composition, respectively.

### 3.3 Deposition of ZnO films

Details of the experiment lay out for deposition of films and characterization tools have been presented in Chapter 2. To summarize ZnO thin films were deposited using a frequency tripled Nd:YAG laser ( $\lambda = 355$  nm) at pulsed repetition rate of 10 Hz and pulse width of 5 ns (full width at half maximum, FWHM). ZnO targets were made from zinc oxide powder (purity 99.99 %) by cold pressing and sintering at 1000 °C for 5 h. Thin films were deposited on glass substrate kept at room temperature in an ambient oxygen (purity 99.9 %) pressure varying from  $10^{-2}$  to 1 Torr at a target substrate distance of 4 cm. As grown films were characterized using x-ray diffraction (XRD), atomic force microscopy (AFM) (Nanoscope III, Digital Instruments), Rutherford back scattering (RBS) and photoluminescence (PL) techniques.

### 3.4 Results and Discussion

The structural characteristics of as deposited films were studied prior to looking for laser action in them. XRD of the films, using  $\text{CuK}\alpha$  ( $1.5418 \text{ \AA}$ ) source, grown at pressures less than  $3 \times 10^{-1}$  Torr showed the films to be highly oriented along (002) plane, implying c-axis of the film uniformly perpendicular to the surface. At pressures greater than or equal to  $3 \times 10^{-1}$  Torr, the planes (101), (002), (100) were observed. Figure 3.2 shows XRD of ZnO films grown at various pressures of oxygen. Figure 3.3 shows variation of width of diffraction peaks (FWHM) corresponding to (002) plane. The broadened diffraction peaks (FWHM) with decreasing pressure imply that the particle size decreases at lower ambient pressures. The average diameter  $b$  of nanocrystallites is estimated using the broadening of the diffraction peaks in the Scherer's formula, chapter 2. Size of nanocrystallites varies from 7 to 16 nm (with an error of less than 20 %). The substrate temperature, ambient gas pressure, and target substrate distance, in addition to laser parameters are the factors that control the width of the diffraction peaks and hence the size of the nanocrystallites. It is expected that at higher pressures, the compressed plasma plume will lead to nucleation of larger ZnO clusters

[103]. The result can be understood by considering the (Zn,O) plume size, the reactive oxygen density, the density of particulates generated at the target that reach the substrate, the surface mobility. Oxygen ambient molecules can be transformed into reactive elements through inelastic collisions within the initial (Zn,O) plasma that is created from the ZnO target by the focused laser beam. ZnO films regardless of the growth technique posses some oxygen vacancies.

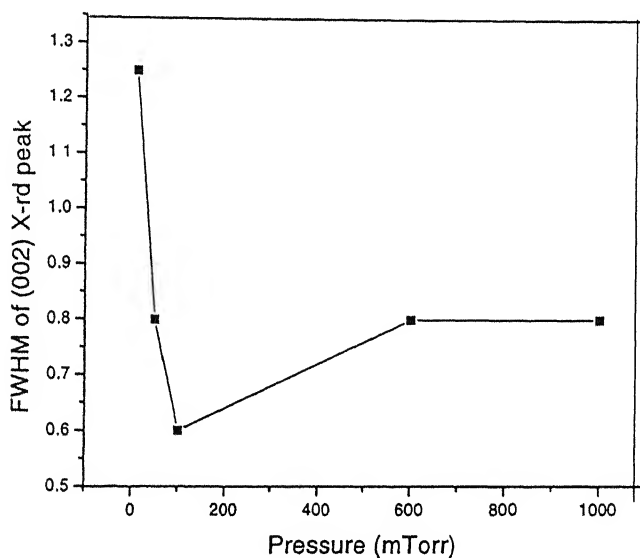
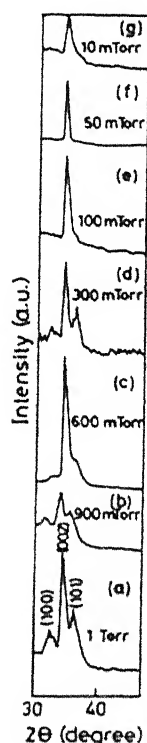


Figure 3-3: Variation of FWHM of the diffraction peak corresponding to the (0 0 2) plane

Figure 3- 2: XRD spectra of ZnO films deposited under various oxygen pressure at RT

So, it is very important for ZnO film growth that the amount of available reactive oxygen created from the ambient oxygen be sufficient to help in the reduction of number of oxygen vacancies. It is also known that the number of particulates arriving at the substrate is decreased as the ambient gas pressure increases. Deposited particulates in the film degrade the film quality. For this reason generally the film quality is improved with the increase of the ambient gas pressure. At sufficiently high pressure, however, the plasma will not reach the substrate and the ZnO film will not be crystallized. The plasma density reaching the substrate might be expected to have a Beer's law behavior given by  $n=n_0\exp(-P\sigma x)$  where  $n_0$ ,  $P$ ,  $\sigma$  and  $x$  are the initial plasma density at the target, the



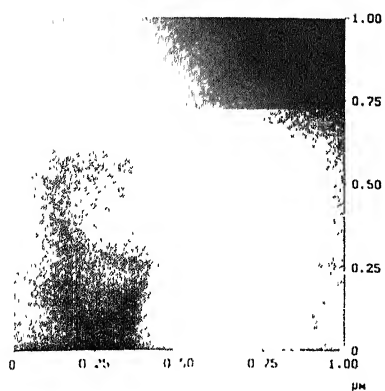
ambient gas pressure, the total cross section for plasma to oxygen collisions, and the distance from the target, respectively. The density of available source elements for ZnO film growth decrease exponentially as the ambient gas pressure increases, and hence the relative density ratio for the Zn and O elements may not be good for high quality film growth at a high ambient gas pressure. The plume size ( $R_p$ ) is related to the ambient gas pressure and to the laser pulse energy ( $E$ ). It can be roughly calculated from the relation  $R_p \propto (E/P)^{1/3\gamma}$ , where  $\gamma$  is the ratio of the specific heats of the elements in the plume. If the substrate is located beyond the plume size  $R_p$ , the adhesion coefficient of the source elements that arrive at the substrate is drastically decreased. Therefore, the crystal quality of ZnO becomes worse as the ambient gas pressure is increased beyond an optimal pressure..

Surface morphologies of the films were studied using AFM. Measurements were done in air. Film samples were scanned over areas ranging from  $500 \times 500 \text{ nm}^2$  to  $10 \times 10 \text{ }\mu\text{m}^2$  at several different locations on the film surface. Figure 3.4 and 3.5 show 2-D and 3-D AFM pictures of as grown films at different pressures of oxygen at RT. Surface morphology varied among films grown at various different ambient pressures. The films grown at lower oxygen pressures were smoother than those grown at higher pressures. At pressures greater than  $3 \times 10^{-2}$  Torr the film became powdery with observable clustering of grains. The average roughness varied from 20 to 108 nm within the scanned area of  $1 \times 1 \text{ }\mu\text{m}^2$  in the pressure range studied. The root mean square (r. m. s.) value of the grain size ranged from 20 to 200 nm. Figure 3.6 and 3.7 show the variation of roughness and grain size (r. m. s.) with the ambient pressure. As is obvious from AFM pictures, clusters are formed at a pressure of 1 Torr. However, the films deposited at 100 mTorr show a particular orientation direction, in confirmation with XRD observation

When the ZnO is ablated by the laser, energetic neutral Zn gas phase is formed and some amount of the Zn reacts with oxygen before the Zn atom arrives at the substrate. It can be expressed as

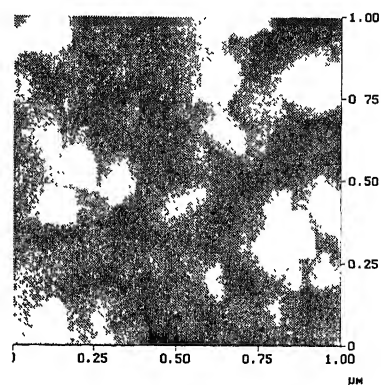


$$\begin{aligned} \Delta G_{[1]}^0 &= -RT \ln (P_{\text{ZnO}}/P_{\text{Zn}} P_{\text{O}_2}^{1/2}) \\ &= -6421 + 9.8T (\text{cal/mol}) \end{aligned} \quad (3.17)$$



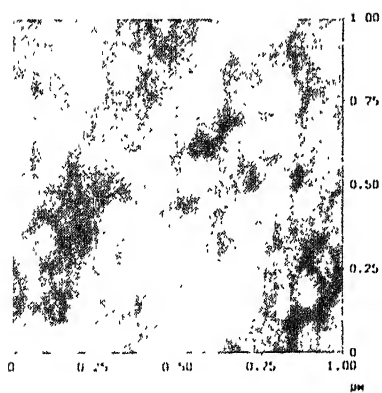
znoltorr.003

1 Torr



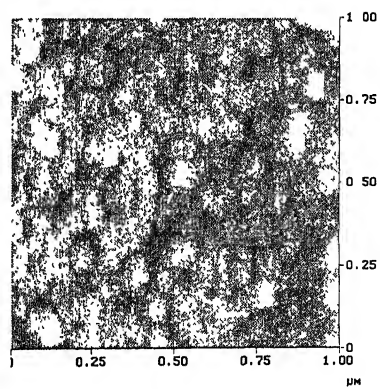
zno3e-1.010

300 mTorr



znole-1.018

100 mTorr



zno5e-1.003

50 mTorr

Figure 3- 2: 2-D AFM photographs of ZnO films deposited under different oxygen pressures

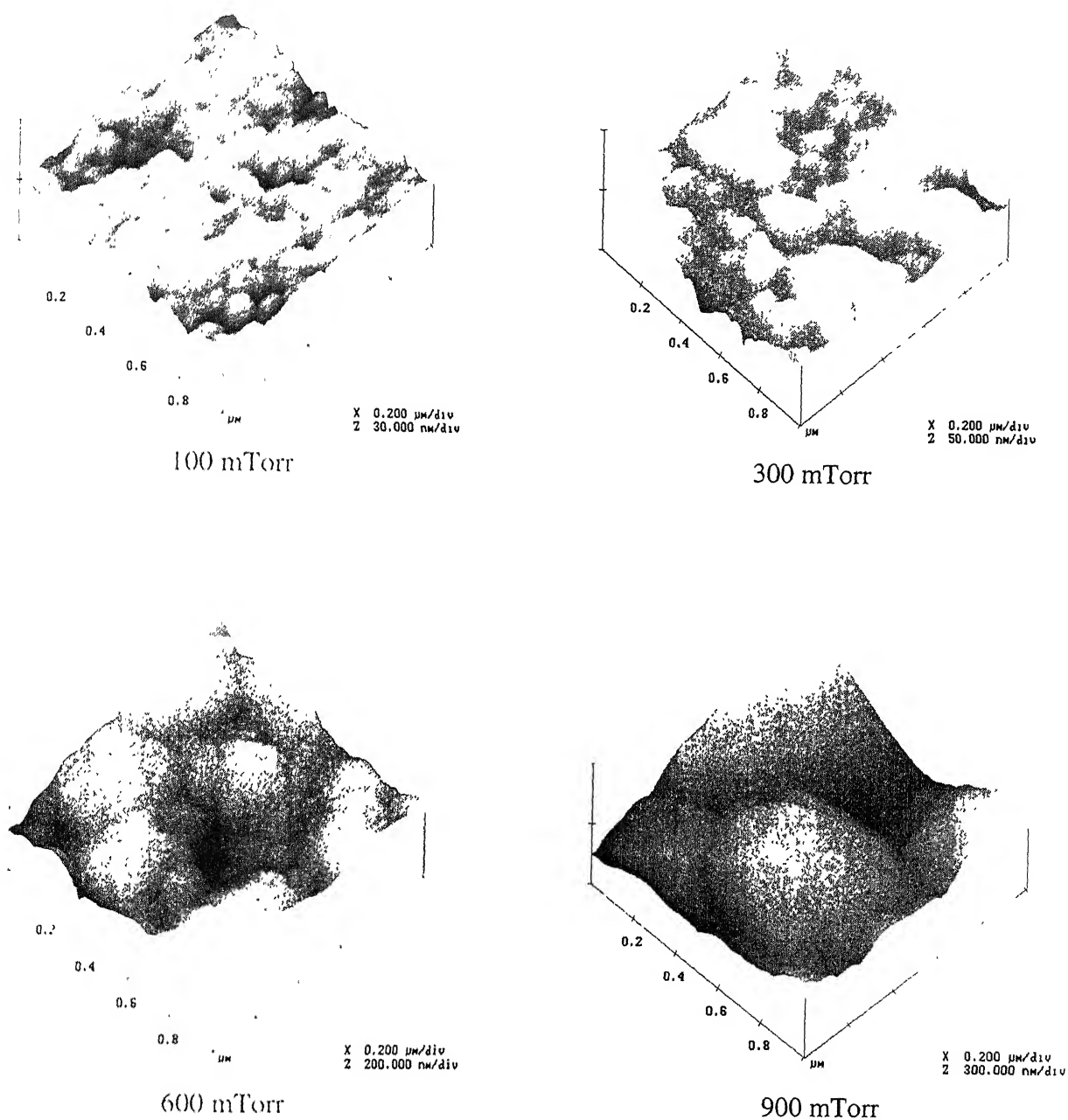


Figure 3- 3: 3-D AFM photographs of ZnO films deposited under different oxygen pressures at RT

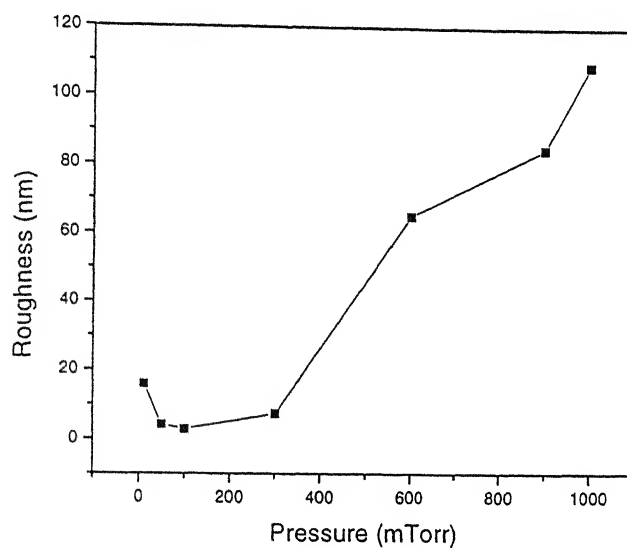


Figure 3- 6: Variation of the surface roughness of the ZnO films deposited under different ambient oxygen pressure

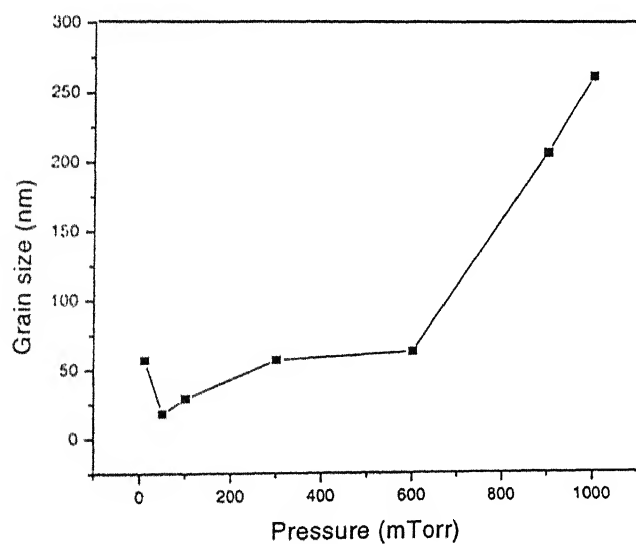
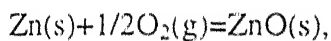


Figure 3- 7: Variation of the grain size of the ZnO films with ambient oxygen pressure

where  $g$  and  $P$  denote the gas phase and partial pressure,  $\Delta G^0_{[1]}$  the change in Gibb's free energy,  $R$  the real gas constant and  $T$  is the temperature. As the reaction temperature increases and the oxygen or Zn partial pressure decreases, the ZnO gas phase formed by reaction given by equation (3.16) tends to be thermodynamically unstable and thus tries to decompose into Zn and  $O_2$  mixture. Although the partial pressure of Zn cannot be measured, higher Zn partial pressure in the vicinity of ZnO target is expected than that near the substrate since a fixed amount of Zn gas atoms are being generated from the ZnO target. Although full reaction equilibrium would not be reached during the deposition process, the critical oxygen partial pressure for the thermal stability of the ZnO gas phase exists at a given substrate temperature (RT in our case) and Zn partial pressure.

At lower oxygen pressure than the critical pressure, a large portion of the ZnO gas phase may decompose into Zn and  $O_2$  gas phase by the reverse reaction, equation (3.16). Therefore, the nucleation of the metallic Zn phase on the substrate can be dominant at lower oxygen partial gas pressures. The metallic Zn nuclei are then oxidized as shown in the following reaction;



$$\Delta G^0_{[2]} = -RT \ln (1/P_{O_2}^{1/2}) = -84275 + 25.3T (\text{cal/mol}) \quad [104]. \quad (3.18)$$

where  $s$  is the solid phase. Since the oxygen partial pressure equilibrates with metallic Zn nuclei at  $\sim 2 \times 10^{-44}$  atm which is significantly lower than those applied in this study ( $P_{O_2} = 1\text{--}500$  mTorr), the deposited metallic Zn nuclei take the oxidation process to form ZnO grains on the substrate. The oxidation rate is relatively low in the applied pressure range [105]. Therefore the ZnO grain growth rate is retarded and fine ZnO grain structure forms at low oxygen partial pressures. As the oxygen partial pressure increases, the oxidation rate increases, leading to large ZnO grains as shown in XRD and AFM.

The photoluminescence spectra of ZnO usually show three PL peaks; green emission around 510 nm, red emission around 650 nm due to defect related deep level emissions, and UV near band edge emission that strongly depends upon the growth conditions of the film [106]. In most polycrystalline thin films, defect related deep level emissions dominate the PL spectra, which precludes various applications such as UV luminescent devices. The photoluminescence spectra of the films deposited at various

pressures of oxygen at RT are shown in Figure 3.8. A strong PL peak at 395 nm decreases with the increase in pressure. This may be due to unfavorable Zn:O ratio at higher pressures of oxygen. Figure 3.9 shows the variation of width (FWHM) of PL peak

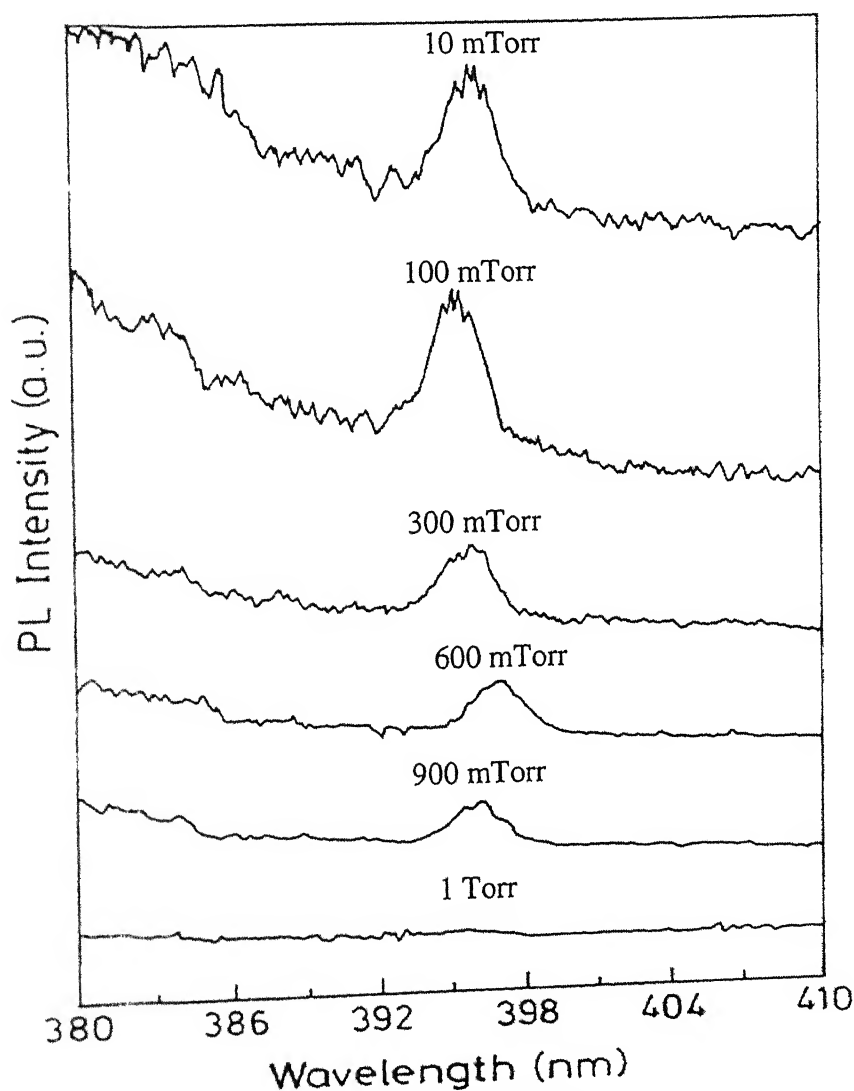
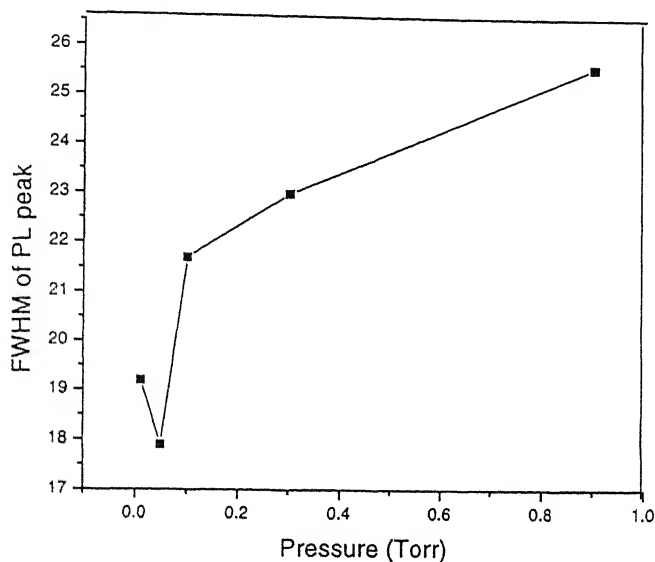


Figure 3- 8: PL spectra of ZnO films grown at various oxygen pressures

with ambient oxygen pressure. The observation of single narrow peak and no deep level emission indicates that our films are defect free pure ZnO films.



**Figure 3- 9: Variation of FWHM of PL with ambient pressure of oxygen**

RBS studies showed that the stoichiometry of the films changes from 1:1 for ZnO at  $10^{-2}$  to 1:2.5 at higher pressures of the ambient gas. Figure 3.10 shows the RBS spectrum of ZnO films deposited under different ambient oxygen pressures. Figure 3.11 shows the thickness of ZnO as measured by RBS deposited under different ambient oxygen pressures. It is observed that thickness of the films increases with the increasing ambient pressure of oxygen. This is due to the higher oxidation rate of Zn leading to the formation of more ZnO clusters and so also the thickness of the films.

With a wurtzite structure ZnO belongs to the  $C_{6v}$  symmetry group. The group theory predicts two  $A_1$ , two  $E_1$ , two  $E_2$  and two  $B_1$  modes. Among them, two  $B_1$  modes are not Raman active. The observed phonon frequencies in the Raman spectra of ZnO are:  $E_2(\text{high})=437 \text{ cm}^{-1}$ ,  $E_2(\text{low})=101 \text{ cm}^{-1}$ ,  $A_1(\text{TO})=380 \text{ cm}^{-1}$ ,  $A_1(\text{LO})=574 \text{ cm}^{-1}$ ,  $E_1(\text{TO})=407 \text{ cm}^{-1}$  and  $E_1(\text{LO})=583 \text{ cm}^{-1}$ , respectively. For the incident light exactly normal to the surface of ZnO samples, only  $A_1(\text{LO})=574 \text{ cm}^{-1}$  and  $E_2(\text{high})=437 \text{ cm}^{-1}$  modes are observed, and the other modes are forbidden according to the Raman selection rules [107,108]. We observed  $A_1(\text{LO})=574 \text{ cm}^{-1}$  and  $E_2(\text{high})=437 \text{ cm}^{-1}$  modes for ZnO pellet as well as thin films as shown in the figure 3.12.

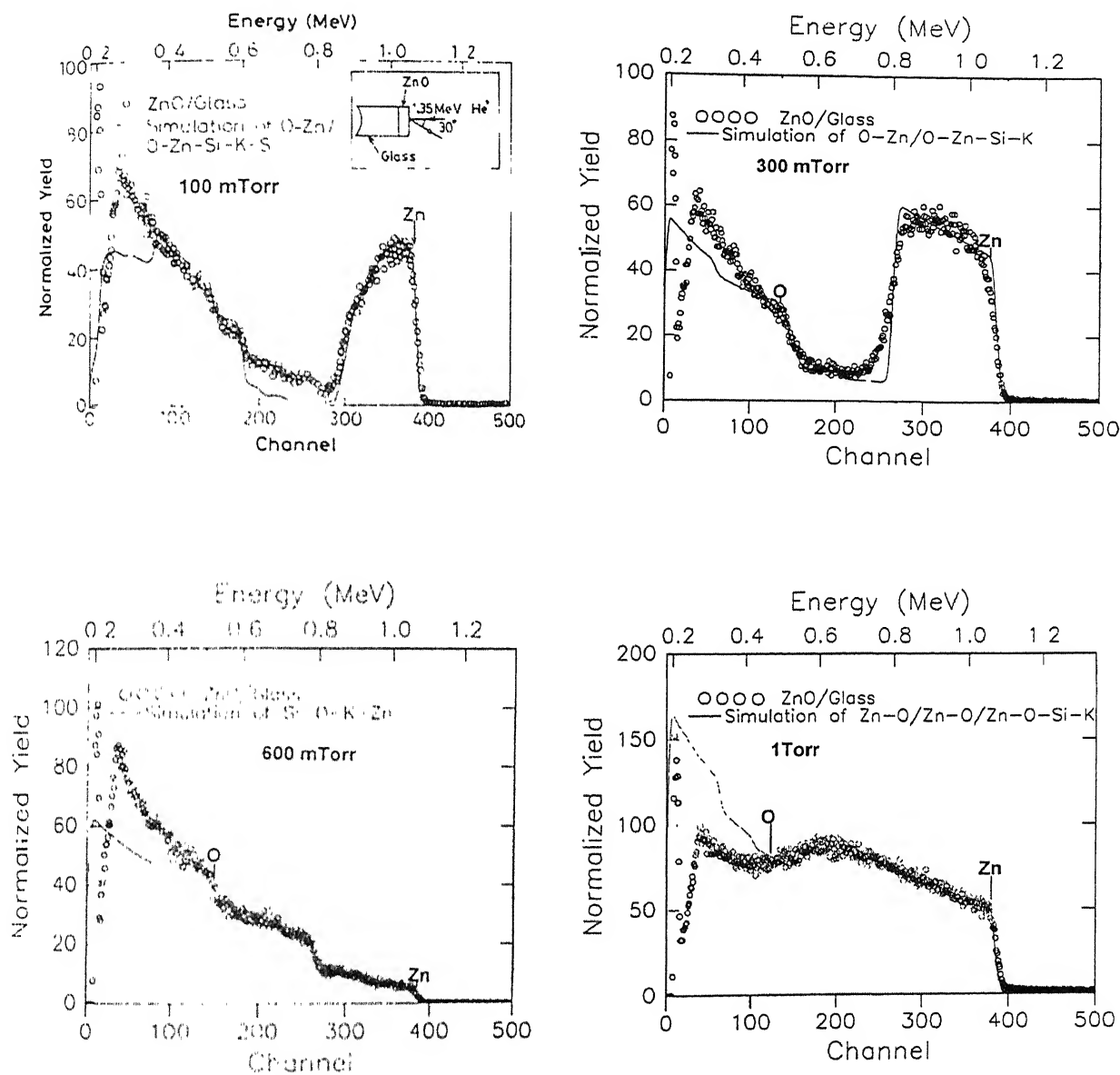


Figure 3- 10: RBS spectrum of PLD ZnO thin films deposited under various ambient oxygen pressures.



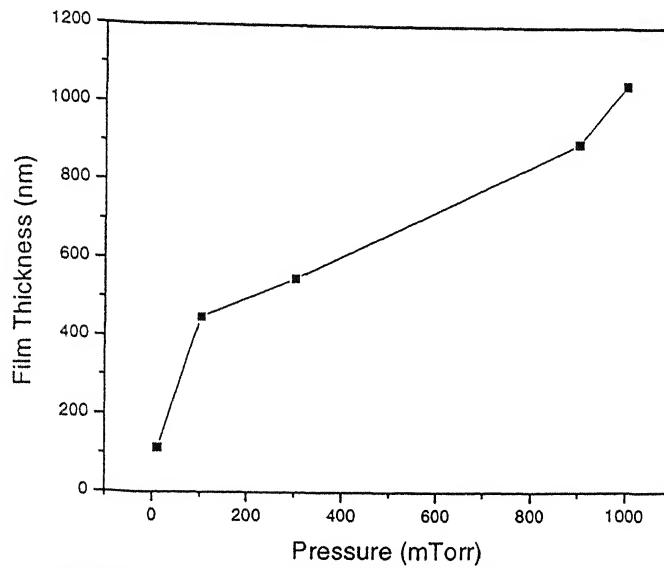


Figure 3- 11: Variation of ZnO film thickness as measured by RBS deposited under different ambient oxygen pressures

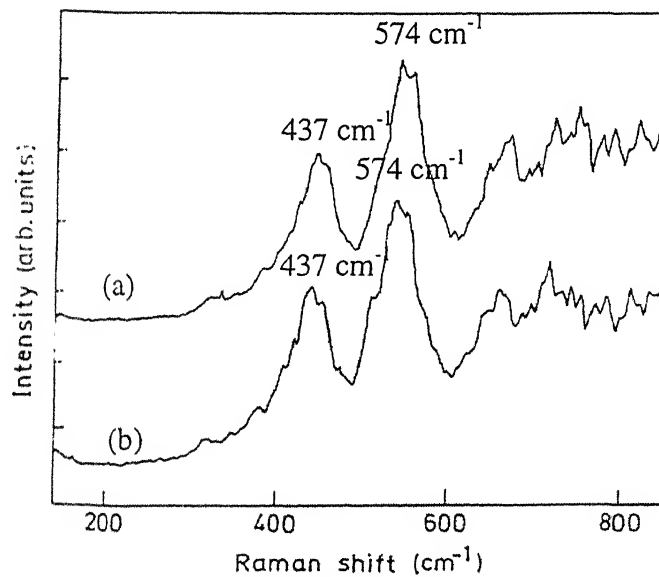


Figure 3- 12: Raman spectra of (a) ZnO pellet and (b) PLD ZnO film

### 3.5 Conclusions

In conclusion we have deposited ZnO films at RT under different pressures of ambient oxygen using PLD. The films deposited at different pressures have different size of nanocrystallites ranging from 7 to 16 nm. The average roughness varied from 20 to 108 nm and grain size from 20 to 200 nm in the pressure range studied. PL depends on the stoichiometry and microstructure of the films.

## Chapter 4

### Random Lasing Action in ZnO

---

Letokhov in 1968 predicted amplification of light due to multiple scattering in random medium [109]. He calculated the optical properties of a random medium with negative resonance absorption that both amplifies and scatters light. Thus taming the evil nature light in disordered system into order. Nonetheless, it took 25 years to show experimentally the amplification of light. In 1993 Gouedard et al. [110] attempted to optically excite grinded powder laser crystal. They observed sub nanosecond and narrow bandwidth pulses when the active medium of neodymium compounds were pumped at high intensity. This emission was spatially incoherent as shown by a speckle statistics analysis. However, it is extremely difficult to optically excite a random material because most of the excitation light is simply scattered back and very little is absorbed by the laser material. Thus to observe any detectable effect very high pulse energies that lie close to the normal thermal threshold of the material are needed. Not only this material must also be able to stand large energy i.e; a large damage threshold. Wiersma et al. [111] found that powdered titanium doped sapphire can withstand these large intensities. The crystal was grounded to very small particles ( $\approx 10 \mu\text{m}$ ) and excited with strong light pulses from a frequency doubled Nd:YAG laser. The amplification was measured with a low intensity “probe” laser immediately after the excitation pulse. Lawandy et al. [112] observed that addition of scatterers like  $\text{TiO}_2$  or polystyrenes, which have very high refractive index to a clear homogenous solution of Rh 6G laser dye dramatically narrows the spectral width of the emission spectra. The spectral narrowing was observed above a well-defined threshold of the pump laser intensity. Although this is also a natural phenomenon in the case of Amplified Spontaneous Emission (ASE), the main difference of it with ASE is that it has spectral width almost two order magnitude smaller than that of ASE and appearance of discrete lasing modes which are missing in case of ASE [113-115]. The mechanism of formation of laser cavities in such a random gain medium is different from that of a conventional laser. The strong and recurring scattering in a

random gain medium helps in forming closed-loop feedback paths leading to lasing. The system is termed as a random laser [116,117].

To understand the random laser let us first consider what happens to light when it passes through the random scattering media without gain. When light passes through air consisting of dust particles or through a colloidal solution it undergoes scattering. Scattering is a completely random phenomenon. If a laser beam passes through the scattering medium, scattering generally destroys the phase relation and so also the coherent nature of laser light. On a gross macroscopic level the explanation is simple, the incoming beam is attenuated due to scattering and a diffuse glow emanates from the medium. On the microscopic level, however, the situation is extremely complex. There are two scattering regimes. One, the single scattering regime, when the scatterer are weakly scattering and the density of scatterer is small so that the probability of light that is scattered once to be scattered again by other scatterer is extremely small. Another is the multiple scattering regime. For a large number of particles in the sample or at larger sample dimension, one can expect light to scatter more than once, multiple scattering, before leaving the scattering volume. This can also be achieved by increasing the refractive index contrast between the scattering particles and the suspended liquid. Interference effects are scrambled due to the many random scattering events and light is assumed to propagate diffusively. In other words we can describe the propagation of light by the diffusion equation for particles in a medium,

$$\frac{\partial n(\vec{r}, t)}{\partial t} = D \nabla^2 n(\vec{r}, t) \quad (4.1),$$

where  $n(\vec{r}, t)$  is the particle density at a point  $\vec{r}$  in space and at a time  $t$ .  $D$  is the diffusion constant. The above equation is also commonly known as the heat equation. This equation holds when there is no dissipation or generation of light in the sample, because only then the situation can be analogous to particle diffusion. In this multiple scattering regime, the scattering is very strong perturbation on the incident light field and the field amplitude is strongly modified by the presence of other scatterers. It is the multiple scattering domain where most of the random laser experiments have been performed. The scattering of light in some way with a particle is expressed by the cross-section,  $\sigma_s(\omega)$ , for the relevant type of interaction. The cross section ( $\sigma_s$ ) usually depends on the

frequency of the light  $\omega(=2\pi\nu)$ . The total chance of interaction depends on the density  $n$  of particles in the medium. Thus the mean free path is given by

$$l_s = \frac{1}{n\sigma_s} \quad (4.2).$$

The mean free path is a measure of the average distance between two events, for example in the case of scattering. It can also be taken as characteristic distance scale at which the relevant quantity produces its effect for example in the case of absorption where the inelastic mean free path gives the distance light has to travel before its intensity reduces to  $1/e$  of its initial value.

In general depending upon the length scale of scattering mean free path the following regimes can be defined,

**(a) Weak and modest scattering with gain**

In this regime the mean free path is of the order of the sample size, the role of the scatterers is trivial. If we pump a clear laser crystal of certain geometry, ASE will develop in the direction of largest gain generally the direction in which the excited region is most extended. This yields directionality in the output of the system. Due to gain narrowing the spectrum of ASE can be very narrow as in the output of laser. Also, the pulse length of the ASE can be very much shorter than the lifetime of the excited state of the laser material. However, the addition of scatterers to the clear laser material scrambles the directionality of the ASE, the output will be in all directions, spectrally narrow but will decay rapidly. Thus the only role of the particles in regime of weak scattering is to scramble the directionality of the ASE, which would build up also in the absence of scatterers. The effect has been observed in weakly scattering dye solutions [112].

If the scattering strength increases, i.e. the mean free path becomes much smaller than the sample size but still larger than the wavelength, the presence of scatterers influences the spectral and temporal properties of the output. Due to scattering the residence life of the light in the sample is increased compared to a clear sample without scatterers. A gain narrowing process will therefore, be much more efficient. In other words the increase of scatterers makes output spectrum narrower.

### (b) Strong scattering with gain

On further increase of the scattering strength a situation is reached where mean free path becomes equal to or smaller than the wavelength. This is the regime where Anderson localization is expected to occur [118]. Due to very strong scattering, recurrent scattering events arise. These are scattering events in which the light returns to its scatterer from which it was scattered, thereby forms closed loop paths. Thus if the amplification along such a loop path is strong enough it could serve as random ring cavity for the light. The system would lase in the modes allowed by the ring cavities. Interference between the two counter propagating beams in a disordered structure gives rise to the enhanced back scattering, called coherent backscattering or weak localization [83-85] which has been described in chapter 2. Coherent backscattering is an interference effect that manifests itself as doubling of the scattered intensity in the exact back-scattering direction compared with other directions.

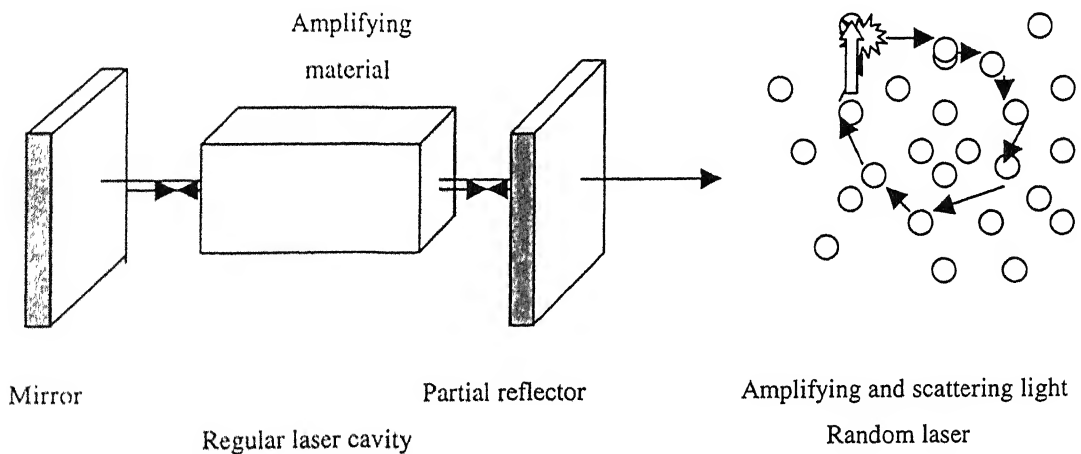


**Figure 4- 1: Regular laser cavity and Random Laser**

The main difficulty to realize Anderson localization or Random laser is the simultaneous realization of strong scattering as well as gain. Anderson localization is a common phenomenon in the disordered system. Since the Anderson localization is completely based on the interference effect, and interference being a common property of all wave phenomena, one can extend this phenomenon to photon localization in

disordered dielectric media. Recently Anderson localization of photon has been observed in GaAs powder [118]. Apart from similarities there are certain dissimilarities between electron transport and photon transport in disordered media. For example, the number of electrons is always conserved while the number of photons is not in an amplifying (or absorbing) random medium. A phenomenon that never occurs in an electronic system is the laser action that occurs in a disordered gain medium. Figure 4.1 shows pictorially a recurring scattering event that could provide coherent feedback leading to lasing action. The parameter that describes the scattering length is the scattering mean free path scaled by the wavelength  $\lambda$  of light,

$$kl_s \equiv \frac{2\pi l_s}{\lambda} \quad (4.3),$$

The transition to the localized regime occurs when

$$kl_s \leq 1$$

where  $k$  is the propagation vector and  $l_s$  is the scattering mean free path. This is known as Ioffe-Regel criterion [118]. The criterion states that localization occurs if the scattering mean free path becomes comparable to the effective wavelength so that a freely propagating wave cannot even perform one oscillation before it gets scattered again.

In a recent experiment Cao et al. have reported the lasing action in ZnO and GaN powder due to the Anderson Localization of light [47-48]. As is said earlier the recurrent scattering could provide coherent feedback. If the amplification along such a loop path exceeds the loss, laser oscillations could occur in the loop. Thus the loop serves as a laser resonator. As in a conventional laser the requirement of the phase shift along the loop being equal to multiple of  $2\pi$  determines the oscillation frequencies. Such a laser is called "Random Laser". It represents a coherent effect in active random medium.

In this chapter the random laser action observed in bulk ZnO pellet as well as in ZnO thin film is presented. The laser action was observed in UV region of the spectrum on optically pumping the samples.

#### 4.1. Experimental details:

The details of the experimental technique used to observe lasing have been discussed in Chapter 2. In brief, ZnO pellet was made from zinc oxide powder (99.99% pure) cold pressed under a pressure of 6 tons for 20 min and then sintered at  $1000^\circ\text{C}$  for 5

h. Methanol was used as a binder for making the pellet. The sample was optically pumped with a frequency tripled Q-switched Nd:YAG laser ( $0.355\text{ }\mu\text{m}$  at 10 Hz repetition rate, 5 nsec pulse width (FWHM)). The pump beam was focused on the sample surface, and the lasing emission from the sample was observed through an optical fiber coupled to the monochromator (Jobin Yvon HRS-2).

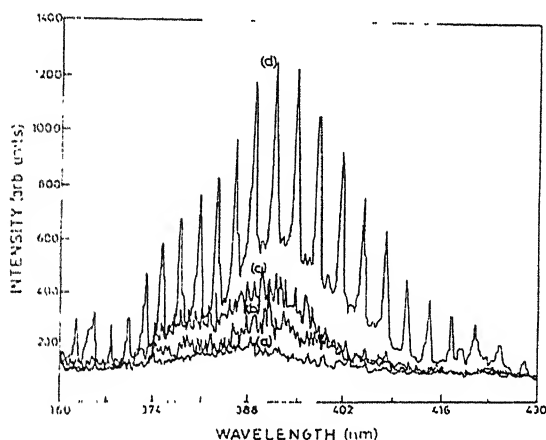


Figure 4- 2: Emission spectra at different excitation intensity (a)  $1527\text{ kW/cm}^2$  (b)  $2860\text{ kW/cm}^2$  (c)  $3310\text{ kW/cm}^2$  and (d)  $7890\text{ kW/cm}^2$

## 4.2. Results and discussion

### 4.2.1 Laser action in ZnO pellets

Figure 4.2 shows the evolution of the emission spectra with the increasing excitation laser intensity. Figure 4.3 shows the peak intensity as a function of the

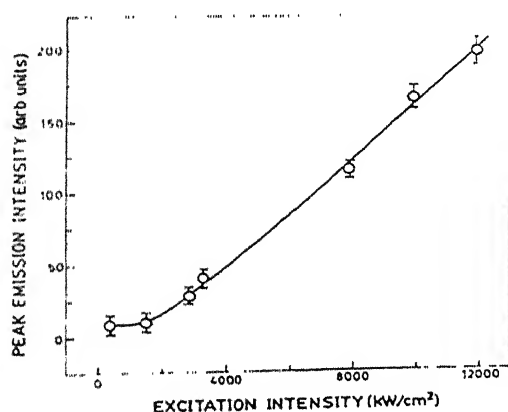
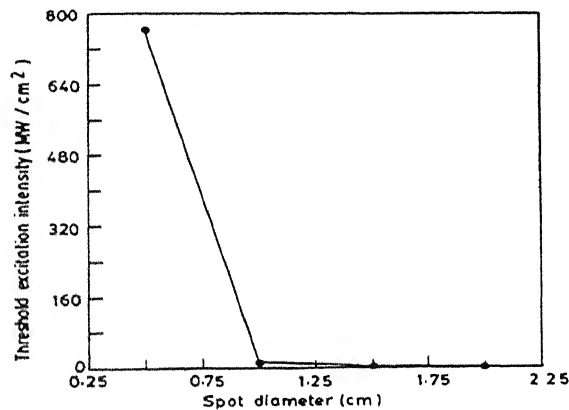


Figure 4- 3: Variation of peak emission intensity as a function of excitation intensity



excitation intensity. A steep rise in the output after the input pump intensity exceeds  $1500 \text{ kW/cm}^2$  can be taken as the lasing threshold. Below the threshold excitation intensity, the spectrum observed is a single broad spontaneous emission peak, figure 4.2. As the input intensity increases, the emission became narrower due to preferential amplification at frequencies close to the maximum of the gain spectrum. At excitation intensity above threshold, very narrow peaks are observed in the emission spectrum. The line width of these peaks decreased to less than  $0.6 \text{ nm}$ , which is more than 25 times smaller than the line width of ASE below threshold. The dependence of laser action on excitation volume and excitation intensity was studied by varying the excitation area. Figure 4.4 shows the variation of lasing threshold excitation intensity with the focused spot. Figure 4.5 shows



**Figure 4- 4: Variation of threshold excitation intensity with diameter of the focused spot**

the variation of the FWHM of the observed mode with the excitation pump intensity. The FWHM decreases as the pump intensity increases above threshold. It is clear from figure 4.4 that the threshold pump intensity depends on the excitation area. As the excitation area increases, the lasing threshold pump intensity decreases and more lasing peaks are observed in the emission spectra. However, the laser oscillations stopped once the excitation area decreased below a critical area [119]. The increase of the threshold for small excitation regions is attributed to longer path inside the pumped volume that has gain resulting in amplification. Even if a scattered path reaches the passive (unexcited) part of the system, there is a large probability that it will return to the amplifying region because of the large pumped area. For a small excitation beam diameter the light paths

will very probably leave the amplifying region, with a small chance of returning. Thus to compensate for losses one needs to put in more energy, i.e. the threshold goes up.

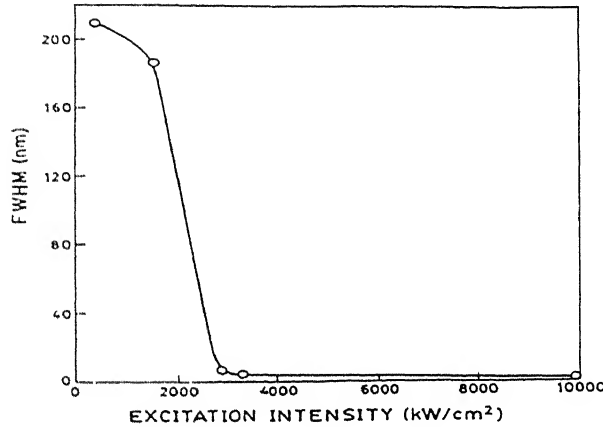


Figure 4- 5: Variation of the spectral width (FWHM) of the observed modes with the excitation intensity.

Figure 4.3 shows a clear evidence of stimulated emission above a threshold of citation intensity of 1500 kW/cm<sup>2</sup>. However, to ensure lasing, it is necessary to see evidence of longitudinal modes or demonstrate coherence. Mode spacing for cavity of length  $d_m$  is given by [120-122],

$$\nu = \frac{c}{2n(\nu)d_m} q \quad (4.4)$$

$$\text{and} \quad \nu + \Delta\nu = \frac{c}{2n(\nu + \Delta\nu)d_m} (q + 1) \quad (4.5)$$

we write,

$$n(\nu + \Delta\nu) = n(\nu) + (dn/d\nu)\Delta\nu \quad (4.6)$$

have

$$(\nu + \Delta\nu)[n + (dn/d\nu)\Delta\nu] = (c/2d_m)(q + 1) \quad (4.7)$$

$$\Delta\lambda = \frac{\lambda^2_0}{2d_m(n - \lambda_0 \frac{dn}{d\lambda})} \quad (4.8)$$

where  $n(E)$  is the refractive index at  $\lambda_0$  ( the wavelength of one of the modes ), and  $dn/d\lambda$  is the dispersion. In terms of energy equation (4.8) can be written as,

$$\Delta E = \frac{\pi c h / d_m}{n(E) + E \frac{dn}{dE}} \quad (4.9)$$

where  $\Delta E$  is the energy spacing between the cavity modes and  $n(E)$  the refractive index of the material at  $E$ . Equation (4.9) gives  $d_m = 7 \mu\text{m}$ .

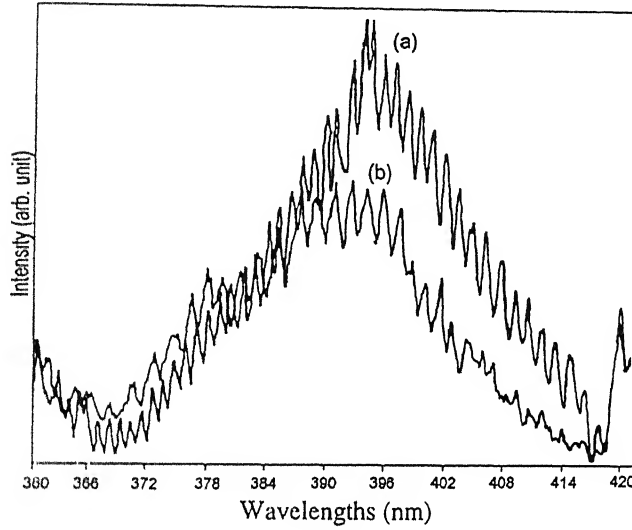


Figure 4- 6: Emission spectrum for two different excitation lengths (a)  $l_g = 2 \text{ mm}$  (b)  $l_g = 1 \text{ mm}$

The lasing spectrum, figure 4.2 shows how the longitudinal modes of the cavity modulate the emission spectrum as the laser intensity crosses the lasing threshold. The observed spectrum follows from the population distribution. The pump photons are absorbed by electrons in the valence band and electrons move to the conduction band. They subsequently relax to the bottom of the conduction band before radiative decay. With completely filled inverted population the optical transitions are emissions rather than absorptions. The photon absorption/amplification constant experiences a sign change as it changes from absorption to emission. The cavity modes are the clear evidence, as is the energy at which the absorption /amplification constant changes its sign.

The optical gain of the laser was measured by measuring the laser output (above threshold) as shown in figure 4.6 for two excitation lengths  $l_g$  and  $l_g'$ . In the region of small signal gain, the amplified output as a function of excitation length  $l_g$  is given by [123-124]

$$I(l_g) = (I_s A / g) [\exp(g l_g) - 1], \quad (4.10)$$

where  $I_s$  is the spontaneous emission intensity,  $A$  is the cross sectional area of excitation region, and  $g$  is the optical gain coefficient. For two excitation lengths, it follows from Equation (4.10),

$$F(g l) = k \log \left[ \frac{f(l'_g)}{f(l_g)} \right] = k \log \frac{\exp(g l'_g) - 1}{\exp(g l_g) - 1} \quad (4.11),$$

where  $k = [\log(l'_g / l_g)]^{-1}$ . We obtained the gain coefficient of  $7.50 \text{ cm}^{-1}$ .

It is worthwhile to check whether the scattering is weak, modest, or strong. To do so we studied coherent backscattering described in chapter 2. The width of the curve 'cone' of backscattered radiation is of the order of  $(k l_s)^{-1}$  where  $l_s$  is the scattering mean free path and  $k = 2\pi/\lambda$ . From the angle of the cone of figure 2.9 we get  $l_s = 0.238 \text{ } \mu\text{m}$  ( $\approx 0.6\lambda$ ). This is the regime where Anderson localization is expected to occur.

The available data conclusively prove that laser action has occurred in the ZnO pellet. The next question to be addressed is the mechanism of formation of laser cavities. A powder is best example of disordered material. It has been demonstrated that in a random gain medium strong and recurrent scattering helps in forming closed-loop feedback paths which result in lasing. In our samples (pellets), average particle size is 20

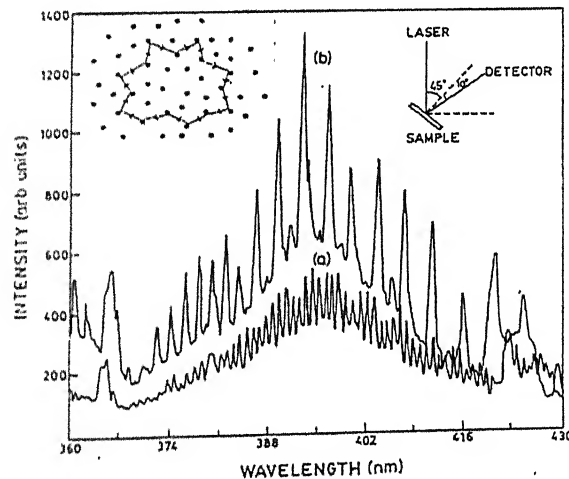


Figure 4- 7: Emission spectra for two observation angles of  $10^\circ$  from the normal to the sample surface, (a) normal to the sample surface (b). The excitation intensity is  $7890 \text{ kW/cm}^2$ . The excitation area is  $3.14 \text{ mm}^2$ . Left side inset shows the formation of ring cavities due to the multiple scattering. Right side inset shows the directions of the laser and detector.

nm, the scattering mean free path is as short as  $0.238 \mu\text{m}$  and hence many closed loops may be formed. These loops could serve as ring cavities having different losses. The laser oscillations are observed when the gain in the medium exceeds the losses. The discrete peaks observed in the emission spectra, figure 4.2, clearly show the laser emission. Unlike a conventional laser, which has well-defined cavity and hence a unique direction of laser emission, laser emission from the powder was observed in all directions. This was confirmed by recording laser emission spectra at various observation angles as shown in figure 4.7. The lasing modes observed at different angles are different. This is due to formation of different laser cavities by multiple scattering and different cavities could have different output direction. It is worthwhile to mention that an earlier report on laser action in active powders of  $\text{TiO}_2$  doped Nd:YAG had a particle size much larger than the emission wavelength [112]. There, every single particle could serve as a resonator. However, in the present case of powder laser resonances are due to recurrent light scattering.

#### 4.2.2 Laser action in PLD ZnO thin films

To observe laser action, films of various thickness were optically pumped by third harmonic of Nd:YAG laser. Figure 4.8 shows the evolution of the emission intensity with the increasing excitation (pump laser) intensity for a film of thickness  $1.5 \mu\text{m}$  deposited at ambient pressure of  $10^{-1}$  Torr. A single broad emission peak is observed below the threshold excitation intensity. A steep increase in the output intensity as the pump laser exceeds an intensity of  $2387 \text{ kW/cm}^2$  is observed as shown in figure 4.9. At excitation above threshold very narrow peaks, almost 10 times narrower than the emission below lasing threshold, are observed in the emission spectrum. The emission spectrum becomes narrower due to preferential amplification at frequencies close to the maximum of the gain spectrum. Due to local variation of particle density and spatial distribution in the film, there exist small regions of higher disorder and stronger scattering and of lower disorder and weaker scattering. Light can be confined in these regions forming closed loop feedback paths through multiple scattering and interference. The gain depends on the volume ( $4/3\pi a^3$ ) of the disordered amplifying medium and loss to its surface area ( $4a^2$ ), where 'a' is radius of sphere of disordered material. Laser oscillations occur once

the optical gain in a cavity exceeds the losses of a cavity. The various peaks observed in the emission spectrum (figure 4.8) are the cavity resonant frequencies.

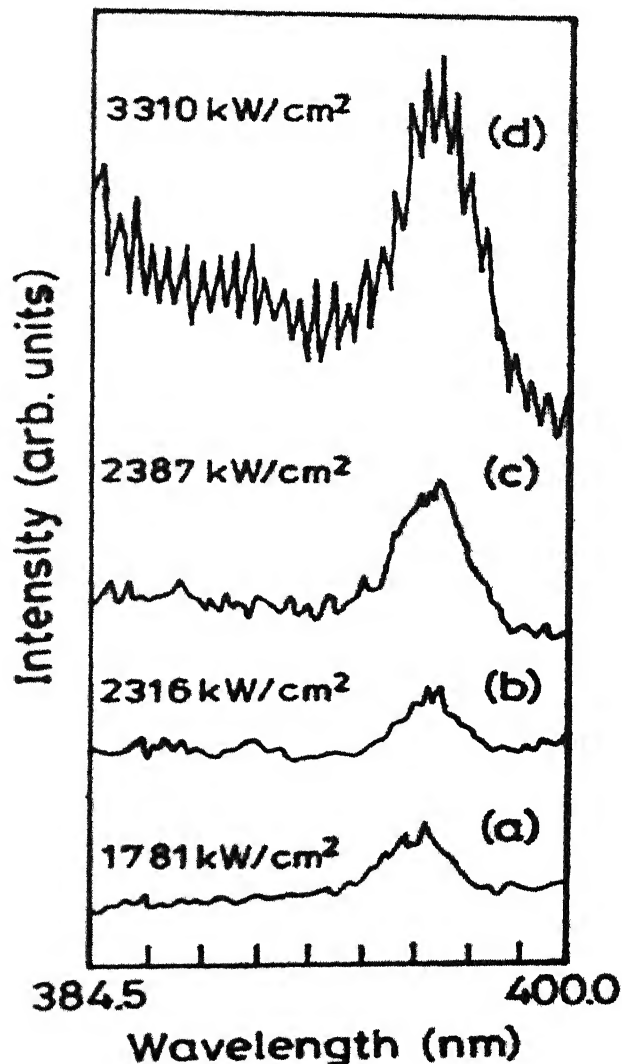


Figure 4- 8: Emission spectra from an optically pumped ZnO film of 1.5  $\mu\text{m}$  thickness deposited at oxygen pressure of  $10^{-1}$  Torr

Increasing thickness of the film can lead to three-dimensional localization of light. To confirm this, ZnO films with thickness of 0.5, 1.0 and 1.5  $\mu\text{m}$  were pumped at an intensity of 2387  $\text{kW}/\text{cm}^2$ . The films were deposited at ambient pressure of  $10^{-1}$  Torr of oxygen. Films deposited at higher pressure did not yield good results due to poor stoichiometry. Figure 4.10 shows the emission spectra from the films. As is obvious from the figure 4.10 the intensity of the laser emission increases with the thickness of the film.

The increased emission is attributed to a longer optical path in thick films contributing to amplification.

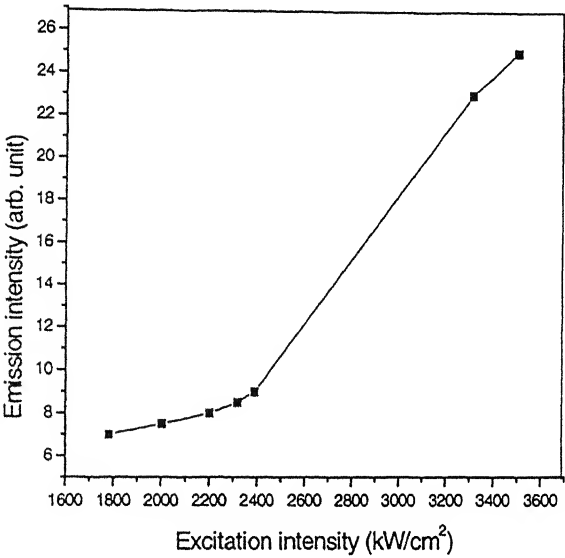


Figure 4- 9: Variation of peak emission intensity with excitation intensity of laser.

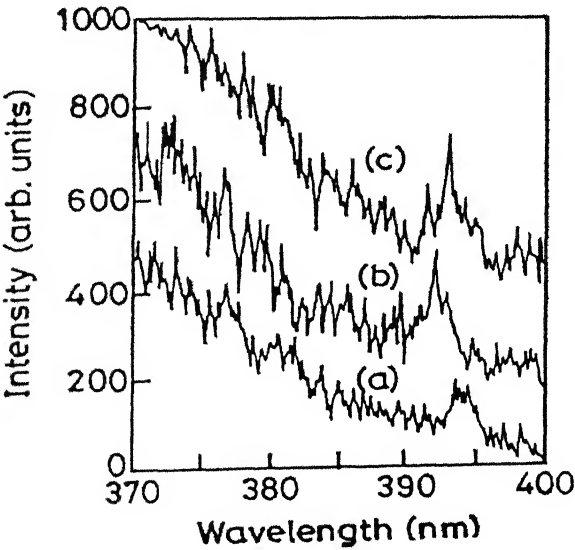


Figure 4- 10: Emission spectra from ZnO film of thickness of (a) 0.5 (b) 1 and (c) 1.5  $\mu\text{m}$ .

### 4.2.3 Theoretical Model:

Earlier prediction of lasing in a random systems by Letokhov were based on time dependent diffusion equation. Using a similar approach Zyuzin [127] analyzed the fluctuation properties of a random system near the lasing threshold. Recently, John and Pang [128] studied the random lasing system by combining the electron number equations of energy levels with the diffusion equation. However, the diffusion approach, does not explain the lasing peaks observed in the recent experiments [48,120] in both semiconductor powders and in organic dyes-doped gel films. An approach based on time-independent wave equations [129-132] for the random gain medium has also been used to determine the lasing threshold. To fully understand the random lasing system, Jiang and Suukoulis [133] used time dependent wave equations in random systems obtained by coupling Maxwell's equation with rate equations of electron population within a semi classical framework. By incorporating the finite difference time domain (FDTD) they calculated the wave propagation in random media with gain. Our experimental observations are qualitatively in agreement with this theoretical model. The system is assumed to consist of many dielectric layers of real dielectric constant of fixed thickness, sandwiched between two surfaces, with the spacing between the dielectric layers filled with the gain medium (e.g. solution of dye molecules). The distance between the neighboring dielectric layers is assumed to be a random variable and the overall length of the system is  $L$ . Essentially, the system is a one-dimensional simplification of the real experiments.

To simulate the experiments the binary layers of the system are assumed of dielectric materials with dielectric constants of  $\epsilon_1=\epsilon_0$  and  $\epsilon_2=4\times\epsilon_0$ , respectively. The thickness of the first layer, which simulates the gain medium, is taken as a random variable  $a_n=a_0(1+W\gamma_r)$  where  $a_0=300$  nm,  $W$  is the strength of randomness., and  $\gamma_r$  is a random value in the range  $(-0.5, 0.5)$ . The thickness of the second layer, which simulates the scatterers, is a constant  $b_r=180$  nm. The layers representing the gain medium, are assumed to be filled with a four level electronic material as shown in figure 4.11. An external pumping pumps the electrons from ground level ( $N_0$ ) to third level ( $N_3$ ) at a pumping speed  $P_r$ , which is proportional to the pumping intensity in the experiments. After  $\tau_{32}$  lifetime electrons can nonradiatively transfer to the second level ( $N_2$ ). The



second level  $N_2$  and first level  $N_1$  are the lasing levels. Electrons can transfer from upper lasing level to lower lasing level through spontaneous or stimulated emissions. Finally, the electrons can non-radiatively transfer from first level ( $N_1$ ) to the ground level ( $N_0$ ). The lifetimes and energies of upper and lower lasing levels are  $\tau_{21}$ ,  $E_2$  and  $\tau_{10}$ ,  $E_1$  respectively. The center frequency of radiation is  $\omega_a = (E_2 - E_1)/\hbar$  which is chosen to be equal to  $2\pi \times 6 \times 10^{14}$  Hz ( $\lambda = 0.5 \mu\text{m}$ ). The parameters  $\tau_{32}$ ,  $\tau_{21}$  and  $\tau_{10}$  are taken as  $10^{-13}$  sec,  $10^{-9}$  sec and  $10^{-11}$  sec, typical values for the laser dyes [134]. The total electron density  $N_0^0 = N_0 + N_1 + N_2 + N_3$  and the pump rate  $P_r$  are the control variables.

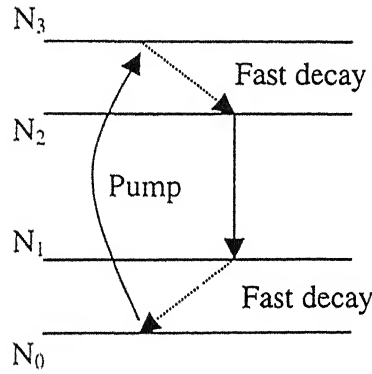


Figure 4- 11: Level diagram of a four level electronic material showing the emission and absorption

The time-dependent Maxwell's equations are given by [135],

$$\nabla \times \vec{E} = -\frac{\partial \vec{B}}{\partial t} \quad (4.13)$$

$$\nabla \times \vec{H} = \epsilon \frac{\partial \vec{E}}{\partial t} + \frac{\partial \vec{P}}{\partial t} \quad (4.14)$$

where,  $\vec{B} = \mu \vec{H}$ , and  $\vec{P}$  is the electric polarization density from which the amplification or gain can be obtained. Following the single electron case, the polarization density  $\vec{P}(x, t)$  in presence of an electric field obeys the following equation [135];

$$\frac{d^2 \vec{P}(t)}{dt^2} + \Delta \omega_a \frac{d\vec{P}(t)}{dt} + \omega_a^2 \vec{P}(t) = \frac{\gamma_r}{\gamma_c} \frac{e^2}{m} \Delta N(t) \vec{E}(t), \quad (4.15)$$

where  $\Delta\omega_a = 1/\tau_{21} + 2/T_2$  is the FWHM of the atomic transition.  $T_2$  is the mean time between de-phasing events which is taken to be  $2.18 \times 10^{-14}$  s,  $\Delta N(x,t) = N_1(x,t) - N_2(x,t)$  and  $\gamma_r = 1/\tau_{21}$  is the real decay rate of the second level., and  $\gamma_c = (e^2/m)(\omega^2/6\pi\epsilon_0 c^3)$  is the classical rate.

The rate equations giving the number of electrons in various levels are;

$$\begin{aligned} \frac{dN_1(x,t)}{dt} &= P_r N_0(x,t) - \frac{N_3(x,t)}{\tau_{32}} \\ \frac{dN_1(x,t)}{dt} &= \frac{N_2(x,t)}{\tau_{21}} + \frac{E(x,t)}{\hbar\omega} \frac{dP(x,t)}{dt} - \frac{N_1(x,t)}{\tau_{10}} \\ \frac{dN_2(x,t)}{dt} &= \frac{N_3(x,t)}{\tau_{32}} + \frac{E(x,t)}{\hbar\omega} \frac{dP(x,t)}{dt} - \frac{N_2(x,t)}{\tau_{21}} \\ \frac{dN_0(x,t)}{dt} &= \frac{N_1(x,t)}{\tau_{10}} - P_r N_0(x,t) \end{aligned} \quad (4.16)$$

where  $\frac{\vec{E}(x,t)}{\hbar\omega_a} \cdot \frac{d\vec{P}(x,t)}{dt}$  is the induced radiation rate or excitation rate depending on its sign.

Finite Difference Time Domain Method (FDTD) is used to solve coupled differential equations (4.13- 4.16). The FDTD model has advantage that one can follow the evolution of both the electric field and electron numbers inside the system. One can clearly distinguish the localized modes from the extended ones. One can also examine the time dependence of electric field inside and just outside the system.

Although the model is strictly applicable to dye solution, the numerical simulations [133] have shown that,

- (a) a well-defined lasing threshold exists which we have also observed in our experiment (figure 4.3) .
- (b) as the pumping excitation intensity  $P_r$  increases above the threshold, lasing modes appear, similar to our experimental results shown in figure 4.2.

### 4.3 Conclusions

To summarize, we demonstrated a random laser in optically pumped ZnO powder.

---

The lasing action is attributed to the coherent feedback due to multiple scattering in the powder. Lasing action has also been observed in ZnO thin films which were deposited at RT under different pressures of ambient oxygen using PLD. The films were used to conclusively confirm the dependence of random lasing action on the strength of scattering.

## Chapter 5

### Second Harmonic Generation from Pulsed Laser Deposited ZnO Thin Film

---

Nonlinear optics (NLO) is a powerful tool to generate coherent sources that may not be readily available through the lasing action in a medium [136]. Many types of lasers are commercially available offering a wide variety of different output wavelengths. However, the number of different wavelengths available in ultraviolet region of spectrum is somewhat limited. Since its discovery by P. Franken [137], the field of NLO has established itself as an important research tool, benefiting several areas of science and technology. The most important applications of NLO arise from the possibility of converting coherent laser radiation to new frequencies. Thus the frequency conversion in a suitable medium allows researchers to develop coherent sources of wavelengths those are required, with a broad tuning range, and/or at frequencies where coherent sources are simply not available.

In recent years there has been immense interest in the development of new optical materials for potential applications in electro-optic and integrated optical devices [53,138-139]. Development in integrated optics is dependent on advances in the development of thin film of materials with large nonlinear optical response. Most of the current efforts are focused on nonlinear optical waveguides of  $\text{LiNbO}_3$ ,  $\text{LiTaO}_3$  and KTP [140]. However, these waveguides require lattice matched substrates and expensive single crystals and have an inherent restriction of limited integrate ability. Thus, it is imperative to look for new optical materials that can be grown on a variety of substrates and are thermally stable.

ZnO, a II-VI semiconductor is a photonic material with attractive properties (*Table I, chapter 1*) like large direct band gap of 3.37 eV at room temperature (RT) and a high melting point of around 2300 °K. The extremely high melting point suggests the optical damage threshold of ZnO may be higher than those of many common NLO materials. The ease of fabrication of films of ZnO offers a flexibility to fabricate optical devices, such as frequency doublers and modulators on variety of substrates [141]. It is

expected that ZnO based optical devices could potentially operate in harsher chemical environment as well.

In this chapter we report the second harmonic generation from ZnO thin films deposited by pulsed laser under ambient oxygen pressures of  $10^{-2}$  Torr,  $10^{-1}$  Torr,  $3 \times 10^{-1}$  Torr,  $6 \times 10^{-1}$  Torr,  $9 \times 10^{-1}$  Torr and 1 Torr. We have used PLD for depositing thin films. The chapter starts with a brief general introduction of second harmonic generation. The experimental details are given in section 3 and the section 4 gives results and discussion of the deposited films.

### 5.1 Nonlinear Optical Effects in Crystals

Before the advent of lasers it was believed that the transparent optical materials are essentially passive unaffected by light traveling through them. After the discovery of high intensity laser light, for the first time it was possible to observe that the presence of light can affect the properties of the material. Intense light beam, for example, can change the refractive index or absorption properties of an optical material. When this happens, the light itself is affected by change in a nonlinear way. The nonlinear response of the material can change the laser light into new colors, both harmonics of the optical frequency and when more than one frequency is present in the input light, sum and difference frequencies. In order to describe more precisely what is meant by an optical non-linearity, let us consider how the dipole moment per unit volume, or polarization  $\vec{P}(t)$ , of a material system depends upon the strength  $\vec{E}(t)$  of the applied optical field. The electric field of electromagnetic radiation interacts with the electric field within the molecules of the crystalline medium. It polarizes the atoms by slightly displacing the electrons along the direction of the field. In the case of conventional (i.e., linear) optics, the induced polarization depends linearly upon the electric field strength in a manner that can be described by the relation

$$\vec{P}(t) = \epsilon_0 \chi^{(1)} \vec{E}(t), \quad (5.1)$$

where the constant of proportionality  $\chi^{(1)}$  is known as the linear susceptibility. This linear relationship between  $\vec{P}(t)$  and  $\vec{E}(t)$  generally fails to give an accurate description of the medium polarization for strong external electric fields  $|\vec{E}| \gg 1$  kV/cm, such as those

present in laser radiation. The high electric fields of lasers induce an appreciable nonlinear response in crystals. The non-linear optical response can often be described by generalizing equation (5.1) by expressing the polarization  $\vec{P}(t)$  as a power series in the field strength  $\vec{E}(t)$  as,

$$\begin{aligned}\vec{P} &= \epsilon_0 (\chi^{(1)} \vec{E} + \chi^{(2)} \vec{E}^2 + \chi^{(3)} \vec{E}^3 + \dots) \\ &\equiv \vec{P}^{(1)}(t) + \vec{P}^{(2)}(t) + \vec{P}^{(3)}(t) + \dots\end{aligned}\quad (5.2)$$

The quantities  $\chi^{(2)}$  and  $\chi^{(3)}$  are known as second and third order non-linear optical susceptibilities, respectively. In writing the equations in the form above, we have also assumed that the polarization at time  $t$  depends only on the instantaneous value of the electric field strength. The assumption that the medium responds instantaneously also implies that the medium must be lossless and dispersionless.

The contribution to the induced polarization rapidly decreases with increasing order of nonlinear susceptibility. The second term  $\vec{P}^{(2)}(t) = \chi^{(2)} \vec{E}(t)^2$  gives rise to second harmonic generation (SHG), the third term  $\vec{P}^{(3)}(t) = \chi^{(3)} \vec{E}(t)^3$  to third-harmonic generation (THG), and so on. It is possible to make a simple order of magnitude estimate of the size of these quantities for the common case in which the non-linearity is electronic in origin. It is expected that the lowest order correction term  $\vec{P}^{(2)}$  would be comparable to the linear response term  $\vec{P}^{(1)}$  when the amplitude of the applied field strength  $\vec{E}(t)$  is of the order of the characteristic atomic field strength  $E_{at} = e/a_0^2$ , where  $-e$  is the charge of the electron,  $a_0 = \hbar^2 / m e^2$  is the atomic Bohr radius of the hydrogen atom and  $m$  is the mass of the electron. On putting numerical values we find that  $E_{at} = 2 \times 10^7$  e.s.u. We thus expect that under conditions of non-resonant excitation the second order susceptibility  $\chi^{(2)}$  will be of the order of  $\chi^{(1)}/E_{at}$ . For condensed matter  $\chi^{(1)}$  is of the order of unity, and we hence expect that  $\chi^{(2)}$  will be of the order of  $1/E_{at}$ , or

$$\chi^{(2)} \cong 5 \times 10^{-8} \text{ esu} = 5 \times 10^{-8} \frac{\text{cm}}{\text{statvolt}}$$

Similarly, we expect  $\chi^{(3)}$  to be of the order of  $\chi^{(1)}/E_{at}^2$ , or

$$\chi^{(3)} \equiv 3 \times 10^{-15} \text{ esu} = 3 \times 10^{-15} \frac{\text{cm}^2}{\text{statvolt}^2}$$

It follows from above calculations  $\chi^{(2)} \gg \chi^{(3)}$

## 5.2 Second Harmonic Generation

As is said before for an isotropic medium and for a weak field  $\vec{P}$  is proportional to  $\vec{E}$  i.e.

$$\vec{P}(t) = \epsilon_0 \chi \vec{E}(t)$$

The displacement vector  $\vec{D}$  is given by,

$$\vec{D} = \epsilon_0 \vec{E} + 4\pi \vec{P} \quad (5.3)$$

and  $\vec{D} = \epsilon \vec{E}$  where  $\epsilon = \epsilon_0 (1 + \chi)$  represents the dielectric permittivity and  $\chi$  the electric susceptibility of the material. For very high fields the polarization has a nonlinear dependence on the electric field and we may write,

$$\vec{D} = \epsilon \vec{E} + 4\pi \vec{P}_{nl} \quad (5.4)$$

where  $\vec{P}_{nl}$  represents the nonlinear part of the polarization that becomes negligible for weak fields.

In order to understand the generation of the second harmonic we start with a charge free, non-conducting and nonmagnetic homogenous medium so that Maxwell's Equations lead to the following equation

$$\nabla^2 \vec{E} = \frac{\partial}{\partial t} (\nabla \times \vec{H}) = \frac{1}{c^2} \frac{\partial^2 \vec{D}}{\partial t^2} \quad (5.5)$$

Substituting in equation (5.4) we get,

$$\nabla^2 \vec{E} - \frac{\epsilon}{c^2} \frac{\partial^2 \vec{E}}{\partial t^2} = \frac{4\pi}{c^2} \frac{\partial^2}{\partial t^2} \vec{P}_{nl} \quad (5.6)$$

We should mention here that in the derivation of above equation, we have used the condition  $\nabla \cdot \vec{E} = 0$  which is strictly valid only in isotropic medium. In an anisotropic medium this condition is not valid, however, for practical crystals  $\vec{E}$  is almost perpendicular to  $k$  and therefore we may assume  $\nabla \cdot \vec{E} \approx 0$ . In equation (5.6)  $\vec{E}$  represents the actual field and therefore can be assumed of the form

$$\vec{E} = \vec{E}_0 \cos(\omega t - kz + \phi) \quad (5.7)$$

where  $\vec{E}$  and  $\phi$  (phase) are real quantities. Equation (5.7) can also be written in the form

$$\begin{aligned} \vec{E} &= \text{Re}(\vec{E}_0 e^{i(\omega t - kz)}) \\ &= \frac{1}{2}(\vec{E}_0 e^{i(\omega t - kz)} + \text{c.c.}) \end{aligned} \quad (5.8)$$

Where c.c. stands for the complex conjugate of the quantity preceding it, the amplitude  $\vec{E}_0$  may be complex.

We consider a wave of frequency  $\omega$  propagating through the medium and consider the generation of the second harmonic frequency  $2\omega$  as the beam propagates through the medium. The field at  $\omega$  generates a polarization at  $2\omega$  which acts as a source for the generation of an electromagnetic field wave at  $2\omega$ . Corresponding to the frequencies  $\omega$  and  $2\omega$  the electric field is given by

$$\vec{E}^{(\omega)} = \frac{1}{2}(\vec{E}_1(z)e^{i(\omega t - k_1 z)} + \text{cc}) \quad (5.9)$$

and

$$\vec{E}^{(2\omega)} = \frac{1}{2}(\vec{E}_2(z)e^{i(2\omega t - k_2 z)} + \text{cc}) \quad (5.10)$$

respectively. The quantities

$$k_1 = (\omega / c)n_1 \quad (5.11)$$

and

$$k_2 = (2\omega / c)n_2 \quad (5.12)$$

represent the propagation vectors at  $\omega$  and  $2\omega$  respectively;  $\epsilon_1$  and  $\epsilon_2$  represent the dielectric permittivities at  $\omega$  and  $2\omega$ , and  $n_1$  and  $n_2$  represent the corresponding wave refractive indices.

It should be noted that the amplitudes  $|\vec{E}_1|$  and  $|\vec{E}_2|$  are assumed to be  $z$  dependent –this is because at  $z=0$  (where the beam is incident on the medium) the



amplitude  $|\vec{E}_2|$  is zero and it develops as the beam propagates through the medium. In order to consider SHG, we write the wave equation corresponding to  $2\omega$ ;

$$\nabla^2 \vec{E}^{(2\omega)} - \frac{\epsilon_2}{c^2} \frac{\partial^2 \vec{E}^{(2\omega)}}{\partial t^2} = \frac{4\pi}{c^2} \frac{\partial^2}{\partial t^2} \vec{P}^{(2\omega)}_{nl} \quad (5.13)$$

The non-linear polarization at  $2\omega$  can be written as

$$\vec{P}^{(2\omega)}_{nl} = \frac{1}{2} (\vec{P}^{(2\omega)}_{nl} e^{2i(\omega t - k_1 z)} + cc) \quad (5.14)$$

With

$$\vec{P}^{(2\omega)}_{nl} = \chi^{(2)}_{eff} \vec{E}_1(z) \cdot \vec{E}_1(z) \quad (5.15)$$

and the parameter  $\chi^{(2)}_{eff}$  depends on the non-linear material. Substituting for  $\vec{E}^{(2\omega)}$  and  $\vec{P}^{(2\omega)}_{nl}$  from (5.10) and (5.14) in equation (5.13) and equating terms proportional to  $e^{2i\omega t}$  we obtain

$$\begin{aligned} & [\nabla^2 + \frac{\epsilon_2}{c^2} (2\omega)^2] \vec{E}_2(z) e^{i(2\omega t - k_2 z)} \\ &= -\frac{4\pi}{c^2} (\chi^{(2)}_{eff})^2 (4\omega^2) \vec{E}_1(z) \cdot \vec{E}_1(z) e^{2i(\omega t - k_1 z)} \end{aligned} \quad (5.16)$$

The L.H.S can be written as,

$$\begin{aligned} & [\nabla^2 + \frac{\epsilon_2}{c^2} (2\omega)^2] \vec{E}_2(z) e^{i(2\omega t - k_2 z)} \\ &= [-k_2^2 \vec{E}_2 - 2ik_2 (d\vec{E}_2(z)/dz) + (2\omega)^2 \frac{\epsilon_2}{c^2} \vec{E}_2(z)] e^{i(2\omega t - k_2 z)} \\ &\approx -2ik_2 (d\vec{E}_2(z)/dz) e^{i(2\omega t - k_2 z)} \end{aligned} \quad (5.17)$$

Where we have used the relation  $k_2^2 = (2\omega)^2 \epsilon_2 / c^2$  and have neglected the term proportional to  $d^2 E_2 / dz^2$ , i.e. we have assumed

$$d^2|\bar{E}_2(z)|/dz^2 \ll k_2(d|\bar{E}_2(z)|/dz) \text{ or,}$$

$$\frac{1}{k_2(d|\bar{E}_2(z)|/dz)} \frac{d}{dz} \left( \frac{d|\bar{E}_2(z)|}{dz} \right) \ll 1 \quad (5.18)$$

The above equation implies that the distance over which  $d|\bar{E}_2(z)|/dz$  changes appreciably is large compared to the wavelength (it is indeed true for all practical cases). Substituting equation (5.17) in equation (5.16) we obtain

$$\frac{d|\bar{E}_2|}{dz} = -\frac{4\pi i \chi_{eff}^{(2)} \omega}{n_2 c} |\bar{E}_1|^2(z) e^{i(\Delta k)z} \quad (5.19)$$

where,

$$\Delta k = k_2 - 2k_1 = (2\omega/c)(n_2 - n_1) \quad (5.20)$$

In order to solve equation (5.19) we assume that the field  $\bar{E}_1(z)$  depletes very slightly (with  $z$ ) so that the quantity  $E_1^2$  on the RHS can be assumed to be independent of  $z$ . On integrating equation (5.19), we obtain

$$|\bar{E}_2(z)| = -\frac{4\pi i \chi_{eff}^{(2)} \omega}{n_2 c} z |\bar{E}_1(z)|^2 e^{i\beta} \frac{\sin \beta}{\beta} \quad (5.21)$$

where,

$$\beta = \frac{1}{2}(\Delta k)z = (\omega/c)(n_2 - n_1)z \quad (5.22)$$

If  $A$  represents the area of cross section of the beam then the power associated with the waves  $\omega$  and  $2\omega$  is given by

$$P_\omega = A(n_1 c / 2\pi) |E_1|^2 \quad (5.23)$$

$$P_{2\omega} = A(n_2 c / 2\pi) |E_2|^2 \quad (5.24)$$

Substituting for  $|E_2|$  from equation (5.21) and then using equation (5.23) and equation (5.24), we get after some simplifications [142],

$$\eta = \frac{P_{2\omega}}{P_{\omega}} = \frac{32\pi^3 \times (\chi_{eff}^{(2)})^2 \omega^2}{n_1^2 n_2 c^3 A} z^2 P_{\omega} \left( \frac{\sin \beta}{\beta} \right)^2 \quad (5.25)$$

where  $\eta$  represents the second harmonic efficiency.

The most important factor in above equation is  $(\sin\beta/\beta)^2$  which has a maximum value of 1 at  $\beta=0$ . Thus for maximum SHG efficiency  $\beta=n_1=n_2=0$ .i.e. the refractive index at  $2\omega$  must be equal to refractive index at  $\omega$  which is known as phase matching condition. It follows from equation (5.25) for a fixed  $\Delta k$ , the function periodically varies with  $\beta$ , coherence length. For oblique incidence  $\beta$  will be equal to:

$$\beta = \frac{2\pi L}{\lambda} (n_1 \cos \theta_{\omega} - n_2 \cos \theta_{2\omega}) \quad (5.26)$$

### 5.3 Second Harmonic Generation in Thin Films

In order to use general equation (5.25) for thin films in ZnO we have modeled the thin films as four layer system i.e. air-film-substrate-air as shown in figure 5.1.

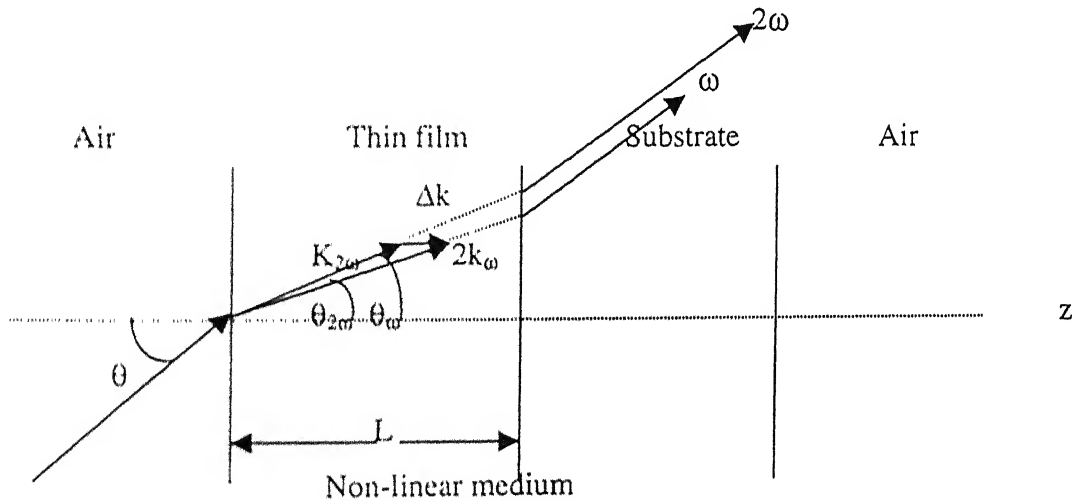


Figure 5- 1: A ray diagram of the four layer thin film system of non-linear optical material generating second harmonic

Absorption of the fundamental and second harmonic of the beam is negligible by the film as the band gap of ZnO is far above these wavelengths. The Fresnel coefficients are evaluated following [143]. Fresnel transmission coefficient for fundamental frequency  $\omega$  at air-film interface can be written as,

$$t_{af}^{1p} = \frac{2 \cos \theta}{(n_{\omega} \cos \theta + \cos \theta_{\omega})} \quad (5.27)$$

when the plane of polarization of the incident electric field is perpendicular to the plane of incidence.

Similarly for second harmonic frequency  $2\omega$ , Fresnel transmission coefficient at the film-substrate or substrate-air can be written as,

$$t_{fs}^{2p} = 2n_{2\omega} \cos \theta_{2\omega} \times \frac{(\cos \theta + n_{\omega} \cos \theta_{\omega})(n_{\omega} \cos \theta_{\omega} + n_{2\omega} \cos \theta_{2\omega})}{(n_{2\omega} \cos \theta_{2\omega} + \cos \theta)^3} \quad (5.28)$$

Using  $P_{2\omega} = n_{2\omega} \cos \theta_{2\omega} I_{2\omega}$  and  $P_{\omega} = n_1 \cos \theta_{\omega} I_{\omega}$  in equation (5.25) where  $I_{2\omega}$  and  $I_{\omega}$  are the intensities for fundamental and second harmonic respectively and Fresnel transmission coefficients  $t_{af}^{1p}, t_{fs}^{2p}, t_{sa}^{2p}$ , at the air-film, film-substrate and substrate air interfaces, the intensity of second harmonic after transmitting through the thin film can be written as;

$$I_{2\omega}(\theta) = \frac{128\pi^3}{cA} \frac{(t_{af}^{1p})^4 (t_{fs}^{2p})^2 (t_{sa}^{2p})^2}{(n_2 \cos \theta_{2\omega})^2} \times I_{\omega}^2 \left( \frac{2\pi L}{\lambda} \right)^2 (\chi_{eff}^{(2)})^2 \frac{\sin^2 \beta}{\beta^2} \quad (5.29)$$

Where  $A$  is the area of the incident beam spot,  $I_{\omega}$  is the intensity of the incident fundamental beam,  $L$  is the film thickness ( $z=L$  in equation 5.27),  $\theta_{\omega}$  ( $\theta_{2\omega}$ ) is determined from  $\sin \theta = n_1 \sin \theta_{\omega}$  ( $\sin \theta = n_2 \sin \theta_{2\omega}$ ). Now if the incident angle  $\theta$  changes continuously then  $\theta_{\omega}$  and  $\theta_{2\omega}$  also change, it follows from equation (5.26) the coherence length  $\beta$  of the film changes. Variation of second harmonic intensity versus incident angle produces a fringe pattern called Maker fringes [145,146].

#### 5.4 Experimental details:

The details of the setup used for depositing ZnO thin film are given in Chapter 2. Briefly, the thin film of ZnO were deposited using the third harmonic (355 nm) of a Nd:YAG laser at pulse repetition rate 10 Hz. and pulse width of 5 ns (FWHM). Thin films were deposited on a glass substrate at distance of 4 cm at room temperature under oxygen gas ambient. Ambient gas pressure of oxygen was varied from 10 mTorr to 1000

mTorr. Experimental set-up for studying the second harmonic generation of ZnO is shown in Figure 5.2. We have used p polarized, fundamental wavelength of (1.06  $\mu\text{m}$ ) Nd:YAG laser for generation of second harmonic. The incident angle of the fundamental beam of Nd:YAG laser is continuously varied. After passing through the thin film, second harmonic of the fundamental beam is detected by a photodiode. Fundamental beam is cutoff using a filter and only second harmonic reflected by dichoric mirror, is ultimately detected by a photodiode.

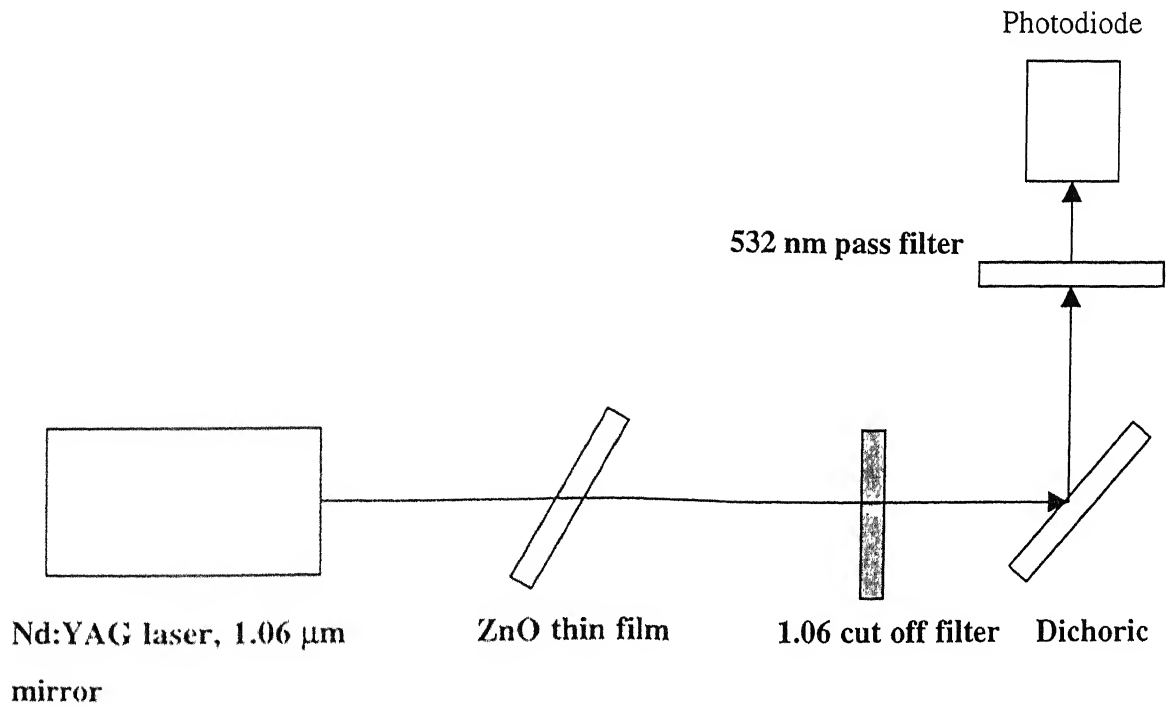


Figure 5- 2: Experimental set-up for Second Harmonic Generation

## 5.5 Results and Discussions

We have used equation (5.29) for analyzing second harmonic generation in pulsed laser deposited ZnO thin films.  $\chi_{\text{eff}}^{(2)}$  in equation (5.29) represents the effective second order susceptibility. Since ZnO has the hexagonal close packed (hcp) structure with the 6 mm symmetry, individual crystallite should have only four nonzero components [147] of the second order susceptibility tensor:  $\chi_{xzx}^{(2)} = \chi_{yzy}^{(2)}$ ,  $\chi_{xxz}^{(2)} = \chi_{yyz}^{(2)}$ ,  $\chi_{zxx}^{(2)} = \chi_{zyy}^{(2)}$ , and

$\chi_{zzz}^{(2)}$ , where the coordinates correspond to the crystal axes of individual crystallite. When the frequencies involved are far from resonances, Kleinmen's symmetry condition can be applied to further reduce the number of independent components to two [147]:  $\chi_{xxz}^{(2)} = \chi_{yyz}^{(2)} = \chi_{xzx}^{(2)} = \chi_{yyx}^{(2)} = \chi_{zxx}^{(2)} = \chi_{zyy}^{(2)}$ , and  $\chi_{zzz}^{(2)}$ . Assuming that individual crystallite average to a texture axis, the tensorial property of the ZnO film (including all the crystallites and the grain boundaries) is equivalent to that of an isotropic uniaxial medium. A large second harmonic intensity observed in our films indicates that a high degree of texturing exists in the film, a fact that is corroborated by XRD results of the deposited films, chapter 3.

Second harmonic coefficients ( $\chi_{\text{eff}}^{(2)}$ ) for different films deposited at different ambient pressures is evaluated by fitting the experimental data with equation (5.29). Depending on the polarization of the fundamental beam, the second harmonic coefficient can be written as,

$$\chi_{\text{eff}}^{(2)} = \chi_{zxx}^{(2)} \sin \theta_{2\omega} \quad (5.30)$$

For s-polarized fundamental beam and for a p-polarized beam we have

$$\chi_{\text{eff}}^{(2)} = \chi_{zxx}^{(2)} (\cos \theta_{2\omega} \sin 2\theta_{\omega} + \sin \theta_{2\omega} \cos^2 \theta_{\omega}) + \chi_{zzz}^{(2)} \sin \theta_{2\omega} \sin^2 \theta_{\omega} \quad (5.31)$$

To get  $\chi_{zxx}^{(2)}$  from experimental observation and equation (5.29) and equation (5.30), we need  $I_{\omega}^2/A$ . To get the value of  $I_{\omega}^2/A$  we substituted ZnO thin film with a KDP crystal whose second harmonic coefficient is known. SHG intensity was measured as a function of the incident angle of the fundamental beam. The variation of SHG intensity with angle of the incident fundamental beam at  $10^{-1}$  Torr,  $3 \times 10^{-1}$  Torr,  $6 \times 10^{-1}$  Torr and  $9 \times 10^{-1}$  Torr of oxygen pressure is shown in figure 5.3. Figure 5.4 and 5.5 show the variation of  $\chi_{zxx}^{(2)}$  with the deposition pressure and the grain size of ZnO crystallites. It is found that the films at lower pressure, have higher second harmonic generation coefficient ( $\chi_{\text{eff}}^{(2)}$ ) than those deposited at higher pressure. This may be due to the poor crystallinity and orientations of the films at lower pressure [103]. Another reason may be the grain size of the film [148]. At higher pressures grain size of the film is more than those deposited at lower pressure.

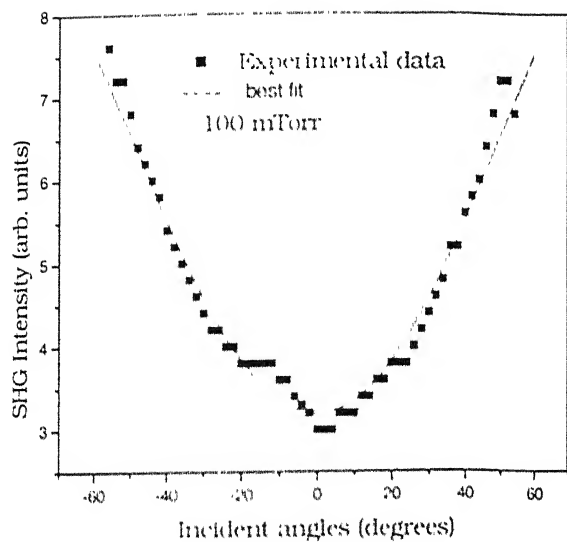


Figure 5.3 (a)

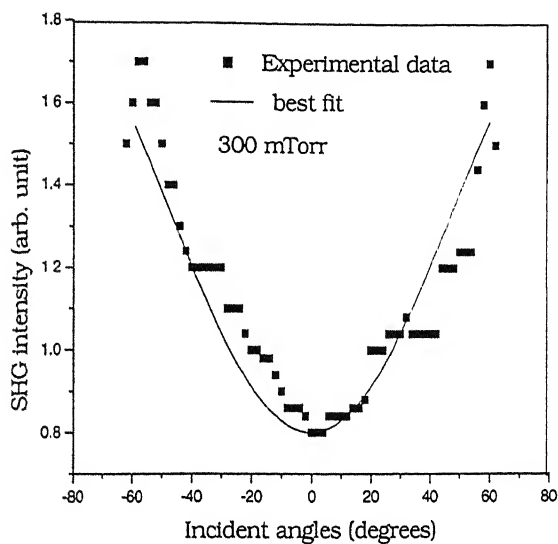


Figure 5.3 (b)

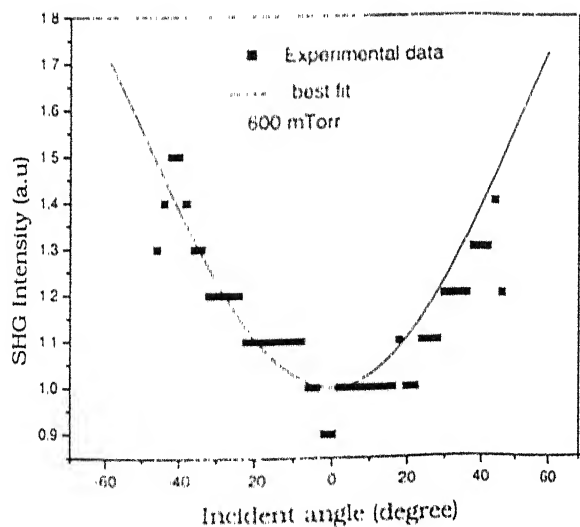


Figure 5.3 (c)

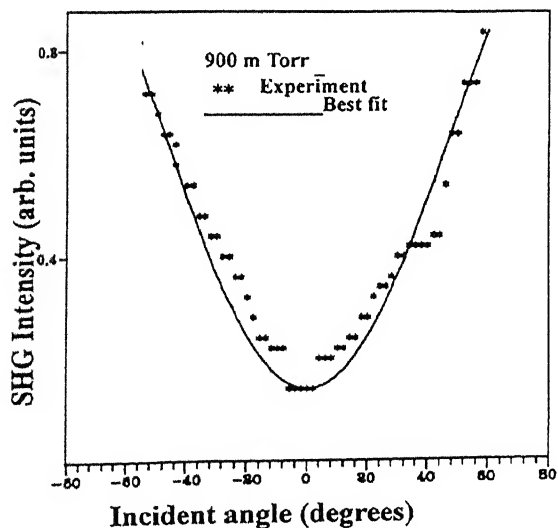


Figure 5.3 (d)

Figure 5- 3: Angular dependence of second harmonic intensity of the ZnO films deposited at (a)  $10^{-1}$  Torr, (b)  $3 \times 10^{-1}$  Torr, (c)  $6 \times 10^{-1}$  Torr and (d)  $9 \times 10^{-1}$  Torr of oxygen.

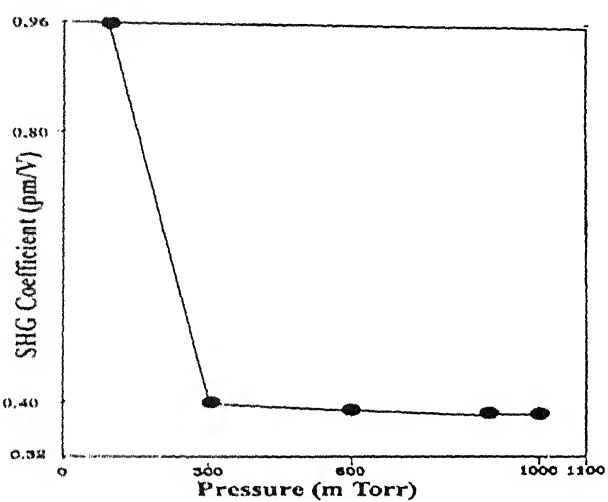


Figure 5- 4: Variation of SHG coefficient with ambient pressure of oxygen

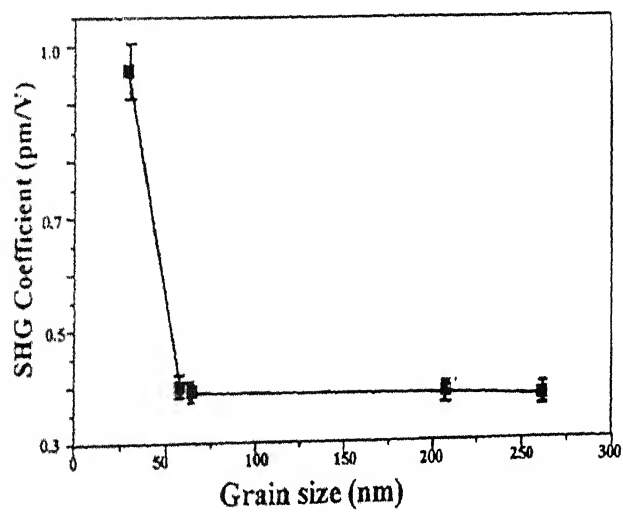


Figure 5- 5: Variation of SHG coefficient with grain size of ZnO crystallites



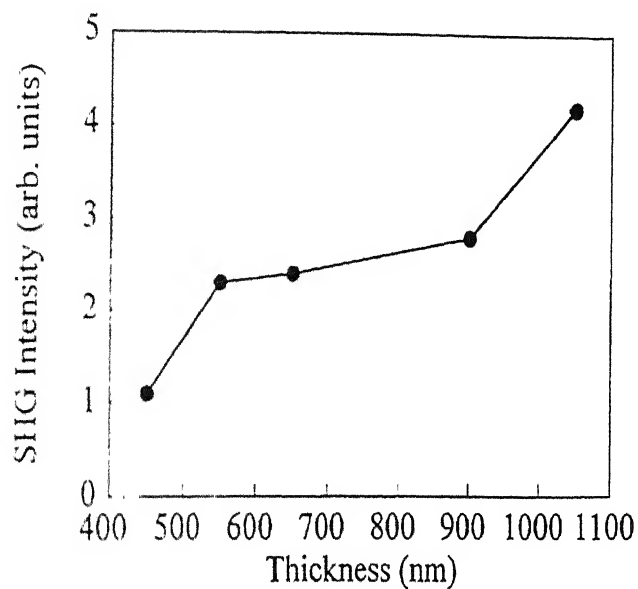


Figure 5- 6: Variation of SHG intensity with film thickness of ZnO

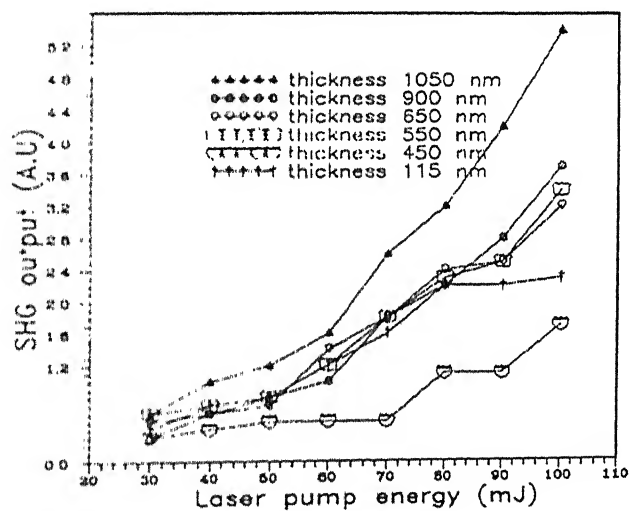


Figure 5- 7: Variation of SHG intensity with laser pump energy.

We have also studied the variation of second harmonic generation with increasing input energy of the fundamental for different thickness of the films. Figure 5.7. shows variation of second harmonic generation of thicker films change rapidly with increasing input. The thickness of the films was measured by RBS. The thickness of 115 nm, 450 nm, 550 nm, 700 nm and 1050 nm deposited under 10, 100, 300, 600, 900 mTorr and 1 Torr respectively was estimated. Though the second harmonic generation coefficient is more for the films deposited at lower pressure, the films deposited at higher pressure show more second harmonic generation as shown in figure 5.8 due to the thicker films. It implies that second harmonic generation does not only depend on the crystallinity but also on the thickness of the films[149].

## 5.6 Conclusions

In conclusion we have studied second harmonic generation in pulsed laser deposited thin films of ZnO of varying crystallinity. It was found that films deposited at lower pressures have higher second harmonic generation coefficient ( $\chi_{\text{eff}}^{(2)}$ ) than those deposited at higher pressures. Thicker films showed a strong dependence of SHG on the input energy.

## Chapter 6

### Conclusion and scope of future work

---

We have reported the deposition of ZnO thin films using pulsed laser deposited techniques under different conditions for its applications as UV source. Films were characterized using X-ray diffraction (XRD), Atomic Force Microscopy (AFM), Photoluminescence (PL), and Rutherford Backscattering (RBS) prior to looking for random lasing action in ZnO pellet as well as thin films. The dependence of PL and lasing properties on crystallite size of ZnO is discussed. Nonlinear optical properties of ZnO thin films are also studied.

XRD of the films showed that the films grown at pressures less than  $3 \times 10^{-1}$  Torr to be highly oriented along (002) plane, implying c-axis of the film uniformly perpendicular to the surface. At pressures greater than or equal to  $3 \times 10^{-1}$  Torr, the planes (101), (002), (100) are observed. The broadened diffraction peaks (FWHM) with increasing pressure imply that the particle size increases at higher ambient pressures. The average diameter of nanocrystallites is estimated using the broadening of the diffraction peaks in the Scherrer's formula. The size of nanocrystallites varied from 7 to 16 nm (with an error of less than 20 %). The substrate temperature, ambient gas pressure and target substrate distance, in addition to laser parameters are the factors that control the width of the diffraction peaks and hence the size of the nanocrystallites. It is expected that at higher pressures, the compressed plasma plume will lead to nucleation of larger ZnO clusters. Therefore, it is possible to control the size of clusters by controlling the ambient gas pressure. However, it is important for ZnO film growth that the amount of reactive oxygen created from the ambient gas be sufficient to help reduce the number of oxygen vacancies.

Surface morphology of the films was studied using AFM. Measurements were done in air. Film samples were scanned over areas ranging from  $500 \times 500 \text{ nm}^2$  to  $10 \times 10 \text{ }\mu\text{m}^2$  at several different locations on the film surface. Surface morphology varied among films grown at various different ambient pressures. The films grown at lower oxygen

pressures were smoother than those grown at higher pressures. At pressures greater than  $3 \times 10^{-1}$  Torr the film became powdery with observable clustering of grains. However, the films deposited at  $10^{-1}$  Torr show a particular orientation direction, in confirmation with XRD. The average roughness varied from 20 to 108 nm within the scanned area of  $1 \times 1 \mu\text{m}^2$  in the pressure range studied. The root mean square (r. m. s.) value of the grain size ranged from 20 to 200 nm. AFM pictures showed the clusters formation at pressure of greater than equal to 1 Torr.

Photoluminescence study was done for the ZnO thin films. In our work we obtained only one peak around 390 nm implying that grown films are defect free. The intensity of the strong PL peak observed at 395 nm decreases with the increase in ambient oxygen pressure. This may be due to unfavorable Zn:O ratio at higher pressures of oxygen.

The thickness and composition of the films was measured using Rutherford Backscattering technique. The thickness of the films is observed to increase with the increase in pressure of the ambient oxygen. The thickness of the deposited films varies from 115 nm to 1050 nm at pressure of  $10^{-2}$  Torr to 1 Torr. The composition Zn:O of the films varied from 1:1 at lower pressures to 1:2.5 at pressures greater than  $10^{-2}$  Torr.

Random lasing action in bulk ZnO pellet as well as in ZnO thin films has been observed. A steep rise in the output after the input pump energy exceeds  $1500 \text{ kW/cm}^2$ , has been observed which can be taken as the lasing threshold. Below the threshold excitation intensity, the spectrum observed is a single broad spontaneous emission peak. As the input intensity increases, the emission becomes narrower due to preferential amplification at frequencies close to the maximum of the gain spectrum. At excitation intensity above threshold very narrow peaks are observed in the emission spectrum. The line width of these peaks decreased to less than 0.6 nm, which is more than 25 times smaller than the line width of amplified spontaneous emission below threshold. In our samples average particle size is 20 nm the scattering mean free path is as short as  $0.232 \mu\text{m}$  and hence many closed loops may be formed. These loops could serve as ring cavities having different losses. The discrete peaks observed in emission spectra clearly show the laser emission. The dependence of laser action on excitation volume and excitation intensity was studied by varying the excitation area. As the excitation area

increases the lasing threshold pump intensity decreases and more lasing peaks are observed in the emission spectra. However, the laser oscillations stopped once the excitation area decreased below a critical area. The optical gain of the laser was measured by measuring the laser output (above threshold) for two excitation lengths. We obtained the gain coefficient  $7.50 \text{ cm}^{-1}$ .

Random lasing action in pulsed laser deposited ZnO thin films also showed a lasing threshold. To observe laser action, films of various thickness were optically pumped by third harmonic of Nd:YAG laser. Similar to ZnO pellet a single broad emission peak is observed below the threshold excitation intensity. A steep increase in the output intensity as the pump laser exceeds an intensity of  $2387 \text{ kW/cm}^2$  is observed. At excitation above threshold very narrow peaks, almost 10 times narrower than the emission below lasing threshold, are observed in the emission spectrum. In the case of thin film the emission spectrum also becomes narrower due to preferential amplification at frequencies close to the maximum of the gain spectrum. Due to local variation of particle density and spatial distribution in the films, there exist small regions of higher disorder and stronger scattering and of lower disorder and weaker scattering. Light can be confined in these regions forming closed loop feedback paths through multiple scattering and interference. Laser oscillations occur once the optical gain in a cavity exceeds the losses of a cavity. The various peaks observed in the emission spectrum are the cavity resonant frequencies. Increasing thickness of the film can lead to three-dimensional localization of light and hence to increased emission. To confirm, ZnO films of thickness 0.5, 1 and  $1.5 \mu\text{m}$  were pumped at intensity of  $3310 \text{ kW/cm}^2$ . The films were deposited at ambient pressure of  $10^{-1}$  Torr. Films deposited at higher pressures did not yield good results due to poor stoichiometry. It is also confirmed by PL and RBS studies. The intensity of the laser emission increased with the increase of film-thickness. The increased emission is attributed to a longer optical path in thick films contributing to amplification.

An extensive investigation of the nonlinear optical properties of ZnO thin films deposited under different ambient pressures of oxygen was done. Second harmonic coefficient ( $\chi_{\text{eff}}^{(2)}$ ) for different films deposited under different ambient pressures is evaluated by fitting the experimental data with the equation which generates the Maker

fringes. Variation of second harmonic intensity versus incident angle produces a Maker fringe pattern. It is found that the films at lower pressure have higher second harmonic generation coefficient ( $\chi_{\text{eff}}^{(2)}$ ) than those deposited at higher pressure. This is due to the poor crystallinity and orientations of the films at lower pressure. Another reason may be the grain size of the film. At higher pressures grain size of the film is larger than those deposited at lower pressure.

The second harmonic generation shows a steep increase with the increase in input energy of the fundamental for thicker films. The thickness of the films as measured by RBS is 115 nm, 450 nm, 550 nm, 700 nm and 1050 nm deposited under pressure of  $10^{-2}$  Torr,  $10^{-1}$  Torr,  $3 \times 10^{-1}$  Torr,  $6 \times 10^{-1}$  Torr,  $9 \times 10^{-1}$  Torr and 1 Torr respectively. Though the second harmonic generation coefficient is more for the films deposited at lower pressure, the films deposited at higher pressure show more second harmonic generation due to the thicker films. It implies that second harmonic generation does not only depend on the crystallinity but also on the thickness of the films.

### Future scope of work

Though in last several years lot of papers have been published on ZnO thin films on its applications as an optical material, a lot is yet to be done before it can be used for commercial purpose. Greatest challenge in this regard is the fabrication of p-type ZnO. For making semiconductor LED or laser it is essential to make p-type semiconductor. There are only few reports of making p-type ZnO oxide by using  $\text{N}_2$ ,  $\text{NO}_2$  and  $\text{NH}_3$  but the results are not very promising.

Fabrication of quantum dots, wires or nanocrystalline thin films of ZnO open up another advancement in this field. One can vary the band gap as well as the luminescence process can be made more efficient for ZnO using the quantum confinement effect.

Doping of ZnO with MgO, CdO or other metal oxides, it is possible to tune the band gap from 3.3 eV to 4 eV. Superlattices of ZnO and MgO can also be used as useful UV source as well as detector.

Random lasing action in ZnO thin film as well as powder is new phenomenon which has been observed very recently. Till today there is no theoretical model which can conclusively explain it. More theoretical as well as experimental work is needed in order

---

to explain this new phenomenon. This has a potential of applications as display devices. As a non-linear optical material ZnO can have potential in the field of integrated optics.

## References

---

1. T. Mitsuyu, S. Ono and K. Wasa, J. Appl. Phys. **51** (1980) 2646.
2. Y.Ito, K. Kushida, H. Kanda, H. Takeuchi, K. Sugaware and H. Onozato, Ferroelectrics **134** (1992) 325.
3. T. Yamazaki, S. Wada, T. Noma and T. Suzuki, Sens. Actuators, B **13–14** (1993) 594.
4. W.W.Wenas, A. Yamada and K. Takahashi, J. Appl. Phys. **70** (1991) 7119.
5. M.A. Hans, J. Qiu, J. M. DePuydt and H. Cheng, Appl. Phys. Lett. **59** (1991) 1272.
6. A.V.Nurmikko and R. Gunshor, Proceedings of the International Symposium on blue laser and light emitting diodes, Chiba University, 1996 3.
7. H.Morkoc, S.Strite, G. B.Gao, M.E.Lin and B.Sverdlov, J. Appl. Phys. **76** (1994) 1363.
8. S. Nakamura and G.Fasol, *Blue Laser Diodes*, (Springer, Berlin 1997)
9. S.Strite and H.Morkoc, J. Vac. Sci. Tech. B **10**, (1992) 1237.
10. J. M. Hvam, Solid. State Comm. **26** (1978) 987.
11. A. Ohmto, M. Kawasaki, T. Koida, H. Koinuma, Y. Sakurai, Y. Yoshida, M. Sumiya, S. Fuke, T. Yasuda and Y. Segawa, . Mate. Science Forum, **264** (1998) 1463.
12. R. D. Vispute, V. Talyansky, S. Choopun, R. P. Sharma, T. Venkatesan, M. He, X. Tang, J. B. Halperu, M. G. Spencer, Y. X. Li, L.G. Salamanca-Riba, A. A. Iliadis, K. A. Jones, Appl. Phys. Lett. **73** (1998) 348.
13. K-K. Kim, J-Hoon. Song, H-J. Jung, W-K. Choi, S-J. Park and J-Han. Song, J. Appl. Phys. **87** (2000) 3573.
14. S. H. Bae, S. Y. Lee, B. J. Jin and S. Im, Appl. Surf. Sci. **154-155**, (2000) 458.
15. Y. R. Ryu, S. Zhu, J. D. Budai, H. R. Chandrasekhar, P. F. Miceli, and H. W. White, J. Appl. Phys. **88** (2000) 201.
16. Y. F. Chen, D. Bagnall and T. Yao, Mate. Scie. Engg. B **75**, (2000) 190.



17. D. M. Bagnall, Y. F. Chen, Z. Zhu, T. Yao, S. Koyama, M. Y. Shen and T. Goto, *Appl. Phys. Lett.* **70** (1997) 2230.
18. D. M. Bagnall, Y. F. Chen, Z. Zhu, T. Yao, M. Y. Shen and T. Goto, *Appl. Phys. Lett.* **73** (1998) 1038..
19. A. Ohtomo, R. Shiroki, I. Ohkubo, H. Koinuma and M. Kawasaki, *Appl. Phys. Lett.* **75** (1999) 4088.
20. A. Ohtomo, K. Tamura, M. Kawasaki, T. Makino, Y. Segawa, Z. K. Tang, G. K. L. Wong, Y. Matsumoto and H. Koinuma, *Appl. Phys. Lett.* **77** (2000) 2204.
21. R. D. Vispute, V. Talyansky, Z. Trajanovic, S. Choopun, M. Downes, R. P. Sharma, T. Venkatesan, M. C. Woods, R. T. Lareau, K. A. Jones and A. A. Iliadis, *Appl. Phys. Lett.* **70** (1997) 2735.
22. F. Hamdani, A. Botchkarev, W. Kim, H. Morkoc, M. Yeadon, J. M. Gibson, S.-C. Y. Tsen and D. J. Smith, *Appl. Phys. Lett.* **70** (1997) 467.
23. T. Minami, K. Oohasi and S. Takata, *Thin Solid Films.* **193/194** (1990) 721.
24. G. A. Hirata, J. McKittrick, J. Siqueiros, O. A. Lopez, T. Cheeks, O. Contreras and J. Y. Yi, *J. Vac. Sci. Tech. A* **14** (1996) 791.
25. Y. Igasaki and H. Saito, *J. Appl. Phys.* **70** (1991) 3613.
26. M. Hiramatsu, K. Imaeda, N. Horio and M. Nawata, *J. Vac. Sci. Tech. A* **16** (1998) 669.
27. J. Hu and R. G. Gordon, *J. Appl. Phys.* **71** (1992) 880.
28. A. Suzuki, T. Matshusita, N. Wada, Y. Sakamoto and M. Okuda, *J. J. Appl. Phys.* **35** (1996) L56.
29. T. Minami, H. Sonohara, T. Kakumu and S. Takata, *J. J. Appl. Phys.* **34** (1995) L971.
30. H. Kim, C. M. Gilmore, J. S. Horwitz, A. Pique, H. Murata, G. P. Kushto, R. Schlaf, Z. H. Kafafi and D. B. Chrisey, *Appl. Phys. Lett.* **76** (2000) 259.
31. T. Minami, T. Miyata, S. Takata and I. Fukuda, *J. J. Appl. Phys.* **30** (1991) L117.
32. T. Minami, T. Maeno, Y. Kuroi and S. Takata, *J. J. Appl. Phys.* **34** (1995) L684.
33. D. C. Reynolds, D. C. Look and B. Jogai, *Solid. State Comm.* **99** (1996) 873.
34. Z. K. Tang, G. K. I. Wong, P. Yu, M. Kawasaki, A. Ohtomo, H. Koinuma and Y. Segawa, *Appl. Phys. Lett.* **72** (1998) 3270.

35. K. Minegish, Y. Koiwai, Y. Kikuchi, K. Yano, M. Kasuga, A. Shimizu, J. J. Appl. Phys. **36** (1997) L1453.
36. M. Joseph, H. Tabata and T. Kawai, J. J. Appl. Phys. **38** (1999) L-1205.
37. Xin-Li Guo, H. Tabata and T. Kawai, J. Cryst. Growth **223** (2001) 135.
38. A. van Dijken, J. Makkinje and A. Meijerink, J. of Luminescence, **92** (2001) 323.
39. Y. C. Kong et al. Appl. Phys. Lett. **78** (2001) 407.
40. M. H. Huang, S. Mao, H. Feick, H. Van, Y. Wu, H. Kind, E. Weber, R. Russo and P. Yang, Science, **292** (2001) 1897.
41. S. L. McCall, A. F. J. Levi, R. E. Slusher, S. J. Pearton, R. A. Logan, Appl. Phys. Lett. **60** (1992) 289.
42. O. Painter, R. K. Lee, A. Scherer, A. Yariv, J. D. O'Brien, P. D. Dapkus, I. Kim, Science **284** (1999) 1819.
43. J. L. Jewell, J. P. Harbison, A. Scherer, Y. H. Lee, L.T. Florez, IEEE J. Quant. Electron. **27** (1991) 1332.
44. R. D. Vispute, H. Wu and J. Narayan, Appl. Phys. Lett. **67** (1995) 1549.
45. H. Cao, J. Y. Xu, E. W. Seelig, R. P. H. Chang, Appl. Phys. Lett. **76** (2000) 2997.
46. D. S. Wiersma, P. Bartolini, A. Lagendijk, R. Righini, Nature (London) **390** (1997) 671.
47. H. Cao, J. Y. Xu, E. W. Seelig, R. P. H. Chang, Appl. Phys. Lett. **76** (2000) 2997
48. H. Cao, J. Y. Xu, D. Z. Zhang, S.-H. Chang, S. T. Ho, E. W. Seelig, X. Liu and R. P. H. Chang. Phys. Rev. Lett. **84** (2000) 5584.
49. S. Bethke, H. Pan and B. W. Wessels, Appl. Phys. Lett. **52** (1988) 138.
50. Y. Chen, D. M. Bagnall, H. J. Koh, K. T. Park, K. Hiraga, Z. Zhu and T. Yao, J. Appl. Phys. **84** (1998) 3912.
51. P. Zu, Z. K. Tang, G. K. L. Wong, M. Kawasaki, A. Ohtomo, H. Koinuma and Y. Segawa, Solid State Comm. **103** (1997) 459.
52. B. Joseph, K. G. Gopchandran, P. K. Manoj, J. T. Abraham, P. Koshy and V. K. Vaidyan, Indian J. Phys. A **72** (1998) 99.
53. S. Cho, J. Ma, Y. Kim, Y. Sun, G. K. L. Wong and J. B. Ketterson, Appl. Phys. Lett. **75** (1999) 2761.
54. H. Morgan and D. E. Brodie, Can. J. Phys. **60** (1982) 1387.

55. B. Joseph, K. G. Gopchandran, P. K. Manoj, P. Koshy and V. K. Vaidyan, Bull. Mate. Sci. **22** (1999) 921.
56. A. Mitra, R. K. Thareja, V. Ganesan, A. Gupta, P. K. Sahoo and V. N .Kulkarni, Appl. Surf. Sci. **174**, (2001) 232.
57. H. M. Smith and A. F. Turner, Appl. Opt. **4** (1965) 147.
58. D. Dijkkamp T. Venkatesan, X. D. Wu, S. A. Shaheen, N. Jisrawi, Y. H. Min-Lee, W. L. McLean, M. Croft, Appl. Phys. Lett. **51** (1987) 619.
59. X. D. Wu, D. Dijkkamp, S. B. Ogale, A. Inam. E. W. Chase, P. F. Miceli, C. C. Chang, J. M. Tarascon, T. Ventatesan, Appl. Phys. Lett. **51** (1987) 861.
60. D. B. Chrisey and G. K. Hubler, Eds., *Pulsed Laser Deposition of Thin Films* (Wiley, New York,1994).
61. D. B. Geohegan in ref 59, pp 115-165.
62. A. Misra and R. K. Thareja, Appl. Surf. Sci. **143** (1999) 56.
63. X. Li, T. Kawai, and S. Kawai, J. J. Appl. Phys. **33** (1994) L18.
64. D. P. Norton, B. C. Chakoumakos, J. D. Budai, D. H. Lowndes, B. c. Salea, J. R. Thomson and D. K. Christen, Science. **265** (1994) 2074.
65. X. -D.Xiang, X. Sun, G. Briceno, Y. Lou, K. Wang, H. Chang, W. G. Wallace-Freedman, S. Chen and P.G. Schultz, Science. **268** (1995) 1738.
66. X. Sun, C. Gao, J. Wang and X.-D.Xiang, Appl. Phys. Lett. **70** (1997) 3353.
67. L.-C. Chen, in ref. 59, pp-167-197.
68. P. R. Wilmott and J. R. Huber, Rev. Mod. Phys. **72** (2000) 315.
69. S. Witanachchi, K. Ahmed, P. Sakthivel, P. Mukherjee, Appl. Phys. Lett. **66** (1995) 1469.
70. H. Sankur and J. T. Cheung, Appl. Phys A **47** (1988) 271.
71. J. A. Greer and M. D. Taba, J. Vac. Sci. Tech. A **13** (1995) 1175.
72. H. Sankur and J. T. Cheung, J. Vac. Sci. Tech. **A1** (1983) 1806.
73. V. Graciun and J.Elders, J. G. E. Gardeiniers and I.W. Boyd, Appl. Phys. Lett. **65** (1994) 2963.
74. V. Graciun, S. Amirhaghi, D. Craciun, J. Elders, J. G. E. Gardeniers and I. W. Boyd, Appl. Surf. Sci. **86** (1995) 99.
75. S. Hayamizu, H. Tabata, H.Tanaka and T. Kawai, J. Appl. Phys. **80** (1996) 787.

76. S. Choopun, R. D. Vispute, W. Noch, A. Balsamo, R. P. Sharma, T. Venkatesan, A. Iliadis and D. C. Look, *Appl. Phys. Lett.* **75** (1999) 3947
77. S. H. Bae, S. Y. Lee, H. Y. Kim and S. Im, *Appl. Surf. Sci.* **168** (2000) 332.
78. T. Ohshima, R. K. Thareja, T. Ecyami and K. Ebihara, *Sci. and Tech. Adv. Matt.* **2** (2001) 517.
79. R. K. Dwivedi, Ph.D Thesis, IIT Kanpur, India. (1997)
80. B. D. Cullity, *X-ray Diffraction* (Addison-Wesley, Reading, MA, 1956).
81. G. Binning, C. F. Quate and Ch. Gerber, *Phys. Rev. Lett.* **56** (1986) 930.
82. D. Rugar and P. Hansma, *Phys. Today*. Oct. (1990) 23.
83. R. Corey, M. Kissner and P. Saulnier, *Am. J. Phys.* **63** (1995) 560.
84. M. P. van Albada and A. Lagendijk, *Phys. Rev. Lett.* **55** (1985) 2692.
85. P. E. Wolf and G. Maret, *Phys. Rev. Lett.* **55** (1985) 2696.
86. W. K. Chu, J. W. Mayer, and M. –A Nicolet, in *Backscattering Spectrometry* (Academic Press, New York, 1978).
87. L. R. Dolittle, *Nucl. Inst. Meth.* **B9** (1985)
88. S.Im, B.J.Jin and S.Yi, *J. App. Phys.* **87** (2000) 4558.
89. Y.F.Lu, H.Q. Ni, Z.H. Mai and Z.M. Ren, *J. App. Phys.* **88** (2000) 498.
90. M. Okoshi, K. Higashikawa and M. Hanabusa, *Appl. Surf. Sci.* **154-155** (2000) 424.
91. E. Millon, O. Albert, J.C. Loulergue, J. Etchepare, D. Hulin, W. Seiler and J. Perriere, *J. Appl. Phys.* **88** (2000) 6937.
92. M. Okoshi, K. Higashikawa and M. Hanabusa, *Jpn. J. Appl. Phys.* **40** (2001) 1287.
93. H. S. Carslaw and J. C. Jaeger, *Conduction of Heat in Solids* (Oxford: Oxford university press, 1959).
94. J. F. Ready, *Effects of High Power Laser Radiation*, (Academic, New York, 1971).
95. R. Kelly and A. Miotello, *Appl. Surf. Sci.*, **96-98** (1996) 205.
96. J. Dawson, P. Kaw and B. Green, *Phys. Fluids.* **12** (1969) 875.
97. R. K. Singh and J. Narayan, *Phys. Rev. B* **41** (1990) 8843.
98. Abhilasa, P. S. R. Prasad and R. K. Thareja, *Phys. Rev. E* , **48** (1993) 2929.

- 
99. A. Neogi and R. K. Thareja, *J. Appl. Phys.* **85** (1999) 1131.
100. R. K. Dwivedi, S. P. Singh and R. K. Thareja, *Int. J. Mod. Phys. B* **12** (1998) 2619.
101. P. R. Wilmott, R. Timm and J. R. Huber, *J. Appl. Phys.* **82** (1997) 2082.
102. R. P. van Ingen, *J. Appl. Phys.* **79** (1996) 467.
103. L. N. Dinh, M. A. Schilbach, M. Balooch and W. McLean II, *J. Appl. Phys.* **86** (1999) 1149.
104. I. Barin, *Thermochemical data of Pure Substances, Part II* (VCH Verlagsgesellschaft mbH, Germany, 1989).
105. J.A. Rodriguez and J. Hebek, *Catal. Lett.* **26** (1994) 393.
106. S. A. Studenikin, N. Golego, and M. Cocivera, *J. Appl. Phys.* **84** (1998) 2287.
107. T. C. Damen, S. P. S. Porto and B. Tell, *Phys. Rev.* **142** (1966) 570.
108. Z. Zhaochun, H. Baibiao, Y. Yongqin and C. Deliang, *Mate. Sci. Engg.* **B86** (2001) 109.
109. V. S. Letokhov, *Sov. Phys. JETP* **26** (1968) 835.
110. C. Guedard, H. Husson, C. Sauteret, F. Auzel and A. Migus, *J. Opt. Soc. Am. B.* **10** (1993) 2358.
111. D. S. Wiersma and Ad. Lagendijk, *Phys. Rev. E.* **54** (1996) 4256.
112. N.M. Lawandy, R.M. Balachandran, A.S.L. Gomes and E. Sauvain, *Nature*, **368** (1994) 436.
113. H.Cao, J.Y.Xu, S.H.Chang and S. T. Ho, *Phys. Rev. E* **61** (2000) 1985.
- 114..D.S. Wiersma, M.P. van Albada and A. Lagendijk, *Nature (London)* **373** (1995) 203.
- 115.W. Sha, C.-H. Liu, and R. Alfano, *Opt. Lett.* **19** (1994) 1922.
- 116.Anirban Mitra and R. K. Thareja, *Mod. Phys. Lett. B.* **13** (1999) 1075.
- 117.D. Wiersma, *Nature*, **406** (2000) 132.
- 118.D. S. Wiersma, P. Bartolini and Ad Lagendijk and R. Righini. *Nature*, **390** (1997) 671.
- 119.G. van Soest, M. Tomita and Ad Lagendijk, *Optics Lett.* **24** (1999) 306.
120. R. C. Polson, G. Levina and Z. V. Verdeny, *Appl. Phys. Lett.* **76** (2000) 3858.
121. R.C.Polson, J. D. Huang and Z. V. Verdeny, *Synth. Mate.* **119** (2001) 7.

- 122.H. Kressel and J.K. Bulter, *Semiconductor Lasers and Heterojunction LEDs*, Academic Press, New York.
- 123.J.M. Hvam, J. Appl. Phys. **49** (1978) 3124.
- 124.P. Yu, Z.K. Tang, G.K.L. Wong, M. Kawasaki, A. Ohtomo, H. Koinuma and Y. Segawa, J. Cryst. Growth. **184/185** (1998) 601.
- 125.R. K. Thareja and A. Mitra, Appl. Phys. B **71**, (2000) pp 181-184.
- 126.A. Mitra and R. K. Thareja, J. of Appl. Phys. **89**, (2001) pp 2025
- 127.A. Y. Zyuzin, Phys. Rev. E, **51** (1995) 5274.
- 128.S. John and G. Pang, Phys. Rev. A **54** (1996) 3642.
- 129.G. A. Berger, M.Kempe and A.Z.Genack, Phys. Rev. E. **56** (1997) 6118.
- 130.P. Pradhan and N. Kumar, Phys. Rev. B, **50** (1994) 9644.
- 131.Z. Q. Zhang, Phys. Rev. B. **52** (1995) 7960.
- 132.X. Jiang and C. M. Soukoulis. Phys. Rev. B. **59** (1999) 6159
- 133.X. Jiang and C. M. Soukoulis. Phys. Rev. Lett. **85** (2000) 70.
- 134.Values are for Coumarine laser dye in methanol as a solvent, see ref [133].
- 135.A. E. Siegmann, *Lasers*, (Mill Valley, California, 1986). See Chaps. 2,3,6 and 13.
- 136.M. M. Fajer, Phys. Today **47**, (1994) 25.
- 137.P. A. Franken, A.E. Hill, C.W.Peters and G. Weinreich, Phys. Rev. Lett. **7**, (1961) 118.
- 138.L. Guo, S. Yang, C. Yang, P. Yu, J. Wang, W. Ge, and G. K. L. Wang, Appl. Phys. Lett. **76** (2000) 2901.
- 139.P. M. Verghese and D. R. Clarke, J. Appl. Phys. **87** (2000) 4430.
- 140.T. Doumuki, H. Tamada, and M. Saitoh, Appl. Phys. Lett. **65** (1994) 2519.
- 141.U. Griebner, R.A. Kaendl, T. Elsaesser and W. Seeber, Appl. Phys. B. **67**, (1998) 757.
142. R. W. Boyd, *Nonlinear Optics*, Academic Press.
- 143.J. Jerphagnon and S. K. Kurtz, J. App. Phys. **41** (1970) 1667.
- 144.P.D. Maker, R.W.Terhune, M. Nishenhoff, and C.M.Savage, Phys. Rev. Lett. **8**, (1962) 121.
- 145.H.Cao, J.Y.Wu, H.C.Ong, J.Y.Dai, and R.P.H.Chang, App. Phys. Lett. **73**, (1998) 572.

- 
146. A. Mitra and R. K. Thareja, *Mod. Phys. Lett. B.* **15**, (2001) pp 515.
147. Y. R. Shen, *The Principles of Nonlinear Optics* (Wiley, New York, 1984).
148. S. K. Kurtz and T. T. Perry, *J. Appl. Phys.* **39**, (1968) 3798.
149. G. Wang, G. T. Kiehne, G.K.L. Wong, J.B. Ketterson, X. Liu and R.P.H. Chang, *Appl. Phys. Lett.* **80** (2002) 401.

A 145026

